

RELEASE DATE

DEC 6 1956

Copy

RM A56I04

NACA RM A56I04



3 1176 00083 9333

~~CONFIDENTIAL~~

UNCLASSIFIED

C, 1



RESEARCH MEMORANDUM

THE STATIC AND DYNAMIC-ROTARY STABILITY DERIVATIVES

AT SUBSONIC SPEEDS OF AN AIRPLANE MODEL

WITH AN UNSWEPT WING AND A HIGH

HORIZONTAL TAIL

By Donald A. Buell, Verlin D. Reed, and
Armando E. Lopez

Ames Aeronautical Laboratory
Moffett Field, Calif.

LIBRARY COPY

DEC 13 1956

LANGLEY AERONAUTICAL LABORATOR
LIBRARY NACA
LANGLEY FIELD, VIRGINIA

CLASSIFIED DOCUMENT

This material contains information affecting the National Defense of the United States within the meaning of the Espionage laws, Title 18, U.S.C., Secs. 793 and 794, the transmission or revelation of which in any manner to an unauthorized person is prohibited by law.

**NATIONAL ADVISORY COMMITTEE
FOR AERONAUTICS**

WASHINGTON

December 5, 1956

UNCLASSIFIED

~~CONFIDENTIAL~~

CLASSIFICATION CHANGED

UNCLASSIFIED

By *gA* ty of TPA # 27 Date 7-28-60

[REDACTED]
NATIONAL ADVISORY COMMITTEE FOR AERONAUTICS

UNCLASSIFIED

RESEARCH MEMORANDUM

THE STATIC AND DYNAMIC-ROTARY STABILITY DERIVATIVES

AT SUBSONIC SPEEDS OF AN AIRPLANE MODEL

WITH AN UNSWEPT WING AND A HIGH

HORIZONTAL TAIL

By Donald A. Buell, Verlin D. Reed, and
Armando E. Lopez

SUMMARY

Measurements were made in a wind tunnel of the static and dynamic-rotary stability derivatives of a model having an unswept wing of low aspect ratio and a high horizontal tail. The tests were conducted at Mach numbers from 0.25 to 0.94 at Reynolds numbers of 0.75 to 8.00 million. The angle-of-attack range was -8° to 24° .

The components of the model were tested in various combinations and the contributions of these components to the measured derivatives are discussed. The stick-fixed oscillatory response of a representative airplane was calculated for flight at altitudes from sea level to 40,000 feet. The airplane was found to have adequate damping of the short-period longitudinal oscillation but inadequate damping of the lateral-directional oscillation.

Estimates were made of the rotary derivatives by semiempirical methods. A comparison of the estimates with measured values is made on the basis of effects on the oscillatory response.

INTRODUCTION

A program of research on the dynamic stability derivatives of various airplane models is being carried out in the Ames 12-foot pressure wind tunnel. The models are tested on an apparatus which forces an oscillation with a single degree of freedom. (The apparatus is described in ref. 1.) The results of tests employing this equipment with a triangular-wing model are presented in reference 2.

[REDACTED]
UNCLASSIFIED

The present report contains the measured static and dynamic-rotary stability derivatives for a model having an unswept wing of low aspect ratio and a high horizontal tail. These measurements were made to evaluate the separate effects of the model components on each of the derivatives and the relative importance of each derivative on the calculated oscillatory response of a representative airplane. Estimates of the rotary derivatives were made by some of the simpler existing procedures, and the agreement between the theory and experiment is assessed on the basis of the airplane-response calculations.

The static-stability characteristics of a model similar to the model of this report have been reported in references 3 and 4 for speeds into the supersonic regime. Another similar model has been the subject of a test employing the steady-rolling technique, and the resulting rolling derivatives are presented in reference 5.

SYMBOLS

C_L	lift coefficient, $\frac{\text{lift}}{\frac{1}{2}\rho V^2 S}$
C_N	normal-force coefficient, $\frac{\text{normal force}}{\frac{1}{2}\rho V^2 S}$
C_D	drag coefficient, $\frac{\text{drag}}{\frac{1}{2}\rho V^2 S}$
C_Y	side-force coefficient, $\frac{\text{side force}}{\frac{1}{2}\rho V^2 S}$
C_l	rolling-moment coefficient, $\frac{\text{rolling moment}}{\frac{1}{2}\rho V^2 S b}$
C_m	pitching-moment coefficient, $\frac{\text{pitching moment}}{\frac{1}{2}\rho V^2 S \bar{c}}$
C_n	yawing-moment coefficient, $\frac{\text{yawing moment}}{\frac{1}{2}\rho V^2 S b}$

$$(\dot{}) \quad \frac{d()}{dt}$$

()' () referred to body axes

The stability system of axes used for the presentation of the data, together with an indication of the positive direction of forces, moments, and angles, is presented in figure 1. The various stability derivatives are defined as follows:

$$\left. \begin{array}{l} C_{L\dot{\alpha}}, C_{m\dot{\alpha}}, C_{N\dot{\alpha}}, \\ C_{l\dot{\beta}}, C_{n\dot{\beta}}, C_{Y\dot{\beta}} \end{array} \right\} \text{derivatives with respect to subscript}$$

$$\begin{array}{l} C_{L\dot{\alpha}}, C_{L\dot{q}}, C_{m\dot{\alpha}}, C_{m\dot{q}} \\ C_{l\dot{\beta}}, C_{l\dot{p}}, C_{l\dot{r}}, \\ C_{n\dot{\beta}}, C_{n\dot{p}}, C_{n\dot{r}}, \\ C_{Y\dot{p}}, C_{Y\dot{r}} \end{array} \left. \vphantom{\begin{array}{l} C_{L\dot{\alpha}}, C_{L\dot{q}}, C_{m\dot{\alpha}}, C_{m\dot{q}} \\ C_{l\dot{\beta}}, C_{l\dot{p}}, C_{l\dot{r}}, \\ C_{n\dot{\beta}}, C_{n\dot{p}}, C_{n\dot{r}}, \\ C_{Y\dot{p}}, C_{Y\dot{r}} \end{array}} \right\} \begin{array}{l} \text{derivatives with respect to } \frac{\bar{c}}{2V} \times \text{subscript} \\ \text{derivatives with respect to } \frac{b}{2V} \times \text{subscript} \end{array}$$

MODEL

The complete model consisted of an unswept wing of aspect ratio 2.44, a horizontal tail mounted in a high position on a vertical tail, and a body with a circular cross section modified by the addition of a canopy and protuberances simulating side inlets. Figure 2 is a three-view drawing of the model showing some of the important dimensions. A photograph of the model mounted on the oscillation apparatus in the wind tunnel is shown in figure 3. Additional geometric and dimensional model data are given in table I.

Construction details of the model are of interest because of the unique problems presented in dynamic testing. Although the weight of the model did not have a direct bearing on the accuracy of the measured aerodynamic data, it was desirable to keep the weight as low as practicable because in this way other design and vibration problems in the model support and oscillation mechanism were minimized. Structural rigidity in the model was also felt to be desirable to minimize flutter and aeroelastic distortion; however, no quantitative measurements were made to evaluate their possible effects.

The model was built of magnesium alloy in five major parts: the wing, the vertical tail, the horizontal tail, the body shell, and the case, which enclosed the oscillation mechanism or the strain-gage balance, and to which the other parts were attached. The wing, vertical

A	$C_{1/2}$	number of cycles for the lateral oscillations to damp to half amplitude
	M	Mach number
	R	Reynolds number
	S	wing area
	$T_{1/2}$	time to damp to half amplitude
	V	velocity
	V_e	equivalent airspeed, ft/sec
	v_e	$V_e \beta $
	b	wing span
	\bar{c}	wing mean aerodynamic chord
	i_t	angle of horizontal-tail incidence, deg
	l_t	tail length
	p	rolling velocity
	q	pitching velocity
	r	yawing velocity
	t	time
	α	angle of attack, radians except where noted
	β	angle of sideslip, radians except where noted
	ϵ	effective angle of downwash at the horizontal tail, deg
	θ	angle of pitch, deg
	ρ	air density
	ϕ	angle of bank, deg
	ψ	angle of yaw, deg
	ω	circular frequency of oscillation, radians/sec

tail, horizontal tail, and the case were machined from solid magnesium forgings. In the fabrication of the body, sections of soft magnesium sheet were formed to shape in a drop-hammer die, then fastened together and attached to the case. The brackets which fixed the horizontal tail at angles of incidence of 4° , 0° , and -4° were machined from aluminum. The resulting weight of the model was approximately 15.7 pounds, of which the wing weight was 4.5 pounds, the vertical tail 1.6 pounds, the horizontal tail 0.7 pound, the bracket 0.2 pound, the body 3.5 pounds, and the case 5.2 pounds. Two interchangeable wings were constructed, the dihedral of one being -10° , as shown in figure 2, and the dihedral of the other being 0° . The axis of rotation in changing dihedral was at approximately the intersection of the wing with the body.

APPARATUS

The static-force and -moment characteristics were measured with a 4-inch-diameter four-component strain-gage balance enclosed within the model body. Six-component data were obtained by rotating the balance 90° with respect to the model. The dynamic stability derivatives were measured on a special oscillation apparatus which is a single-degree-of-freedom oscillatory system. The model was mounted on crossed-flexure restraining springs which permitted rotation about one axis only. Various combinations of rolling, pitching, and yawing motions were obtained in this system by variations in the orientation of the axis of oscillation. The moments due to prescribed combinations of these motions were measured and separated into the various stability derivatives.

It should be noted that the experimental technique did not permit the separation of the rotary derivatives into all the desired components. The pitching and yawing moments caused by the oscillation of a model in straight flight may be thought of as consisting of components caused by (1) rotation (identified by the subscripts q or r), which would result from a curved flight path with the attitude of the model maintaining the same relation to the flight direction, and (2) acceleration (identified by the subscripts $\dot{\alpha}$ or $\dot{\beta}$), resulting from transverse accelerations which bring the model back to the straight flight path. Only the sum of these two components about each of the transverse stability axes could be established.

Oscillations were excited and maintained about the axis of rotation by a push-rod linked to an electromagnetic shaker. The shaker was, in turn, excited by an electronic feedback network which maintained the desired amplitude of oscillation at the natural frequency of the model mounted on the flexure-pivot support. The necessary strain-gage measurements were processed through an analog computing system which evaluated

and recorded the amplitude and phase relationship of each oscillatory quantity. This method is described in detail in reference 1.

TESTS

Tests of the model were made at Mach numbers from 0.25 to 0.94 for a range of angles of attack from -8° to $+24^\circ$ or, at high speeds, from -8° to the maximum obtainable without choking of the wind tunnel or erratic oscillation of the model. The Reynolds number was 1.50 million for most of the tests, although data were also obtained at Reynolds numbers up to 8.00 million for low speeds and at 0.75 million for high speeds.

In the oscillation tests, the frequency of the oscillation ranged from 4 to 9 cycles per second, depending on the mass and aerodynamic restoring moments of the particular configuration. The reduced frequency, $\omega c/2V$ (a basic parameter in comparing the oscillatory characteristics of models having different scales), ranged from approximately 0.01 to 0.10. The amplitude of the oscillation had a peak value of approximately $\pm 1^\circ$ for the pitching tests and $\pm 2^\circ$ for the rolling and yawing tests. Data were also taken for comparative purposes at half the normal frequency and at amplitudes different from those quoted by about ± 50 percent. The reduction in frequency was accomplished by the use of flexure pivots of reduced stiffness.

In certain tests it was found necessary to increase the stiffness of the support system by means of guy wires attached to the tunnel walls a short distance behind the model. This was done to avoid a resonant condition between the model and its support system which would invalidate measurements obtained by the present test technique.

CORRECTIONS TO DATA

The data presented herein have been corrected by the method of reference 6 for the induced effect of the wind-tunnel walls resulting from lift on the model. The magnitudes of the corrections which were added to the measured values are:

$$\Delta\alpha = 0.13 C_L$$

$$\Delta C_D = 0.0022 C_L^2$$

The induced effects of the tunnel walls on the pitching moment were calculated and found to be negligible. The dynamic-stability derivatives have not been corrected for tunnel-wall effects resulting from lift on the model.

Corrections for the effects of constriction due to the wind-tunnel walls were calculated by the method of reference 7 and applied to the data. At a Mach number of 0.94 this correction amounted to an increase of less than 2 percent in the measured values of Mach number and dynamic pressure.

The drag data have been adjusted to correspond to a base pressure equal to free-stream static pressure. The effect of interference between the model and sting on measured static values of pitching- and yawing-moment coefficients was assumed to be negligible on the basis of unpublished measurements of pitching moment of the triangular-wing model of reference 2 with two different sting diameters - the 4-inch sting used for the static tests and the 2-1/4-inch sting used for the dynamic tests.

Corrections to the measured values of the damping coefficients due to internal damping of the model and oscillation mechanism were determined from wind-off measurements of the damping with the tunnel evacuated. The corrections would have changed the measured values of C_{l_p} and C_{n_r} less than 0.03 (and values of $C_{m_q} + C_{m_{\dot{\alpha}}}$ less than 0.20) and were therefore considered negligible.

The effects of aerodynamic resonance caused by the wind-tunnel walls similar to that discussed in reference 8 cannot be determined accurately in this case. The relation used in reference 9 yields a minimum wind-tunnel resonant frequency of 17 cycles per second. This frequency was for a Mach number of 0.95, with higher resonant frequencies at lower Mach numbers. Since the model oscillation frequency never exceeded 9 cycles per second, it is doubtful that aerodynamic resonance had any important effect on the data.

RESULTS

As a guide to the following discussion, an index of figures, presenting the measured and estimated aerodynamic characteristics of the model and the calculated oscillatory response characteristics of a representative fighter-type airplane geometrically similar to the model, is given in the following table:

	Figure
Longitudinal stability characteristics	
Basic data for complete model	4,5
Effects of Reynolds number	4,5
Effects of model components	6
Downwash characteristics	7
Effects of wing dihedral	8

Effects of sideslip angle	8,9
Effects of Mach number	10
Longitudinal stability derivatives, $C_{m\alpha}$ and $C_{mq} + C_{m\dot{\alpha}}$	
Basic data	11
Effects of Mach number	12
Static lateral-directional characteristics	
Basic data for complete model	13
Sideslip derivatives, $C_{l\beta}$, $C_{Y\beta}$, $C_{n\beta}$	
Basic data	14
Effects of Reynolds number	15
Effects of wing dihedral	15
Effects of model oscillation	16
Effects of Mach number	17
Lateral rotary derivatives, C_{lp} , C_{np} , $C_{lr} - C_{l\dot{\beta}}$, $C_{nr} - C_{n\dot{\beta}}$	
Basic data	18,19
Effects of Reynolds number	20
Effects of wing dihedral	20
Effects of Mach number	21
Dynamic-stability estimates (controls-fixed)	
Longitudinal short-period oscillation	22
Lateral-directional short-period oscillation	23
Comparison using measured and predicted dynamic derivatives . .	24
Stability derivatives for the complete model referred to body axes (see Appendix for description of the axis system).	25

The lateral stability characteristics are presented for 0° incidence of the horizontal tail.

DISCUSSION

The discussion will be concerned with first, the measured aerodynamic characteristics of the model, second, the calculated oscillatory response of a representative airplane, and third, the estimation of the rotary derivatives. The primary purpose of the investigation was the measurement of the stability derivatives of a model representing an airplane of modern design. Of these, the rotary derivatives are ordinarily the ones least amenable to measurement and, consequently, are the ones considered here in most detail. An examination of the estimated values of these derivatives is postponed until after a discussion of the oscillatory response calculations, because the accuracy desired in the estimation of any derivative should be determined only in light of its effect on the behavior of the airplane.

The effects of frequency and amplitude of the model oscillation on the data have been considered although the data are not shown. The effects of a reduction in frequency of 50 percent were in most cases indistinguishable from experimental scatter. However, the frequency effects were

not checked at high Mach numbers in the case of lateral oscillations. A change in oscillation amplitude of 50 percent had only minor effects on the measured derivatives.

The Measured Static Longitudinal Characteristics

Static stability.- Figure 4 shows that, at Mach numbers of 0.90 and less, a reduction in lift-curve slope occurred as the angle of attack was increased beyond 8° to 10° , followed by a large positive increase in the slope of the pitching-moment curves at somewhat higher angles of attack. This loss of stability continued to an angle of attack of at least 20° and was of such a magnitude as to make the model unstable beyond 14° . These longitudinal characteristics suggest a severe pitch-up problem at high angles of attack for a large range of center-of-gravity positions. The data for a Mach number of 0.94 also showed a decrease in stability at high angles of attack but were too limited in this range to define the pitching-moment curve properly.

Effect of model components.- It may be seen from the pitching-moment curves of figure 6 that the loss of stability at high angles of attack was caused by the forces on the horizontal tail. The origin of the destabilizing variation of tail load may be traced, in turn, to wake and downwash effects. Evidence of the movement of the tail into the wing and body wakes is the loss of $\partial C_m / \partial i_t$, shown by the gradual convergence of the pitching-moment curves for different tail incidences as the angle of attack was increased (fig. 4). The more powerful downwash effects are shown in figure 7 in the form $1 - (\partial \epsilon / \partial \alpha)$, which represents the rate of change of the tail angle of attack with the model angle of attack. (The factor was determined from the data of figs. 4 and 6 by assuming the tail angle of attack to be equal to the increment of pitching-moment coefficient contributed by the tail, divided by $\partial C_m / \partial i_t$ for the particular model angle of attack under consideration.) The factor $1 - (\partial \epsilon / \partial \alpha)$ decreased rapidly with increasing angles of attack above 3° , indicating a proportional decrease in the stability contribution of the tail. The downwash tended to make the tail destabilizing above 14° for Mach numbers of 0.90 and less. At intermediate angles of attack the variations of the stability contributions of the tail and of the wing tended to be compensatory (see fig. 6).

Effects of wing dihedral and sideslip angle.- Figure 8 shows that an increase of dihedral from -10° to 0° made the model somewhat less stable, and that a sideslip angle of 6° produced a slight increase in stability. Although figure 9 shows that at angles of attack up to 6° positive stability (indicated by the increment of pitching-moment coefficient between $\alpha = 0^\circ$ and 6°) was maintained at sideslip angles up to 18° , it is evident that the stability decreased at the higher Mach number and angles of sideslip.

Effects of Mach number.- Figure 10 illustrates the rather abrupt changes in static longitudinal stability which were caused by increasing Mach number. The figure shows further that there were increases in the lift-curve slopes of the wing and tail (the latter is reflected in the curves of $\partial C_m / \partial i_t$) as the Mach number was increased in the upper range.

The Measured Longitudinal Stability Derivatives

Static-stability derivative, $C_{m\alpha}$.- The stability parameter $C_{m\alpha}$ was measured on the oscillating model and is compared with values from the static-force tests in figure 11. Deflection of the flexure pivots in the oscillation mechanism limited the tests of each configuration to angles of attack near that for $C_m = 0$. The Reynolds number of 0.75 million was particularly useful since the lesser restoring moments produced at this Reynolds number permitted model oscillation over a more extensive angle-of-attack range than was possible at a Reynolds number of 1.50 million. Where the comparison could be made, the data for the Reynolds number of 0.75 million appeared to be representative of the data for 1.50 million in the over-all trends with angle of attack and Mach number.

The comparison of the values of $C_{m\alpha}$ measured statically and dynamically shows good agreement, except at the lowest test Mach number. It should be noted that static-force data for only one tail incidence have been included in figure 11. The difference between the static and oscillatory values of $C_{m\alpha}$ at the high angles of attack is due primarily to the previously mentioned loss of tail effectiveness which resulted in different values of $C_{m\alpha}$ for different tail incidences.

The large effects of Mach number on the static longitudinal stability which were previously noted are again demonstrated by the values of $C_{m\alpha}$ in figure 12. The data presented are for angles of attack of 4° or -4° since these were the only angles at which the higher Reynolds number data were available at all Mach numbers.

Damping-in-pitch derivative, $C_{mq} + C_{m\dot{\alpha}}$.- The derivative $C_{mq} + C_{m\dot{\alpha}}$, measured simultaneously with $C_{m\alpha}$ during pitching oscillations of the model, is presented in figure 11. For reasons mentioned previously the lower Reynolds number data are the more extensive. There was no Reynolds numbers effect large enough to be differentiated from scatter in the data at Mach numbers below 0.85. At higher Mach numbers the trends produced by increasing angle of attack at the low Reynolds number seemed to be repeated at the higher Reynolds number but, in certain cases, at distinctly different levels of damping.

It is noteworthy that at the higher Mach numbers the model with the horizontal tail removed provided a large proportion of the damping of the complete model at some angles of attack, and little damping at others. For example, at a Mach number of 0.94 and a Reynolds number of 1.50 million, the damping attributable to the body and wing was 50 percent of the total at an angle of attack of -4° but diminished rapidly as the angle of attack became more negative. A similar loss of damping of the body-wing-vertical-tail combination occurred at all test Mach numbers above 0.85 and was in each case accompanied by a large gain in static stability. The same relationship between damping in pitch and static longitudinal stability was observed with the triangular-wing model of reference 2. It can be determined from the data in figure 6 that the wing caused variations in $C_{m\alpha}$ at positive angles of attack that were of the same order of magnitude as those noted in figure 11 at negative angles of attack, and it seems probable that the wing was also the source of large variations in damping.

It is remarkable that there was a total lack of damping of the complete model at the higher Mach numbers at some large angles of attack. Relations such as are given in reference 10 lead to the expectation of a favorable downwash effect on tail damping as angle of attack is increased. Unfortunately, there were insufficient data to establish the damping contributions of the various model components and to determine if the unsteady flow conditions on the wing had actually altered the downwash effects on damping.

The damping of the complete model at 4° angle of attack increased with Mach number up to 0.92 but decreased at a Mach number of 0.94 (fig. 12). If it is assumed that the damping of the body-wing-vertical-tail combination at -4° angle of attack is representative of that at 4° , it may be concluded that the horizontal tail caused part of the increase in damping of the complete model with Mach number and was primarily responsible for the decrease at Mach numbers above 0.92.

The Measured Static Lateral-Directional Characteristics

The sideslip derivatives were determined from static-force tests by measuring the forces and moments at one angle of sideslip, 6° , and assuming they varied linearly with sideslip angle from 0° to 6° . Additional data, presented in figure 13, establish the validity of the assumption for the complete model at angles of attack up to 6° . Other data not presented showed that the lateral forces and moments for 0° of sideslip were negligible at angles of attack up to 20° .

The measurements of the lateral-directional characteristics were confined to model configurations having only one horizontal tail incidence, 0° . The possibility that there may be an effect of tail incidence

on the lateral-directional derivatives at high subsonic Mach numbers is pointed out in reference 11, which reports the results of an investigation with an unswept "T" tail. Although not investigated, the effect of tail incidence on the subject model is believed to be smaller than in the case with the model of reference 11 on the basis of the differences in tail geometry, which makes the tail of the subject model less conducive to the shock interference discussed in the reference. Also, as pointed out in the reference, the effect is encountered only at small angles of attack with large negative tail incidences, which is an out-of-trim condition of secondary importance.

Rolling moment due to sideslip, $C_{l\beta}$. The complete model was found to have a positive dihedral effect (negative $C_{l\beta}$) at all angles of attack at which the model was tested (see fig. 14). Much of the dihedral effect was contributed by the vertical tail, as may be seen from a comparison of the data for the body and the body-vertical-tail combination, although this contribution diminished to approximately zero for angles of attack of 12° and more. The end-plate effect of the horizontal tail amplified the dihedral effect of the vertical tail. The addition of the wing at a dihedral of -10° reduced the dihedral effect at angles of attack up to about 6° to 8° but, except at the highest test Mach number, provided a positive rather than negative dihedral effect at the highest angles. At Mach numbers of 0.80 and 0.90 the abrupt changes observed in $C_{l\beta}$ at angles of attack near 10° are thought to be caused by an asymmetric loss of wing lift.

The oscillatory and static-force-test values of $C_{l\beta}$ shown in figure 16(a) were in good agreement except possibly at a Mach number of 0.25. The comparison of $C_{l\beta}$ was similar to that of $C_{m\alpha}$ in this respect.

Yawing moment due to sideslip, $C_{n\beta}$. The complete model had positive directional stability, $C_{n\beta}$, (fig. 14) over the angle-of-attack range of the test, although the stability diminished with increases in angle of attack beyond about 14° . The stability afforded by the vertical tail was increased by the end-plate effect of the horizontal tail. The addition of the wing also gave rise to a small but definite increase in the effectiveness of the tail at most angles of attack. However, it may be observed in figure 15 that an increase in the wing dihedral angle to 0° caused a decrease in directional stability, approximately nullifying the favorable interference effect noted for the wing of -10° dihedral in figure 14.

Figure 16(b) shows that the oscillatory and static-force-test values of $C_{n\beta}$ were in good agreement for the body-wing combination. The agreement between the two test conditions was not so good for the complete model. It is possible that the extreme rearward position of the vertical tail on this model may have resulted in sting interference on the values

of $C_{n\beta}$ and that part of the disagreement in figure 16(b) is due to the use of different sting diameters in the oscillation and static-force tests.

The chief Mach number effect on directional stability, shown in figure 17 for 0° angle of attack, was an increase with increasing Mach number, due to an increase in tail effectiveness.

Lateral Rotary Derivatives

Damping-in-roll derivative C_{l_p} .-- Figure 18 shows that the major portion of the damping in roll was contributed by the body-wing combination. The damping of both this configuration and of the complete model diminished rapidly with an increase in angle of attack beyond 6° to 8° , which is the angle range just preceding the decrease in slope of the lift curve. This trend is the same as that noted in reference 5 on a similar model.

The contribution of the tail surfaces to damping in roll increased markedly with Mach number, and was actually equal to the damping of the body-wing combination at a Mach number of 0.94 at 0° angle of attack. The end-plate effect of the horizontal tail again increased the contribution of the vertical tail as was the case with the sideslip derivatives. While the tail was expected to provide damping with no wing present, it was anticipated that the sidewash produced by the rolling wing would create a rolling moment on the tail which would almost nullify the damping of the tail. This result was in fact realized at the lowest speeds, but at the higher Mach numbers (fig. 18) the damping of the tail was in many cases practically undiminished by the addition of the wing. The tail provided much smaller values of damping in the steady-rolling tests of reference 5, but this disparity in results was not limited to the wing-on case. The apparent conclusion is that the oscillatory motion produced substantial tail damping that was not greatly affected by wing sidewash at the higher Mach numbers. As a result, the damping in roll of the model increased with Mach number, as shown for 0° angle of attack in figure 21.

Reynolds number and dihedral effects, presented in figure 20(a), were not discernible from experimental scatter.

Yawing moment due to rolling velocity C_{n_p} .-- Figure 18 shows that at small and negative angles of attack the values of C_{n_p} for the complete model were positive but that they became increasingly negative as the angle of attack was increased above 2° to 4° . Unlike the damping in roll, the expected effect of wing sidewash on C_{n_p} was observed at all Mach numbers; that is, the sidewash at the tail was expected to produce negative

increments in C_{np} , and the test results established that the C_{np} of the complete model was much more negative than would result from a simple addition of the body-wing values and the body-tail values.

The effects of wing dihedral and Reynolds number on C_{np} are shown in figure 20. Generally, a change in wing dihedral from -10° to 0° resulted in substantial positive increases in C_{np} , particularly at the higher Mach numbers. The values of C_{np} were also rather sensitive to Reynolds number at these Mach numbers.

The effect of Mach number on C_{np} at 0° angle of attack (fig. 21) was to increase the positive value of C_{np} at a Mach number of 0.94 to about twice the value observed at Mach numbers below 0.90.

Rolling moment due to yawing velocity $C_{l_r} - C_{l_\beta}$.- Figure 19 shows that this derivative was positive for the complete model at angles of attack up to at least 8° . The positive values were due, for the most part, to the tail. Values of this derivative for higher angles of attack than those shown in figure 19 were actually measured and are presented in figure 25 referred to a body system of axes. (A discussion of the body system of axes is in the Appendix.) A sharp decrease in $C_{l_r} - C_{l_\beta} \cos \alpha$ for the complete model is evident in figure 25 above 10° angle of attack at Mach numbers of 0.80 and higher. This large change, presumably associated with an asymmetric loss of wing lift, did not materialize at the lower Reynolds number, however (see fig. 20(c)).

The effects of dihedral on $C_{l_r} - C_{l_\beta}$ were irregular over the angle-of-attack range, and were largest at the higher Mach numbers, being similar to C_{np} in this respect. In both derivatives, Reynolds number effects varied with angle of attack in a nonuniform manner and were largest at the highest Mach number.

Damping-in-yaw derivative $C_{n_r} - C_{n_\beta}$.- The data of figures 19 and 25 show that the damping in yaw of the complete model was maintained at a high level for angles of attack up to at least 12° . There was some increase in damping at angles of attack above 6° with a subsequent loss at still higher angles, where the damping of the body-wing combination became less. The body appeared to be the major factor in the loss of damping at high angles of attack. It should be stated here that the measurements made with the body alone were sufficient only to establish the values of the damping in yaw and the rolling moment due to yawing velocity referred to body axes. To obtain the body-alone damping referred to stability axes, as is presented in figure 19, it was necessary to assume that the moments due to the body's rolling about its longitudinal axis were zero. Such an assumption may have

created errors in the values of body-alone damping at the larger angles of attack, but the data are presented, nevertheless, in the belief that the correct trend is indicated.

As shown in figure 19, the addition of the horizontal tail increased the effectiveness of the vertical tail in providing damping in yaw, except at a Mach number of 0.94. The contribution of the tail to damping increased considerably with angle of attack for the wing-off case, but with the wing on there was much less increase. Evidently, the nature of the wing interference on the tail damping and on the tail restoring moments was quite different; that is, this interference on $C_{n_r} - C_{n_\beta}^0$ was favorable at negative angles of attack and unfavorable at high positive angles of attack, whereas the interference effect on C_{n_β} (fig. 14) was always favorable.

At 0° angle of attack there was an increase in damping with increasing Mach number up to about 0.85, as illustrated in figure 21, but above this Mach number there was a loss of damping contributed by the tail. The latter effect was caused wholly by the horizontal tail, which had an unfavorable interference effect on the damping of the vertical tail at high Mach numbers (fig. 19). This was true regardless of whether or not the wing was attached. The effect is not simply explained since the horizontal tail maintained an end-plate effect on the vertical-tail contribution to C_{n_β} at all Mach numbers.

The Reynolds number and dihedral effects (fig. 20(d)) were largest at the highest Mach numbers, as was the case with C_{n_p} and $C_{l_r} - C_{l_\beta}$.

Dynamic-Stability Calculations

In order to provide a better perspective of the dynamic stability of this particular configuration, the data in the foregoing figures have been applied to calculations of the dynamic motions for a representative airplane. Values of the period and time to damp of the short-period longitudinal and lateral-directional oscillations have been calculated and the dynamic characteristics compared with the requirements of reference 12. It should be pointed out that if the requirements are not met, it does not necessarily mean that the motions will be unsafe or divergent, but rather that the airplane may not be able to execute satisfactorily its expected maneuvers.

The mass and dimensional data for the representative airplane used in these calculations are presented in table II.

Dynamic longitudinal stability.- The period and time to damp of the short-period controls-fixed longitudinal oscillations were calculated by the method given in the Appendix of reference 2. Additional derivatives other than those measured in this investigation enter into the calculations but have little effect on the period or time to damp. These include C_{Lq} and $C_{L\dot{q}}$. A variation of either of these two derivatives from 0 to 4 produced a change in period of about 2 percent and essentially no change in damping. Also an independent variation of C_{mq} and $C_{m\dot{q}}$ resulted in a similarly small change. If the measured damping is assumed to be entirely due to $C_{m\dot{q}}$, the period is increased by no more than 10 percent over what it would be if the damping were due entirely to C_{mq} .

The results of the calculations of the period and time to damp to half amplitude, presented in figure 22, indicate that for all the conditions considered, the airplane has dynamic-longitudinal-stability characteristics which adequately fulfill the requirements of reference 12. It should be noted that due to the restricted amount of data available at a Reynolds number of 1.50 million, it was necessary to use damping derivatives measured at a Reynolds number of 0.75 million in estimating the longitudinal dynamic stability for the higher Mach numbers. This procedure gave somewhat misleading results at a Mach number of 0.94, because a large Reynolds number effect was present in the data for an angle of attack (4°) corresponding to an altitude of 40,000 feet. Figure 11(g) shows that at the lower Reynolds number the damping of the model decreased rapidly at angles of attack above 2° (corresponding to 20,000 feet). It is evident that the calculated stability characteristics of the airplane at the higher altitudes and at a Mach number of 0.94 would have been better if the higher Reynolds number data had been used.

Dynamic lateral stability.- The period and damping of the short-period lateral-directional oscillations have been calculated by the method of reference 13. Derivatives encountered in the calculations included C_{Yr} and C_{Yp} , which were not measured in this investigation. Estimates were made of these two derivatives, and it was found that any reasonable variation in either derivative resulted in only negligible changes in the period and damping. These derivatives were therefore assumed to be zero. Another limitation of the calculations is the lack of separate values for the derivatives due to sideslipping acceleration, $C_{n\dot{\beta}}$ and $C_{l\dot{\beta}}$. In this situation the measured values of $C_{nr} - C_{n\dot{\beta}}$ and $C_{lr} - C_{l\dot{\beta}}$ have been used in the equations of reference 13 in place of C_{nr} and C_{lr} , with no consideration being given to the $\dot{\beta}$ terms separately. This is believed to be the most accurate way to take account of the possible effects of sideslipping acceleration in the absence of independent measurements of all derivatives.

The results of the calculations are presented in figure 23. Although the period and time to damp were considered sufficient indications of the acceptability of the longitudinal response, they provide only part of the information necessary to evaluate the lateral-directional stability. The damping parameter $1/C_{1/2}$ still represents damping in the same sense as was considered in longitudinal motions, since it is merely the ratio of the period P to the time required to damp to half amplitude, $T_{1/2}$. However, the minimum value desirable is no longer fixed, but varies with the roll-excitation parameter $|\phi|/|v_e|$. This parameter, representing the tendency of the airplane to roll when disturbed in sideslip, was calculated by the method outlined in the Appendix of reference 14.

The boundaries in figure 23 indicate minimum acceptable values as defined in reference 12. Boundary A represents a minimum for an airplane with no artificial stability augmentation, and boundary B is a minimum for an airplane which normally employs an artificial stabilizing device but with the device inoperative. The uppermost boundary is the minimum for a tactical mission and is therefore the value which must be attained at the design conditions, by an artificial device if necessary.

The calculated values in figure 23 fall well below the minimum required for a tactical mission, but the values are all above boundary B. It may be noted that there was a decrease in the stability as the altitude increased, particularly at the higher Mach numbers. Such a situation was due partially to an increase in the relative density factor of the airplane, which is a factor relating inertial forces to aerodynamic forces. A second and important factor was the decrease in C_{n_p} which accompanied the increase in angle of attack as altitude increased.

The dependence of the damping parameter on C_{n_p} is demonstrated by the results of calculations for a Mach number of 0.90. For these calculations the effect of the relative density factor was eliminated by considering only a constant altitude. It was here indicated that a decrease in C_{n_p} of 0.1 would result in a loss in $1/C_{1/2}$ of about 0.15. By way of comparison, it may be noted that the range of values of C_{n_p} which was encountered in the preparation of figure 23 was almost 0.25. It is perhaps obvious that the effect of C_{n_p} was large for this particular model because of the interaction of this derivative with other factors in the equations of motion. An examination of the equations indicated that a large dihedral effect was of the most importance in this respect, and calculations verified that the effect of C_{n_p} would have been negligible if C_{l_β} had been zero.

The damping-in-roll derivative, C_{l_p} , is the only other derivative involved to any great extent in the changes of dynamic stability with altitude and Mach number that are indicated in figure 23. The effect of increases in roll damping on the parameter $1/C_{1/2}$ was favorable and about

one half as great as the effect of C_{np} at a Mach number of 0.90 and 40,000 feet. However, at 20,000 feet C_{lp} had practically no effect, so that its importance is not simple to evaluate. The derivative $C_{nr} - C_{n\dot{\beta}}$ was almost constant in the range of flight conditions considered in figure 23, so that this derivative had little to do with the changes in dynamic stability shown. However, if $C_{nr} - C_{n\dot{\beta}}$ had varied by an amount equal to C_{np} it would have produced about one third of the effect on $1/C_{1/2}$ that was caused by C_{np} .

Figure 23 shows an increase of the roll-excitation parameter $|\phi|/|v_e|$ with altitude. This was caused primarily by changes in the relative density factor. The only aerodynamic derivatives which cause significant changes in $|\phi|/|v_e|$ are the static derivatives $C_{l\beta}$ and $C_{n\beta}$. However, these did not vary enough in the range of flight conditions examined to cause much effect.

Estimates of Rotary Derivatives

An estimation of the rotary derivatives of the model has been attempted, using some of the simpler methods available and utilizing the static-force data where possible. The results of these calculations are shown by the curves labeled "theory" in the figures. The theory and experiment are compared on the basis of the effect these derivatives had on the estimated oscillatory response of the representative airplane.

Estimate of $C_{mq} + C_{m\dot{\alpha}}$. - The contribution of the body to this derivative was determined by the method developed in reference 15, from which equation (B21) is repeated for convenience:

$$\left(C_{mq} + C_{m\dot{\alpha}} \right)_{\text{body}} = - \frac{4B_D}{Sc^2} (l - x_0)^2$$

where

B_D base area

$l - x_0$ distance from base of body to axis of rotation.

It may be seen in figure 11 that this estimate compared well with the data for the body-vertical-tail combination for all angles of attack at which the model was tested.

The wing contribution was also estimated by the method in reference 15. In this case it was necessary to expand certain terms in the equations so that they would apply to other than triangular wings. For the particular plan form of the wing of this investigation, only the moment due to camber (which was intended to be equivalent to a flat wing in pitch) was of any consequence in the estimation of $(C_{mq})_{wing}$. Therefore, the relation used was as follows:

$$(C_{mq})_{wing} = \frac{-\frac{9\pi}{32} \frac{1 + \lambda^2}{[1 + \lambda - \lambda/(1 + \lambda)]^2}}{\sqrt{1 - M^2}}$$

where

λ taper ratio, c_{tip}/c_{root}

The contribution of the wing to $C_{m\dot{\alpha}}$ was ignored on the basis that its magnitude, calculated by the method of reference 15, was generally small compared to $(C_{mq})_{wing}$. However, the trend with angle of attack of the calculated values of $C_{m\dot{\alpha}}$ was approximately the same as the trend of the experimental data for $C_{mq} + C_{m\dot{\alpha}}$ in figure 11. It is possible that inclusion of $C_{m\dot{\alpha}}$ might have improved the theoretical values if the effects of the low aspect ratio and sharp leading edge on this term had been more accurately assessed.

The largest damping component was calculated for the horizontal tail following the method of reference 10:

$$C_{mq} + C_{m\dot{\alpha}} = 2 \frac{l_t}{c} 57.3 \frac{\partial C_m}{\partial i_t} \left(1 + \frac{\partial \epsilon}{\partial \alpha} \right)$$

The pitching-moment and downwash terms used in this calculation were evaluated from the static-force tests. It may be seen in figure 11 that the

tail contribution was usually overestimated but tended to compensate for an underestimation of the wing contribution at the smaller angles of attack. Here, again, the δ term is assumed to be that which has been incorrectly evaluated, inasmuch as a relationship is expected to exist between the unsteady forces on the wing and the tail. This problem has been considered in more detail in reference 16.

Estimation of C_{lp} .- The damping-in-roll derivative was estimated by methods described in reference 13. Two components, that from the wing and that from the tail, were computed, both based on static-force data. Only the wing contribution is shown in figures 18 and 21 because the sidewash from the rolling wing was assumed to have reduced the tail contribution to a negligible amount. Calculations of the sidewash by methods suggested in reference 13 did not materially change this conclusion. The comparison with experiment for the tail-off configuration shows the estimates to be adequate at Mach numbers of 0.80 and above, but the experimental values for the complete model exceeded the calculated derivatives by as much as 0.2.

Estimation of C_{np} .- This derivative was also estimated for the body-wing combination and for the complete model. Reference 13 was used to calculate all components. However, when the method was applied to the calculation of the body-wing component, the resulting values of C_{np} were greater than +0.3 which was very large compared to the test values. Since the method uses empirical factors, another relation was employed based on considerations in reference 17. This relation was simply

$$\left(C_{np}\right)_{\text{wing}} = - \left(C_{lp}\right)_{\text{wing}} \tan \alpha$$

and is valid as long as

$$\left(C_D - C_{D_{C_L=0}}\right)_{\text{wing}} = \left(C_L\right)_{\text{wing}} \tan \alpha$$

which implies the presence of leading-edge separation. Although the data are not shown, the drag coefficient due to lift of the body-wing combination never differed from $C_L \tan \alpha$ by more than 0.01. The theoretical values for the body-wing combination in figure 18 are therefore those calculated by this latter method, using the estimated values of C_{lp} . Unfortunately, the estimate is still not in very good agreement with the test value at large angles of attack.

The estimate of the tail contribution to C_{n_p} was somewhat small at an angle of attack of 0° , but perhaps a less desirable result was that the rate of decrease of the derivative with angle of attack was underestimated. In view of the sensitivity of the airplane's oscillatory response to changes in C_{n_p} , the estimate of C_{n_p} for the complete model at high angles of attack must be considered unsatisfactory. It was possible to improve the agreement at an angle of attack of 0° by using some of the methods for calculating sidewash effects suggested in reference 13, but they did not materially improve the rate of change of C_{n_p} with angle of attack, which was felt to be the basic deficiency of the estimate.

Estimate of $C_{l_r} - C_{l_{\dot{\beta}}}$.- Values of this derivative were calculated for the wing and for the tail using reference 13 and the static-force data. The reference did not actually consider $\dot{\beta}$ terms, so they have been assumed equal to zero. The values, shown in figures 19 and 21, compared favorably with experimental values up to angles of attack of about 10° , above which large negative increases were measured (fig. 25) that were not predicted by theory.

Estimate of $C_{n_r} - C_{n_{\dot{\beta}}}$.- The estimate of damping in yaw also was accomplished using reference 13 and static-force data for the most part and again assuming the $\dot{\beta}$ term equal to zero. The exception to this procedure was the body estimate which was assumed to be:

$$\left(C_{n_r} - C_{n_{\dot{\beta}}} \right)_{\text{body}} = \left(C_{m_q} + C_{m_{\dot{\alpha}}} \right)_{\text{body}} \left(\frac{\bar{c}}{b} \right)^2$$

The estimate was fair (see figs. 19 and 21) at small angles of attack but did not take account of the loss of damping with increasing angle of attack that was measured. The calculated wing contribution was small in relation to the apparent experimental increment. It should be recalled that the measured damping in yaw about the stability axis for the body alone was an approximation since it was assumed that the body had no moments due to rolling about its longitudinal axis. The contribution of the tail was underestimated at the lower Mach numbers, but the agreement was improved at the higher Mach numbers, largely because of the unexpected loss of the end-plate effect of the horizontal tail on the measured values.

The maximum disagreement between estimated and test values of $C_{n_r} - C_{n_{\dot{\beta}}}$ for the complete model was of the same order of magnitude as was obtained with C_{l_p} . Better agreement was obtained at high Mach numbers because of the compensating effects noted for the various model components.

Comparison of theory and experiment by oscillatory-response calculations.- The over-all agreement between the estimated and measured values of the rotary derivatives can be assessed from figure 24. This figure presents calculated values of the time to damp to half amplitude, since this is the only oscillatory-response characteristic affected significantly by the rotary derivatives.

The most serious discrepancy between the damping calculated from the experimental and theoretical values of $C_{m\dot{q}} + C_{m\dot{\alpha}}$ occurs at a Mach number of 0.94 at 40,000 feet. As noted previously, the measured value of $C_{m\dot{q}} + C_{m\dot{\alpha}}$ for this flight condition was adversely affected by Reynolds number, and the theoretical value of $C_{m\dot{q}} + C_{m\dot{\alpha}}$ is actually more representative of the higher Reynolds number data. It is concluded that the estimates of $C_{m\dot{q}} + C_{m\dot{\alpha}}$ agree well with the measured values for these flight conditions.

Figure 24 shows that the damping of the lateral oscillation was lower when the estimated values of the rotary derivatives were used than when the measured values were used. The differences between the two sets of calculated damping values for an altitude of 20,000 feet were caused by differences in $C_{n\dot{r}} - C_{n\dot{\beta}}$ (primarily at Mach numbers below 0.90) and in $C_{n\dot{p}}$ (the larger influence at Mach numbers above 0.90). Both derivatives were also responsible for some of the large discrepancy in damping at a Mach number of 0.92 and an altitude of 40,000 feet, while differences in $C_{l\dot{p}}$ caused much of the disagreement at the lower Mach numbers at 40,000 feet. The figure shows that the difference in time to damp to half amplitude computed from the two sets of derivatives could amount to more than one third of the value for the representative airplane. This comparison applies, of course, only to the angles of attack corresponding to the selected flight condition ($6-1/2^\circ$ was the maximum angle of attack considered).

SUMMARY OF RESULTS

The static and dynamic-rotary stability derivatives of a model representative of modern airplane design were measured in a wind tunnel at subsonic speeds. The model had an unswept wing with a sharp leading edge, a thickness ratio of 0.034, and an aspect ratio of 2.44. The horizontal tail of the model was mounted high on a swept vertical tail. The following was observed:

1. The wing was in itself the source of large variations in $C_{m\dot{\alpha}}$ and $C_{m\dot{q}} + C_{m\dot{\alpha}}$ as angle of attack and Mach number changed. Data at Mach numbers of 0.90 and less indicated that $C_{L\dot{\alpha}}$ decreased by a large amount

above an angle of attack of 8° to 10° , and this was accompanied by large losses in $C_{l_r} - C_{l_\beta}$. The decrease in lifting effectiveness was evident also in the much smaller values of C_{l_p} as compared to those at lower angles of attack, and in abrupt variations in C_{l_β} with angle of attack.

2. The vertical tail, besides being the major source of C_{n_β} , $C_{l_r} - C_{l_\beta}$, and $C_{n_r} - C_{n_\beta}$ over most of the angle-of-attack range, had a large effect on C_{l_β} , and on C_{l_p} at high Mach numbers. The horizontal tail increased the effectiveness of the vertical tail except in the case of $C_{n_r} - C_{n_\beta}$ at a Mach number of 0.94.

3. The air flow behind the wing altered the characteristics of the tail in certain important aspects. The wing downwash increased with angle of attack enough to make the horizontal tail longitudinally destabilizing above an angle of attack of 14° . When the model was rolling, the sidewash from the wing created tail loads which made C_{n_p} negative over much of the angle-of-attack range and which reduced the tail contribution to C_{l_p} at low Mach numbers. Interference of the wing on the flow at the tail increased both C_{n_β} and $C_{n_r} - C_{n_\beta}$ at negative angles of attack but decreased $C_{n_r} - C_{n_\beta}$ at large positive angles of attack. Data on the complete model showed that a change in wing dihedral caused changes in many of the derivatives besides C_{l_β} . The effects of dihedral were especially large at high Mach numbers for C_{n_p} , $C_{l_r} - C_{l_\beta}$, and $C_{n_r} - C_{n_\beta}$, all of which are highly dependent on the air flow at the tail and consequently on the location of the tail with respect to the flow field behind the wing. These rotary derivatives, together with $C_{m_q} + C_{m_{\dot{\alpha}}}$, seemed also to be sensitive to changes in Reynolds number from 0.75 million to 1.50 million, particularly at the higher Mach numbers.

4. Calculations of the control-fixed oscillatory response of a representative airplane were made for a range of Mach numbers from 0.60 to 0.94 and of altitudes from sea level to 40,000 feet. In this range of flight conditions, the airplane had satisfactory damping of the short-period longitudinal oscillation. The lateral oscillation was sufficiently damped for the airplane to be safely flown, but the damping was insufficient for a tactical mission. The damping of the lateral oscillation was found to be sensitive to changes in C_{n_p} (because of interaction with a large negative value of C_{l_β}) and to a lesser extent on C_{l_p} and $C_{n_r} - C_{n_\beta}$.

5. Estimates were made of the rotary derivatives by semiempirical methods. On the basis of oscillatory damping calculations for the representative airplane at small angles of attack, it was concluded that the estimates of $C_{mq} + C_{m\dot{q}}$ agreed well with the measured values. Computations using the estimated and measured values of the lateral rotary derivatives indicated differences in time to damp to half amplitude of as much as one third of the value for the representative airplane.

Ames Aeronautical Laboratory
National Advisory Committee for Aeronautics
Moffett Field, Calif., Sept. 4, 1956

APPENDIX

THE STABILITY DERIVATIVES OF THE COMPLETE MODEL

ABOUT A BODY SYSTEM OF AXES

When the dynamic motions of an airplane are to be computed, it is sometimes desirable to use a body system of axes which remains fixed within the airplane rather than the stability system of axes. The use of a body system of axes simplifies the calculation of these motions in that the moment of inertia about any axis is independent of the angle of attack. The body system of axes chosen for the data presented in this report is one in which the x axis is the fuselage reference line, the z axis is perpendicular to the x axis and lies in the plane of symmetry and the y axis is perpendicular to the plane of symmetry.

The transfer of the rotary derivatives to the body axes involves the transfer of the moments, l, rolling moment and n, yawing moment, and the rotational velocities, p and r. For a pure rolling motion about the body x axis, the total damping moments about that axis are:

$$C_{l_p}^i + C_{l_{\dot{\beta}}}^i \sin \alpha = C_{l_p} \cos^2 \alpha + (C_{n_r} - C_{n_{\dot{\beta}}}) \sin^2 \alpha - \\ (C_{n_p} + C_{l_r} - C_{l_{\dot{\beta}}}) \sin \alpha \cos \alpha$$

and

$$C_{n_p}^i + C_{n_{\dot{\beta}}}^i \sin \alpha = C_{n_p} \cos^2 \alpha - (C_{l_r} - C_{l_{\dot{\beta}}}) \sin^2 \alpha - \\ (C_{n_r} - C_{n_{\dot{\beta}}} - C_{l_p}) \sin \alpha \cos \alpha$$

For a pure yawing motion about the body z axis, the total damping moments about that axis are:

$$C_{l_r}' - C_{l_{\dot{\beta}}}' \cos \alpha = (C_{l_r} - C_{l_{\dot{\beta}}}) \cos^2 \alpha - C_{n_p} \sin^2 \alpha - \\ (C_{n_r} - C_{n_{\dot{\beta}}} - C_{l_p}) \sin \alpha \cos \alpha$$

and

$$C_{n_r}' - C_{n_{\dot{\beta}}}' \cos \alpha = (C_{n_r} - C_{n_{\dot{\beta}}}) \cos^2 \alpha + C_{l_p} \sin^2 \alpha + \\ (C_{n_p} + C_{l_r} - C_{l_{\dot{\beta}}}') \sin \alpha \cos \alpha$$

As before, it is assumed that the total damping moment is the moment of most significance for calculations of airplane dynamic stability in the absence of measurements of all the individual components. Therefore, the quantity expressed by the left-hand side of each of the above equations is considered to be the desired derivative for such calculations. Incidentally, this quantity represents the moment actually measured by the present test technique.

The derivative listed above as well as the applicable static stability derivatives are presented in figure 25 for the complete model. Only the oscillatory values of the sideslip derivatives are presented. Since the y axes of the body and stability system of axes are coincident, the derivatives $C_{Y_{\dot{\beta}}}$, $C_{m_{\alpha}}$, and $C_{m_q} + C_{m_{\dot{\alpha}}}$ are the same in either system of axes.

REFERENCES

1. Beam, Benjamin H.: A Wind-Tunnel Test Technique for Measuring the Dynamic Rotary Stability Derivatives at Subsonic and Supersonic Speeds. NACA Rep. 1258, 1956. (Supersedes NACA TN 3347)
2. Beam, Benjamin H., Reed, Verlin D., and Lopez, Armando E.: Wind-Tunnel Measurements at Subsonic Speeds of the Static and Dynamic-Rotary Stability Derivatives of a Triangular-Wing Airplane Model Having a Triangular Vertical Tail. NACA RM A55A28, 1955.
3. Smith, Willard G.: Wind-Tunnel Investigation at Subsonic and Supersonic Speeds of a Fighter Model Employing a Low-Aspect-Ratio Unswept Wing and a Horizontal Tail Mounted Well Above the Wing Plane - Longitudinal Stability and Control. NACA RM A54D05, 1954.
4. Wetzel, Benton E.: Wind-Tunnel Investigation at Subsonic and Supersonic Speeds of a Fighter Model Employing a Low-Aspect-Ratio Unswept Wing and a Horizontal Tail Mounted Well Above the Wing Plane - Lateral and Directional Stability. NACA RM A54H26b, 1955.
5. Sleeman, William C., Jr., and Wiggins, James W.: Experimental Investigation at High Subsonic Speeds of the Rolling Stability Derivatives of a Complete Model with an Aspect-Ratio-2.52 Wing Having an Unswept 72-Percent-Chord Line and a High Horizontal Tail. NACA RM L54I20, 1955.
6. Glauert, H.: The Elements of Aerofoil and Airscrew Theory. The University Press, Cambridge, England, 1926, ch. XIV.
7. Herriot, John G.: Blockage Corrections for Three-Dimensional-Flow Closed-Throat Wind Tunnels With Consideration of the Effects of Compressibility. NACA Rep. 995, 1950. (Formerly NACA RM A7B28)
8. Runyan, Harry L., Woolston, Donald S., and Rainey, A. Gerald: Theoretical and Experimental Investigation of the Effect of Tunnel Walls on the Forces on an Oscillating Airfoil in Two-Dimensional Subsonic Compressible Flow. NACA TN 3416, 1955. (Formerly NACA RM L52IL7a)
9. Beam, Benjamin H.: The Effects of Oscillation Amplitude and Frequency on the Experimental Damping in Pitch of a Triangular Wing Having an Aspect Ratio of 4. NACA RM A52G07, 1952.
10. Perkins, Courtland D., and Hage, Robert E.: Airplane Performance Stability and Control. John Wiley and Sons, Inc., New York, 1949.

11. Sleeman, William C., Jr.: An Experimental Study at High Subsonic Speeds of Several Tail Configurations on a Model With an Unswept Wing. NACA RM L56A06a, 1956.
12. Anon.: Flying Qualities of Piloted Airplanes. U. S. Air Force Spec., MIL-F-8785(ASG), Sept. 1, 1954.
13. Campbell, John P., and McKinney, Marion O.: Summary of Methods for Calculating Dynamic Lateral Stability and Response and for Estimating Lateral Stability Derivatives. NACA Rep. 1098, 1952.
14. McNeill, Walter E., and Creer, Brent Y.: A Summary of Results Obtained During Flight Simulation of Several Aircraft Prototypes With Variable-Stability Airplanes. NACA RM A56C08, 1956.
15. Tobak, Murray, Reese, David E., Jr., and Beam, Benjamin H.: Experimental Damping in Pitch of 45° Triangular Wings. NACA RM A50J26, 1950.
16. Thomas, H. H. B. M., and Spencer, B. F. R.: The Calculations of the Derivatives Involved in the Damping of the Longitudinal Short Period Oscillations of an Aircraft and Correlation With Experiment. British R.A.E. Rep. Aero 2561, Nov. 1955.
17. Wiggins, James W.: Wind-Tunnel Investigation at High Subsonic Speeds to Determine the Rolling Derivatives of Two Wing-Fuselage Combinations Having Triangular Wings, Including a Semiempirical Method of Estimating the Rolling Derivatives. NACA RM L53L18a, 1954.

TABLE I.- MODEL DIMENSIONS

Wing (basic plan form, leading and trailing edges extended to plane of symmetry)	
Span, b, ft	2.16
Area, S, sq ft	1.90
Mean aerodynamic chord, \bar{c} , ft	0.94
Aspect ratio	2.44
Leading-edge sweep, deg	27.00
Taper ratio	0.38
Incidence, deg	0
Dihedral, deg	-10
Airfoil section	
Forward 50-percent chord (forward 2.5 percent modified to form sharp leading edge)	elliptical
Rear 50-percent chord	biconvex
Thickness ratio	0.034
Horizontal tail	
Span, ft	1.20
Area, sq ft	0.48
Mean aerodynamic chord, ft	0.44
Aspect ratio	2.97
Taper ratio	0.31
Leading-edge sweep, deg	19.81
Length (distance between 0.25 \bar{c} points), ft	1.67
Height, ft	0.69
Airfoil section	
Forward 50-percent chord	elliptical
Rear 50-percent chord	biconvex
Thickness ratio	0.05
Vertical tail (leading and trailing edges extended to body center line)	
Span, ft	0.69
Area, sq ft	0.56
Mean aerodynamic chord, ft	0.87
Aspect ratio	0.86
Taper ratio	0.37
Leading-edge sweep, deg	43.96
Length (distance between 0.25 \bar{c} points), ft	1.20
Height, ft	0.29
Airfoil section	
Forward 50-percent chord	elliptical
Rear 50-percent chord	biconvex
Thickness ratio	
Root	0.043
Tip	0.050
Body	
Length, ft	4.65
Base area, sq ft	0.13
Moment center (on body center line)	
Horizontal location (aft of leading edge of \bar{c}), percent \bar{c}	25

TABLE II.- ASSUMED GEOMETRIC AND MASS DATA
FOR REPRESENTATIVE AIRPLANE

Geometric data	
Model scale (wing area 189.6 sq ft)	0.10
Mass data	
Weight, lb	14,150
I_{x_0} , slug-ft ²	3,120
I_{y_0} , slug-ft ²	40,100
I_{z_0} , slug-ft ²	41,100
Inclination of the principal longitudinal axis below the fuselage reference line, deg	
	3
Center of gravity position, percent \bar{c}	25
where: I_{x_0} , I_{y_0} , I_{z_0} moments of inertia about the principal axes	

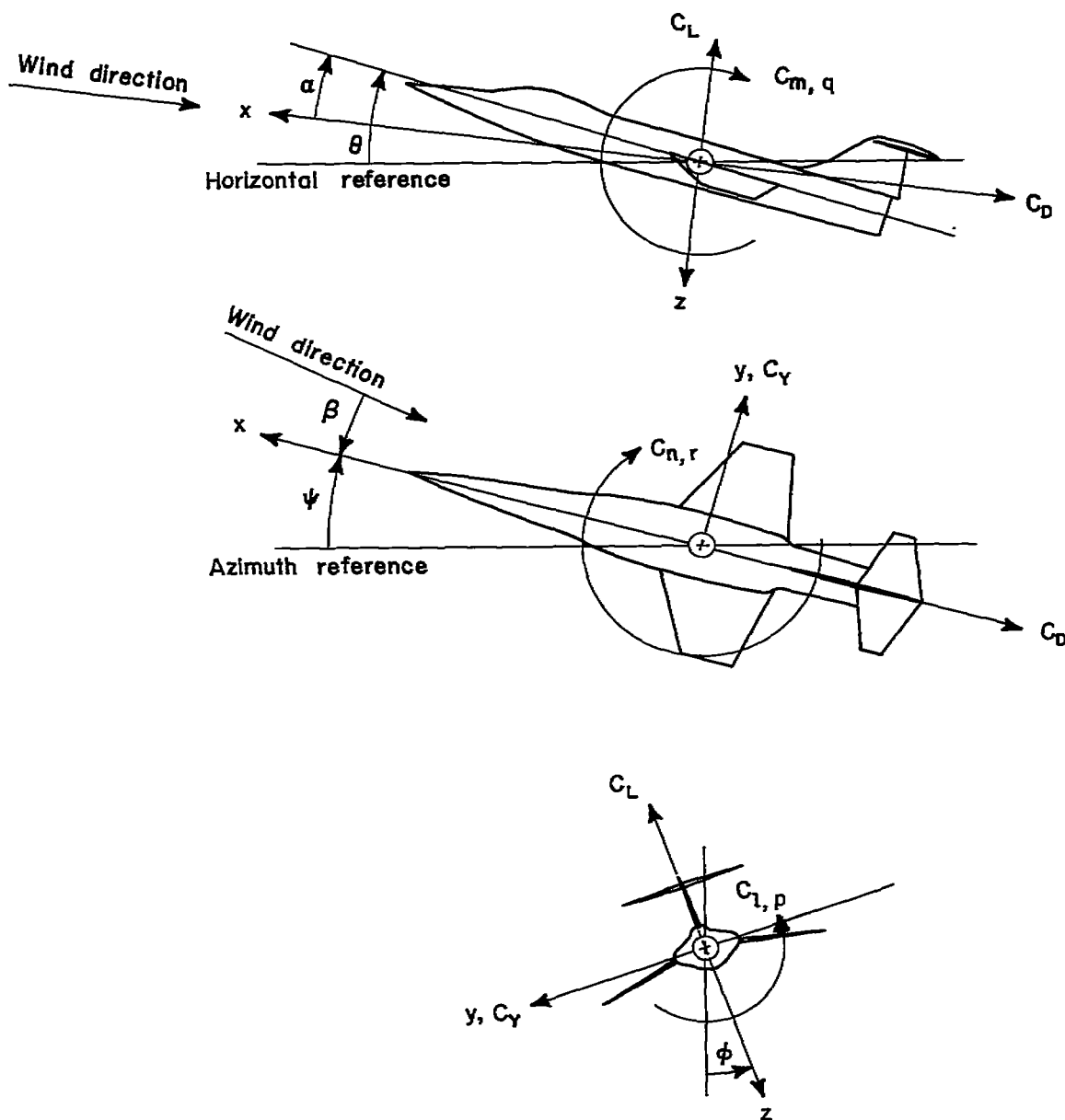


Figure 1.- The stability system of axes: an orthogonal system of axes having its origin at the center of gravity, the z axis in the plane of symmetry and perpendicular to the relative wind, the x axis in the plane of symmetry and perpendicular to the z axis, and the y axis perpendicular to the plane of symmetry. Arrows indicate the positive directions of forces and moments.

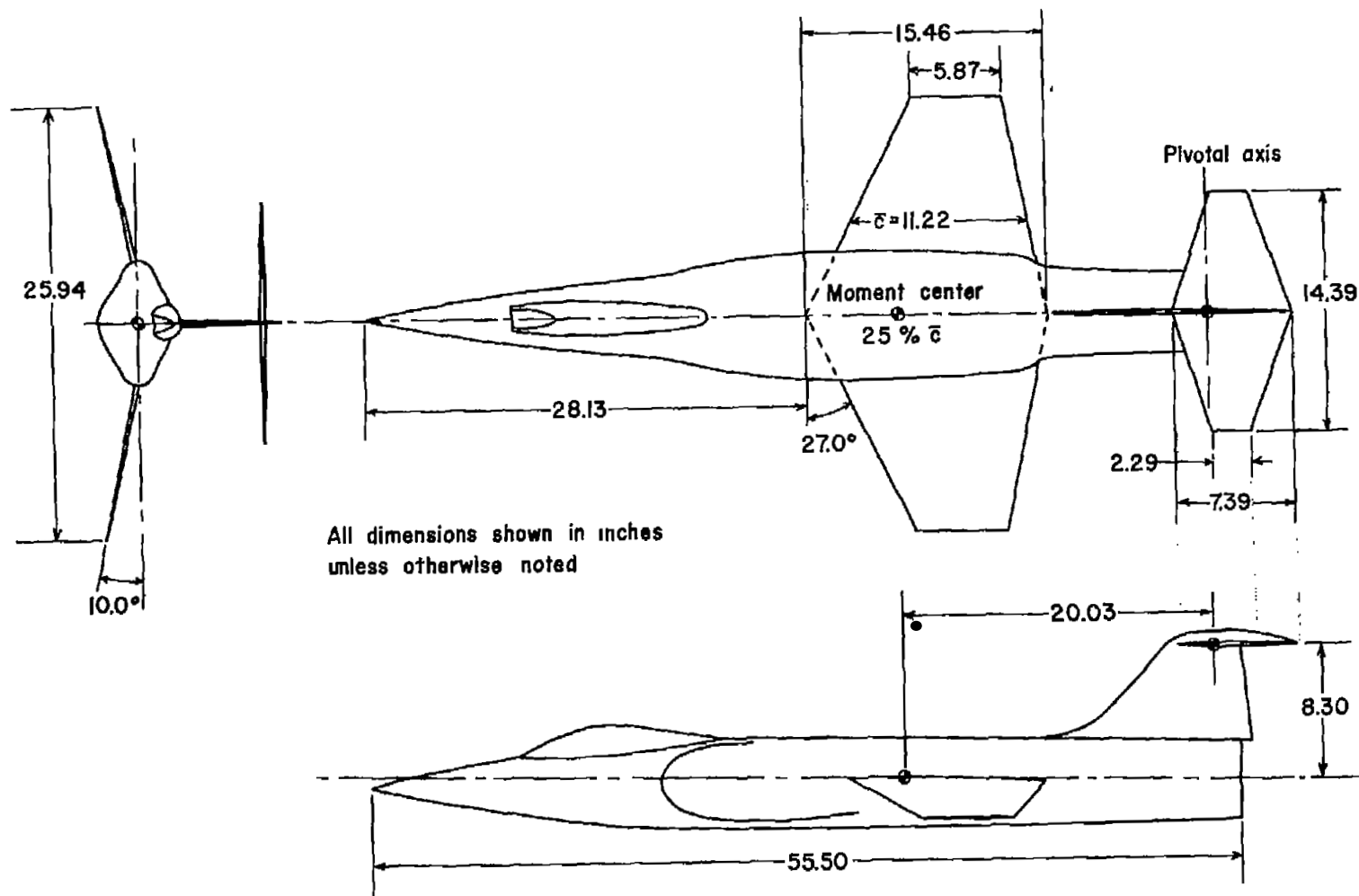
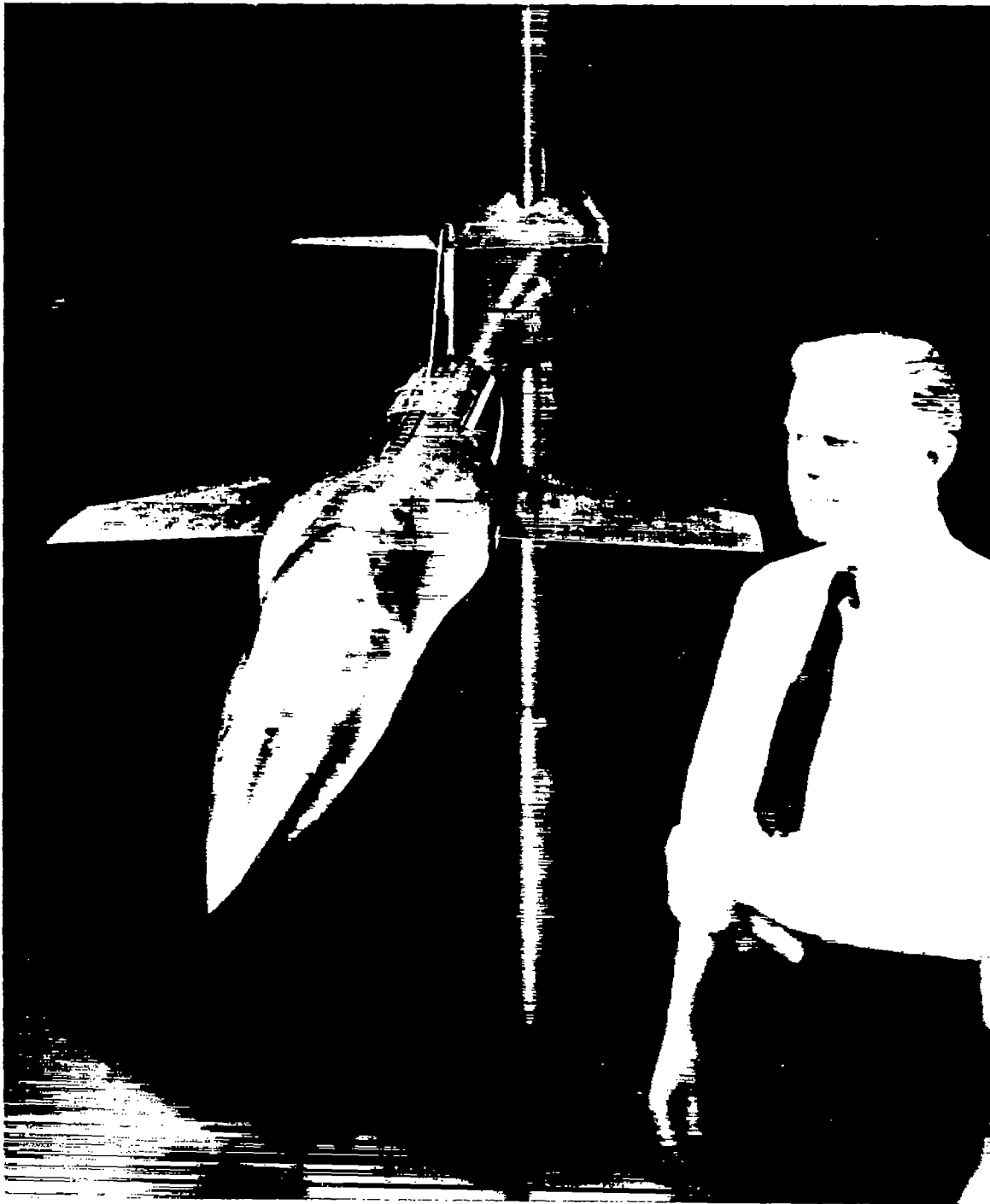


Figure 2.- Three-view drawing of the model.



A-20177.1

Figure 3.- Photograph of the model mounted on the oscillation apparatus.

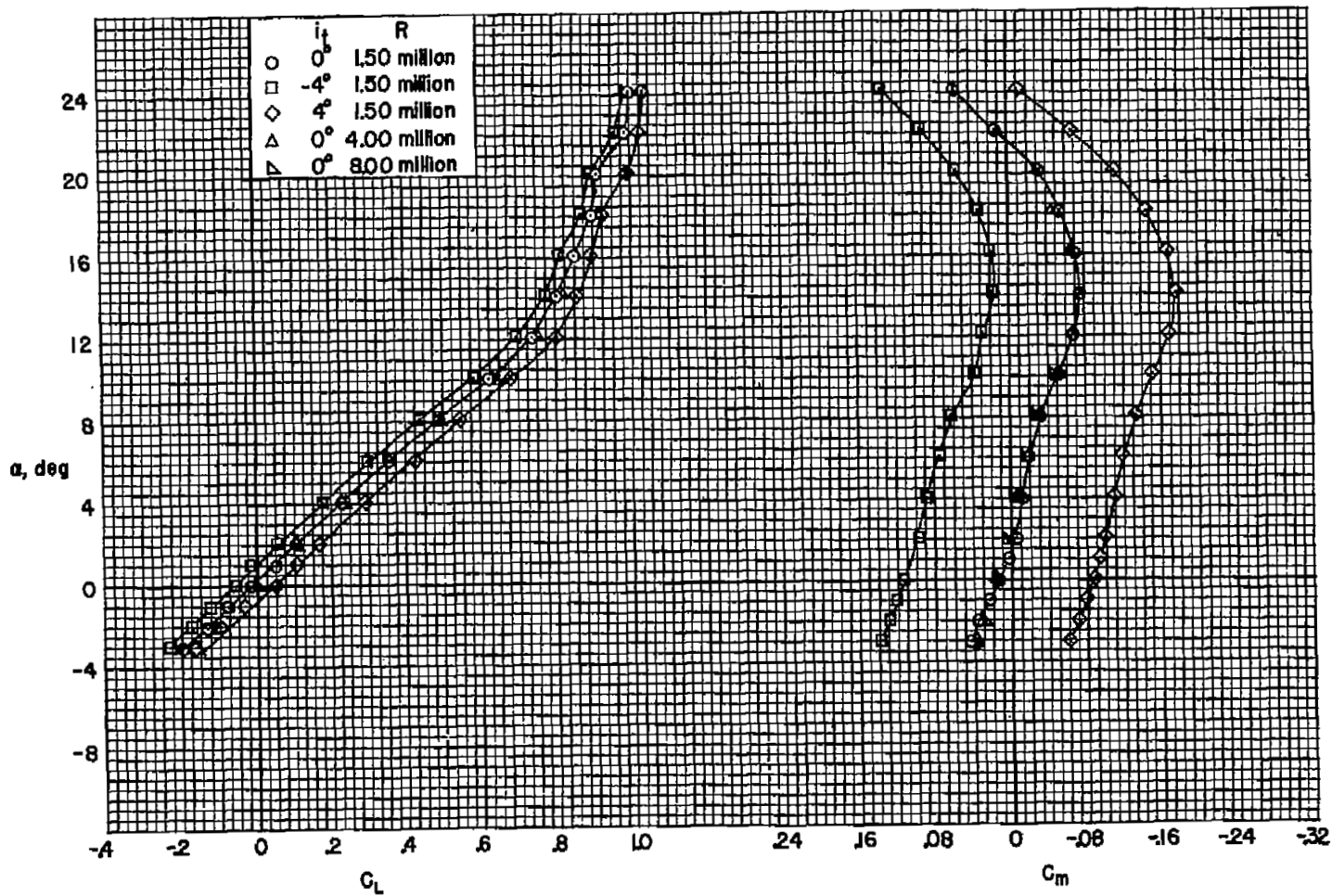
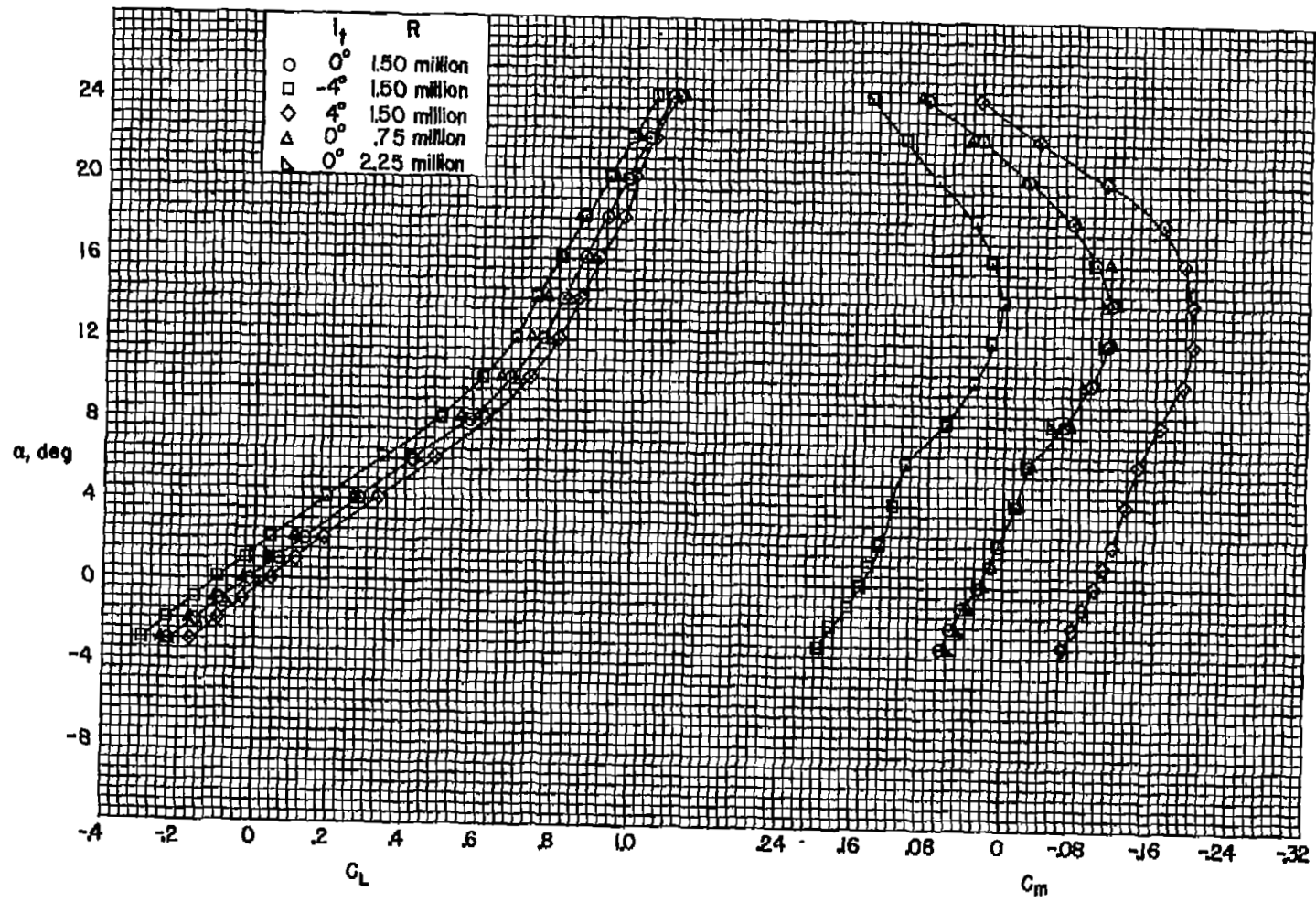
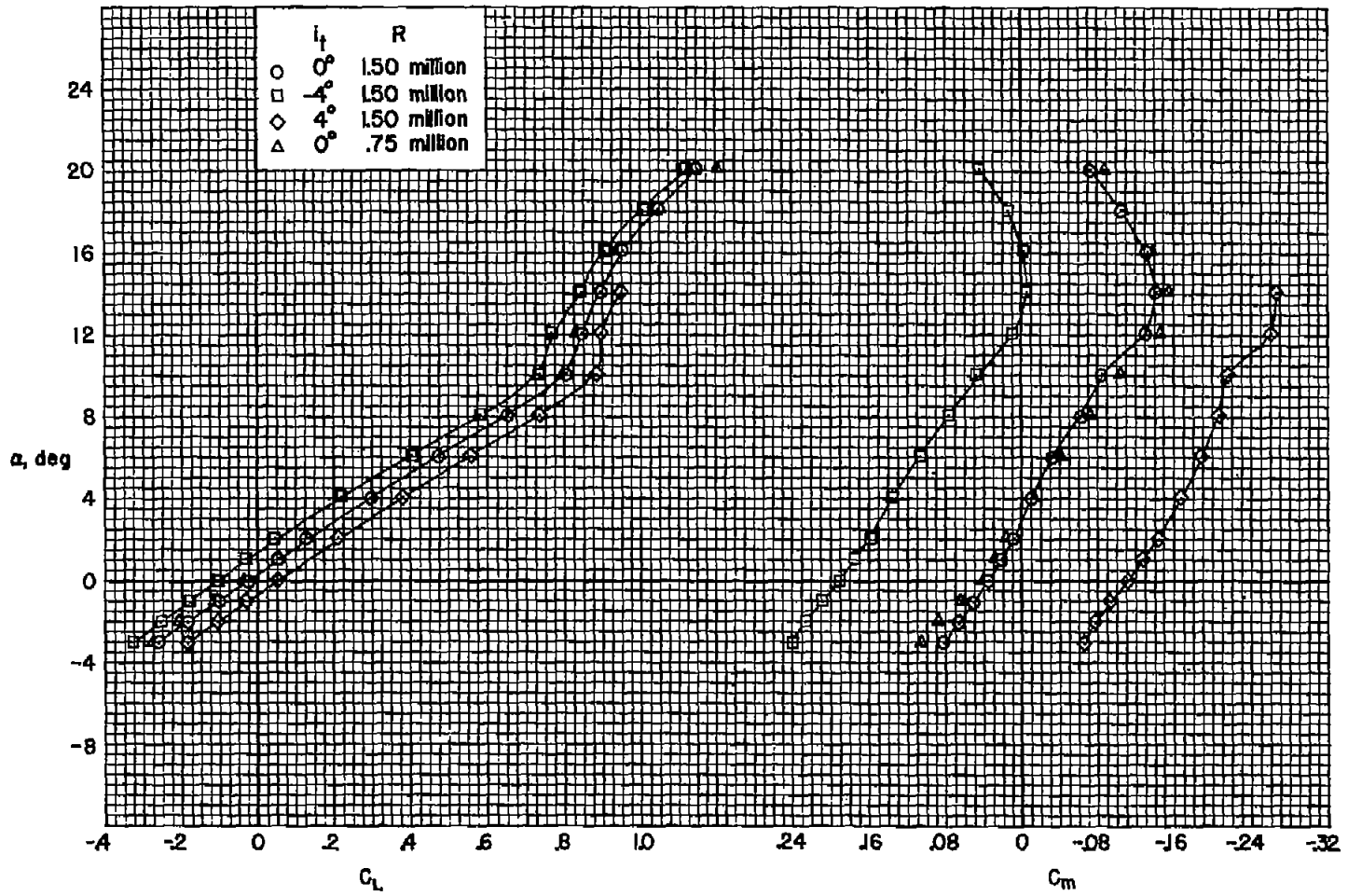
(a) $M = 0.25$

Figure 4.- The lift and pitching-moment characteristics of the complete model; wing dihedral = -10° .



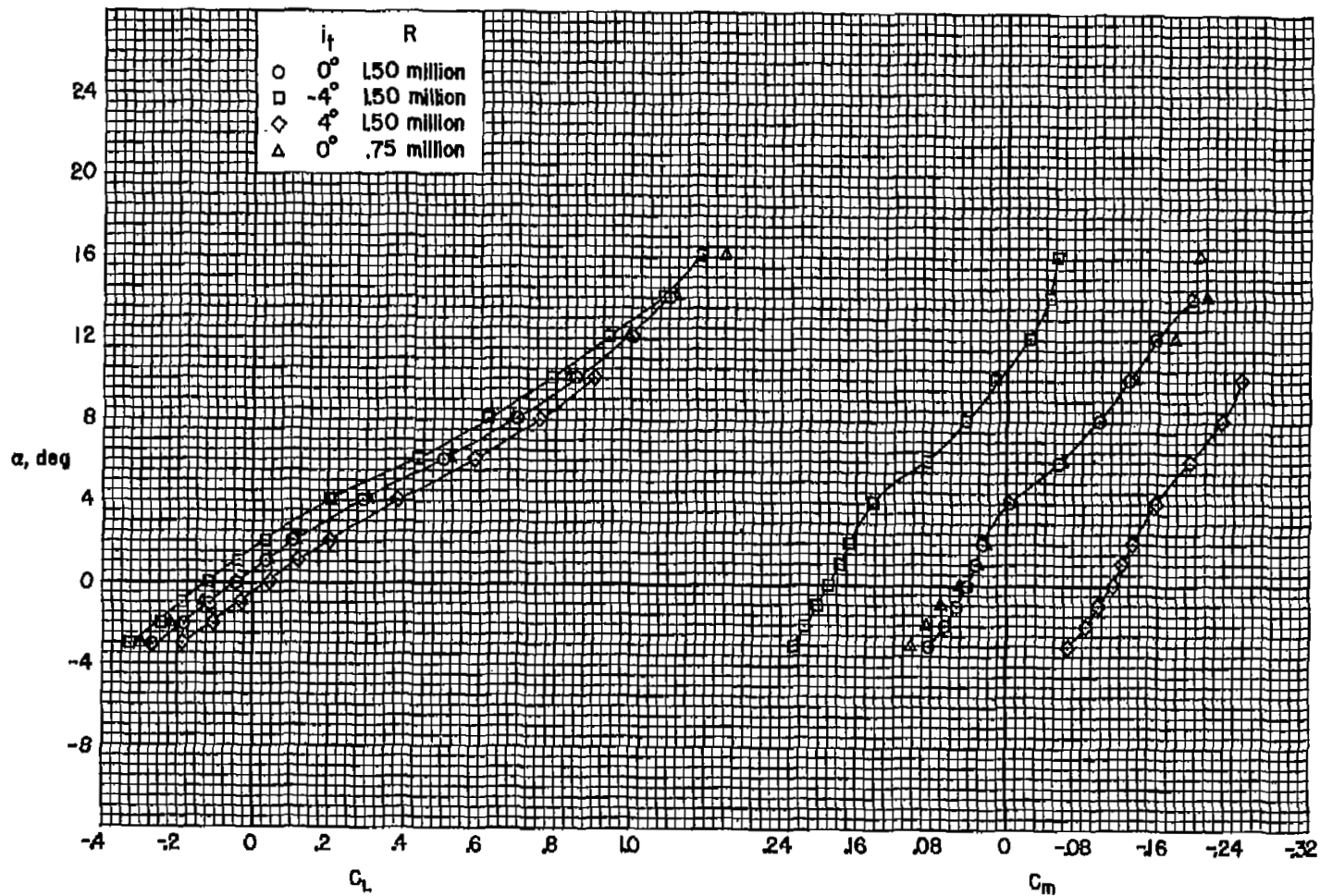
(b) $M = 0.80$

Figure 4.- Continued.



(c) $M = 0.90$

Figure 4.- Continued.



(d) $M = 0.94$

Figure 4.- Concluded.

CONFIDENTIAL

CONFIDENTIAL

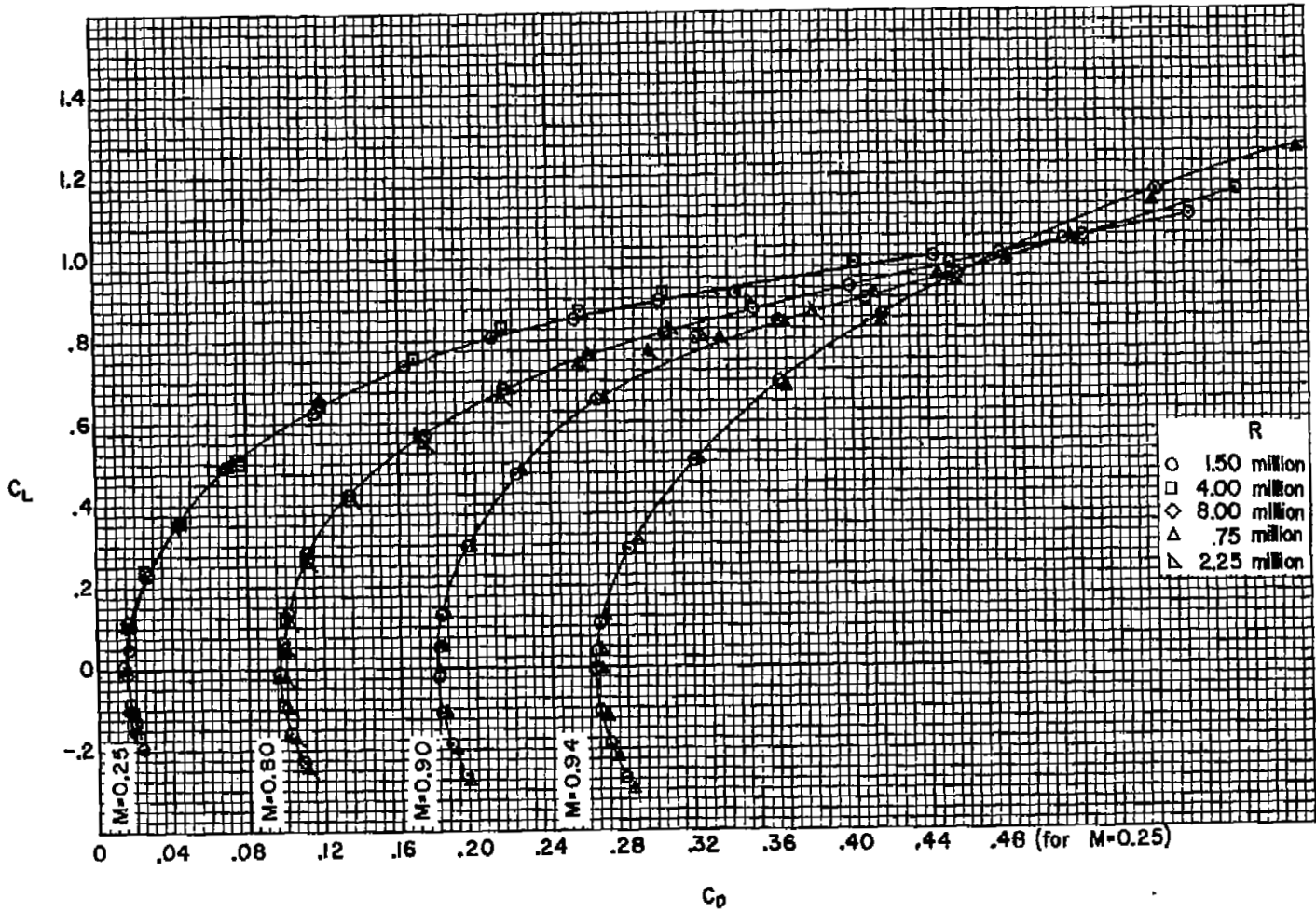
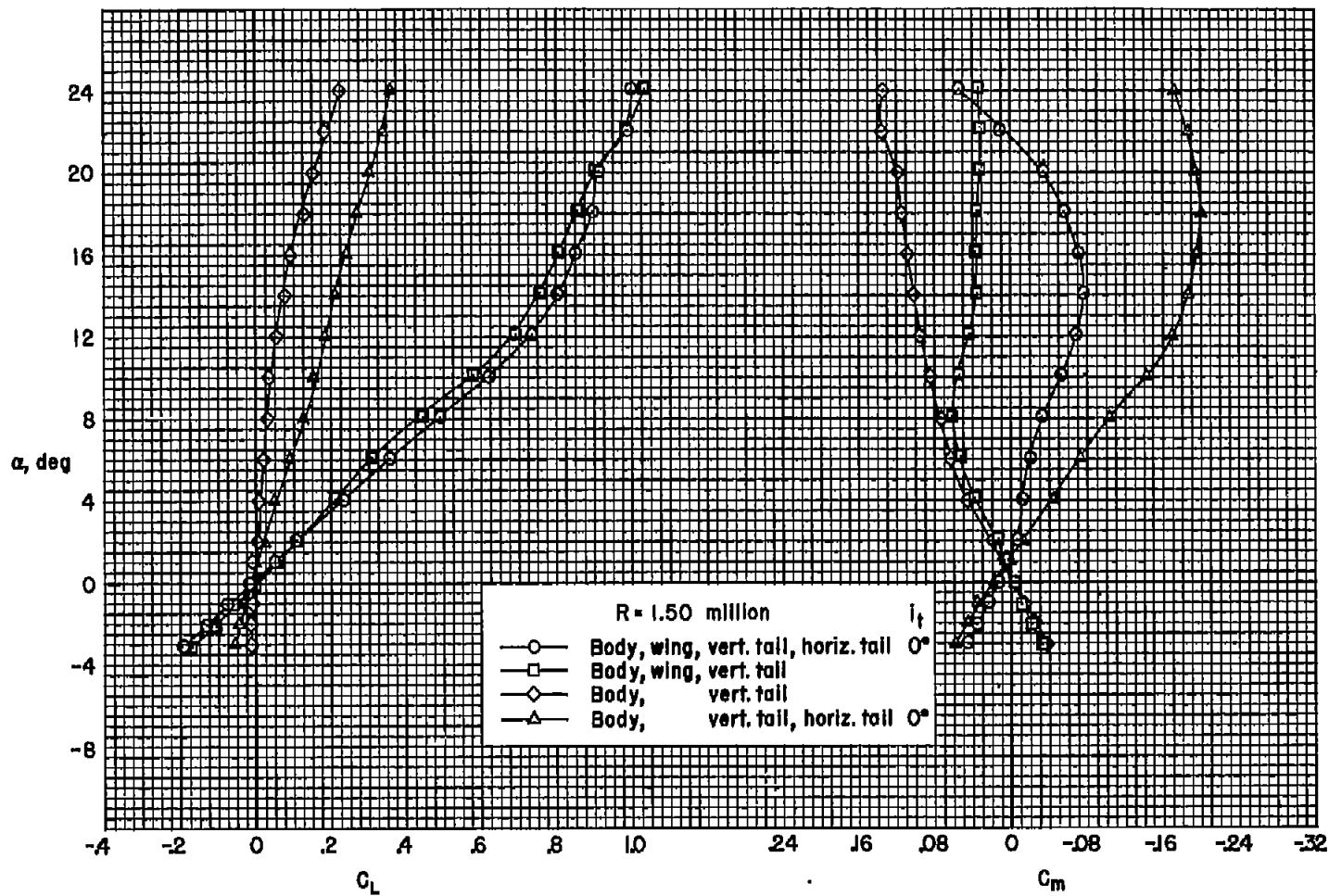


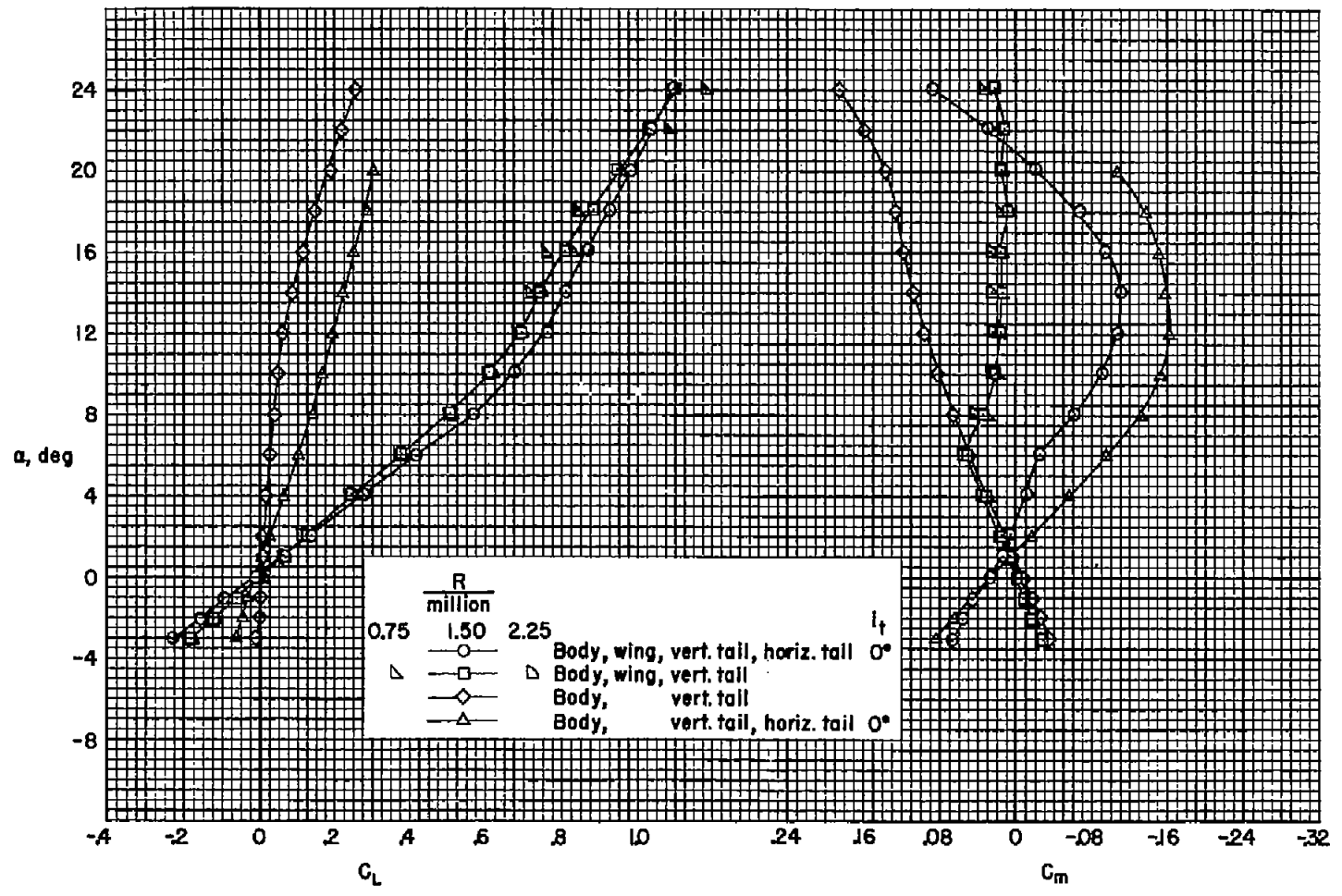
Figure 5.- The drag characteristics of the complete model; wing dihedral = -10° , $i_t = 0^\circ$.

CONFIDENTIAL



(a) $M = 0.25$

Figure 6.- The lift and pitching-moment characteristics for various configurations; wing dihedral = -10° .

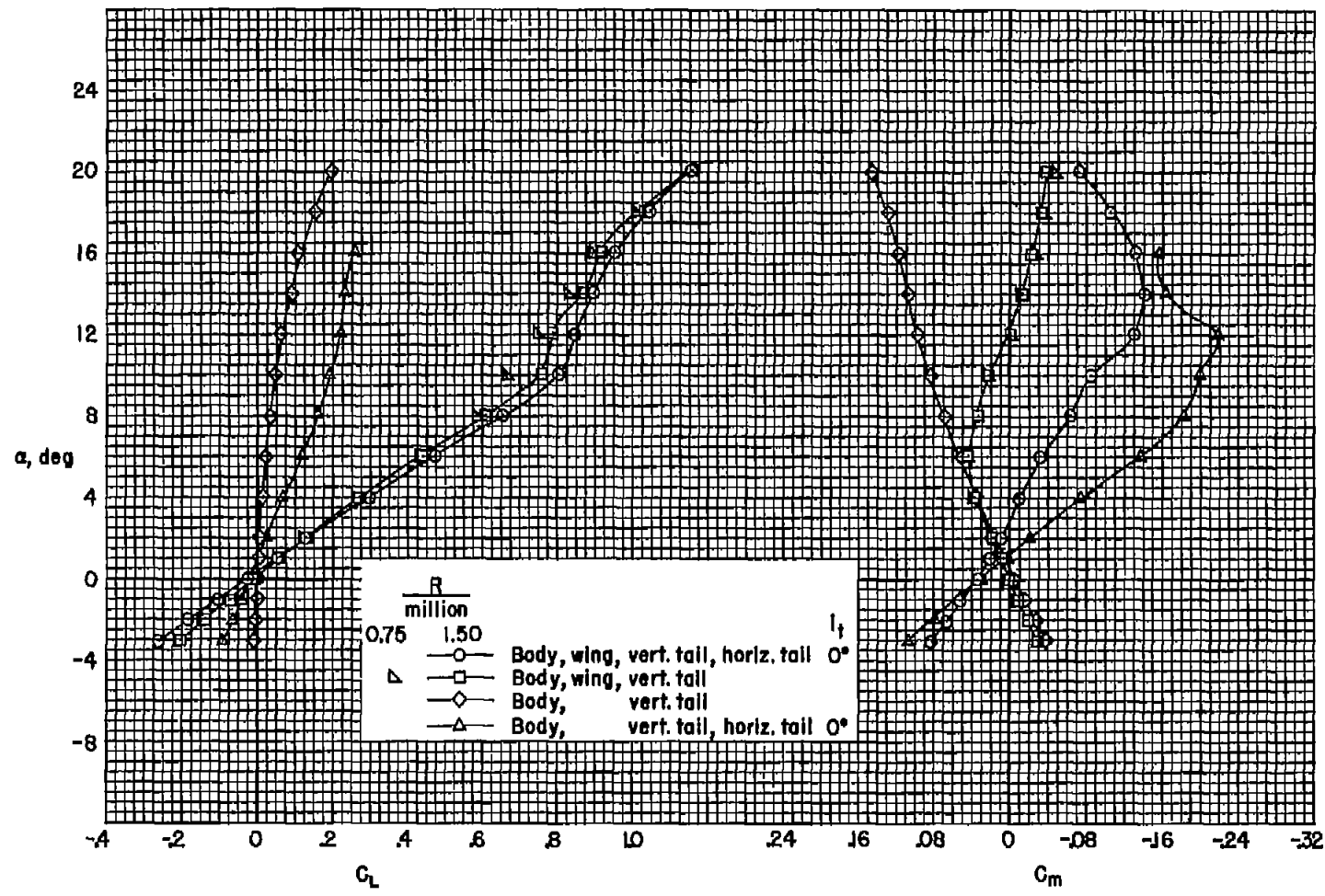


(b) $M = 0.80$

Figure 6.- Continued.

CONFIDENTIAL

CONFIDENTIAL



(c) $M = 0.90$

Figure 6.- Continued.

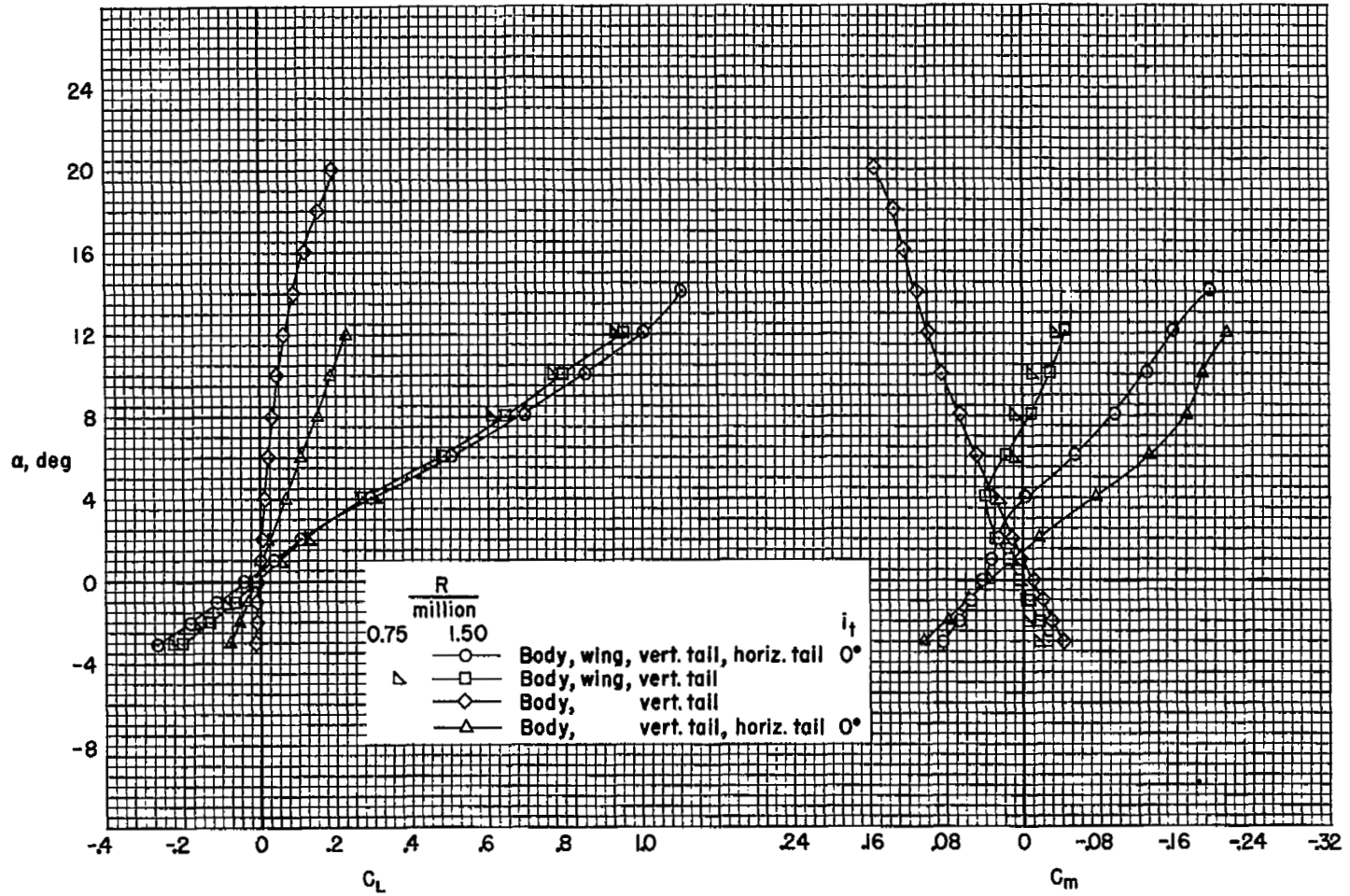
(d) $M = 0.94$

Figure 6.- Concluded.

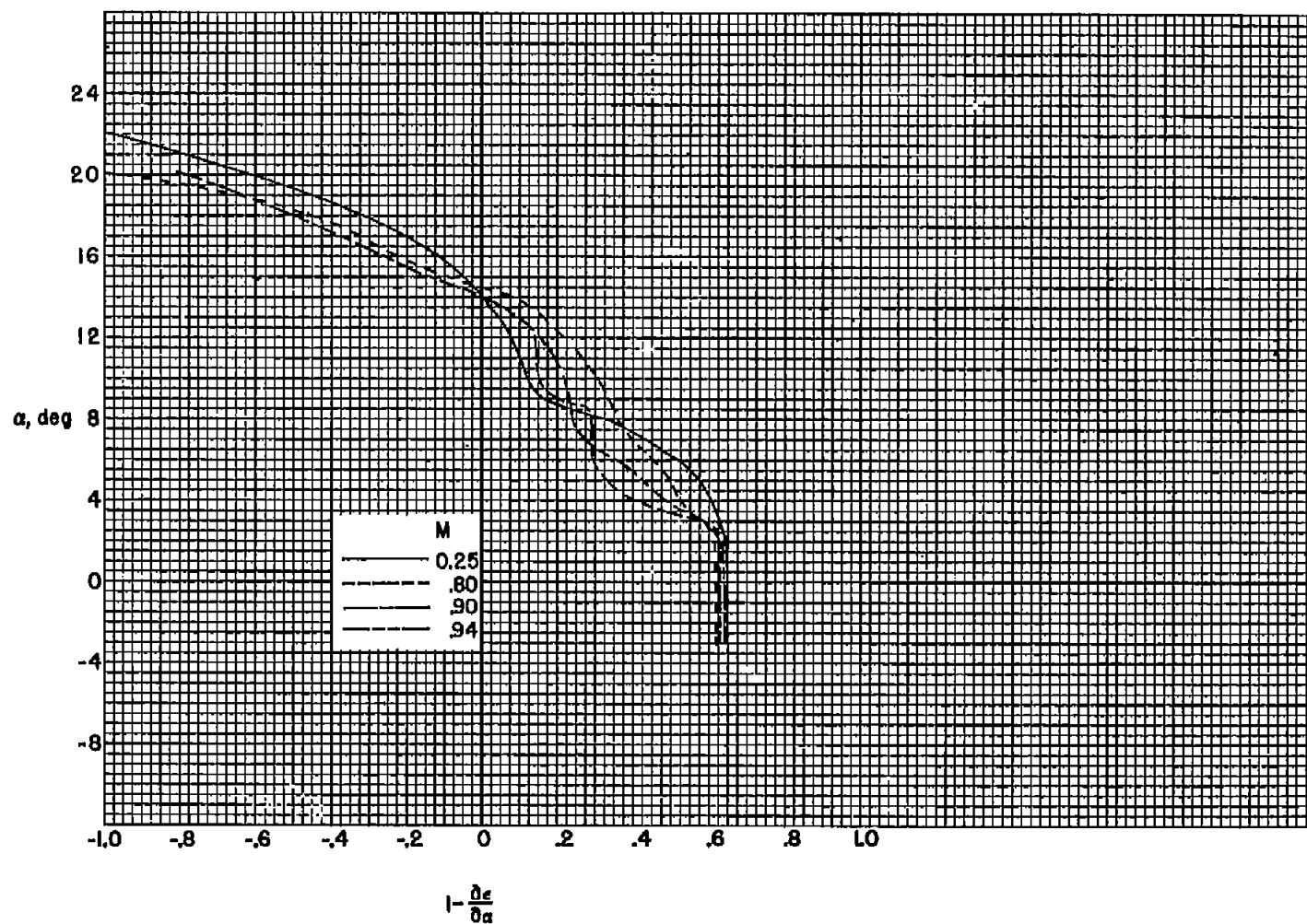


Figure 7.- The variation with angle of attack of the factor, $1 - (\partial \epsilon / \partial \alpha)$; $R = 1.50$ million, wing dihedral = -10° .

CONFIDENTIAL

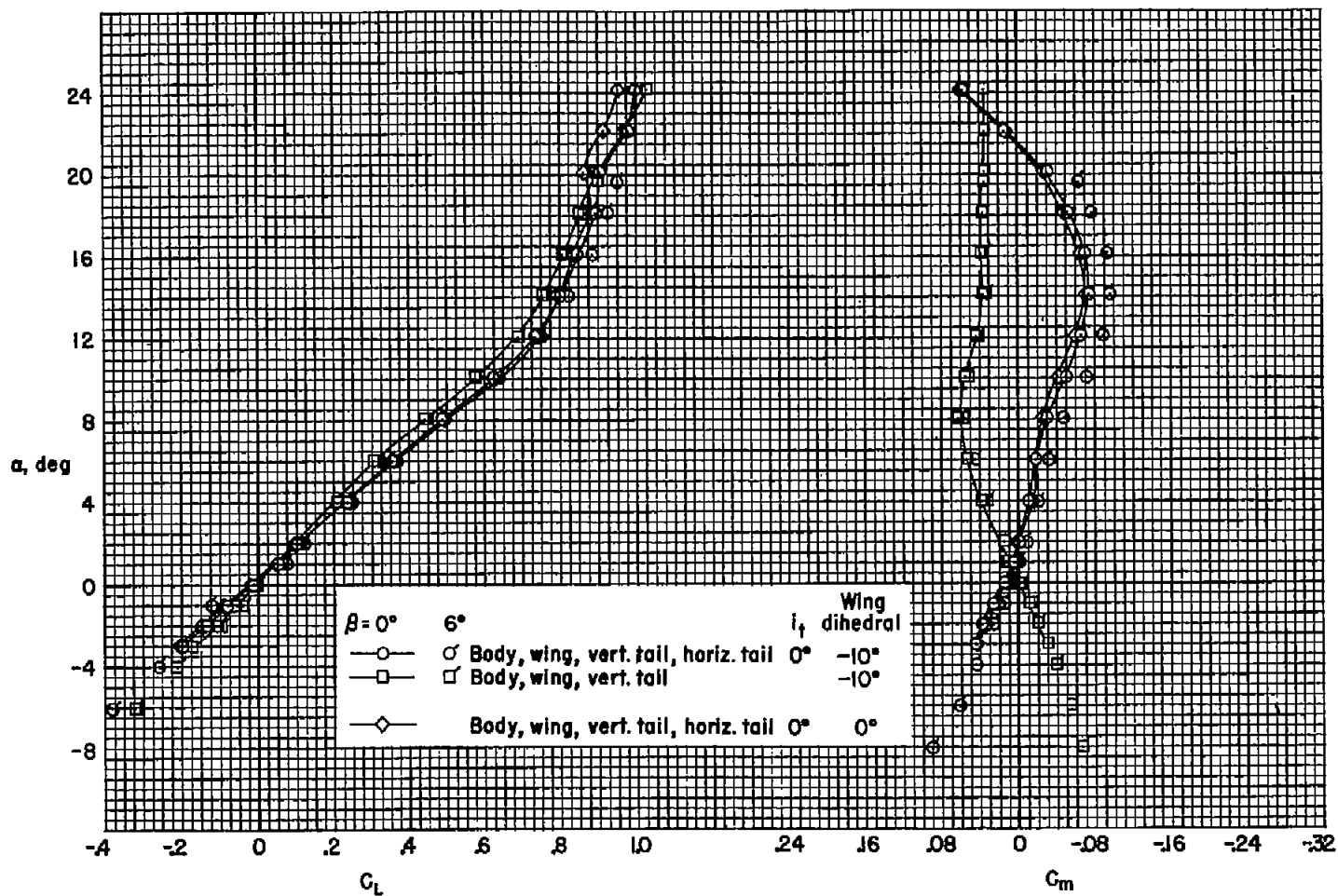
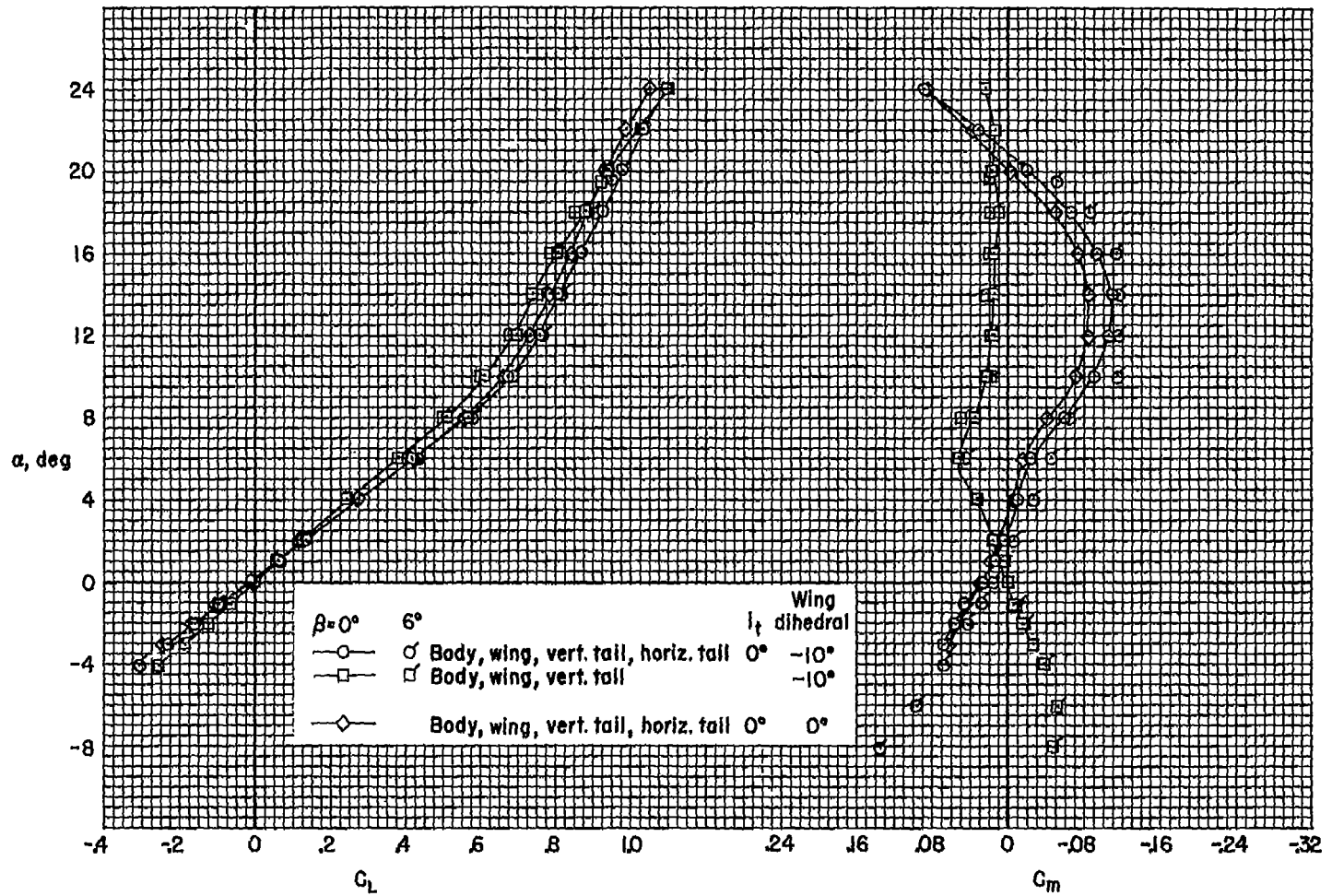
(a) $M = 0.25$

Figure 8.- The lift and pitching-moment characteristics for various angles of sideslip and wing dihedral; $R = 1.50$ million.

14

CONFIDENTIAL

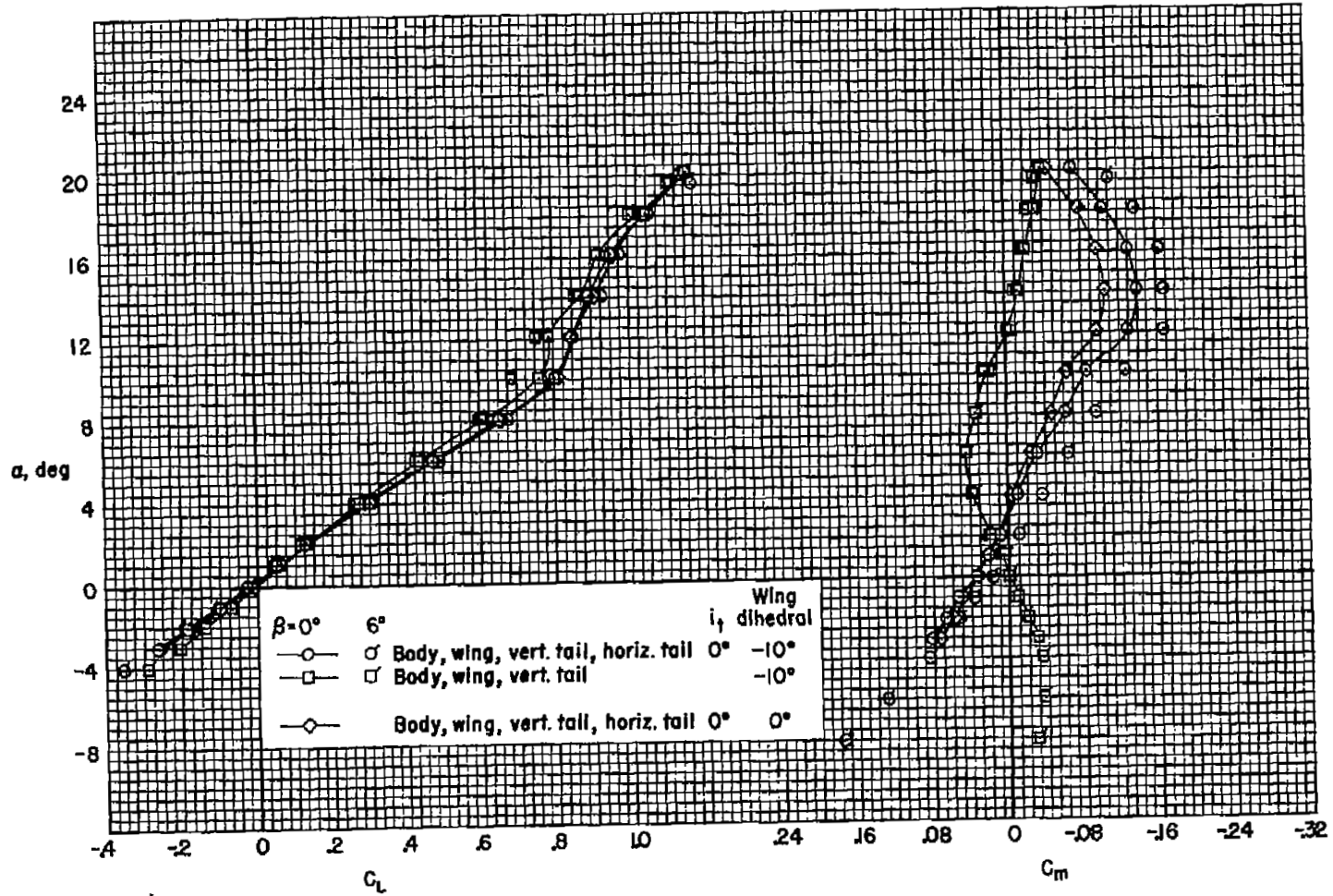
NACA RM A56104



(b) $M = 0.80$

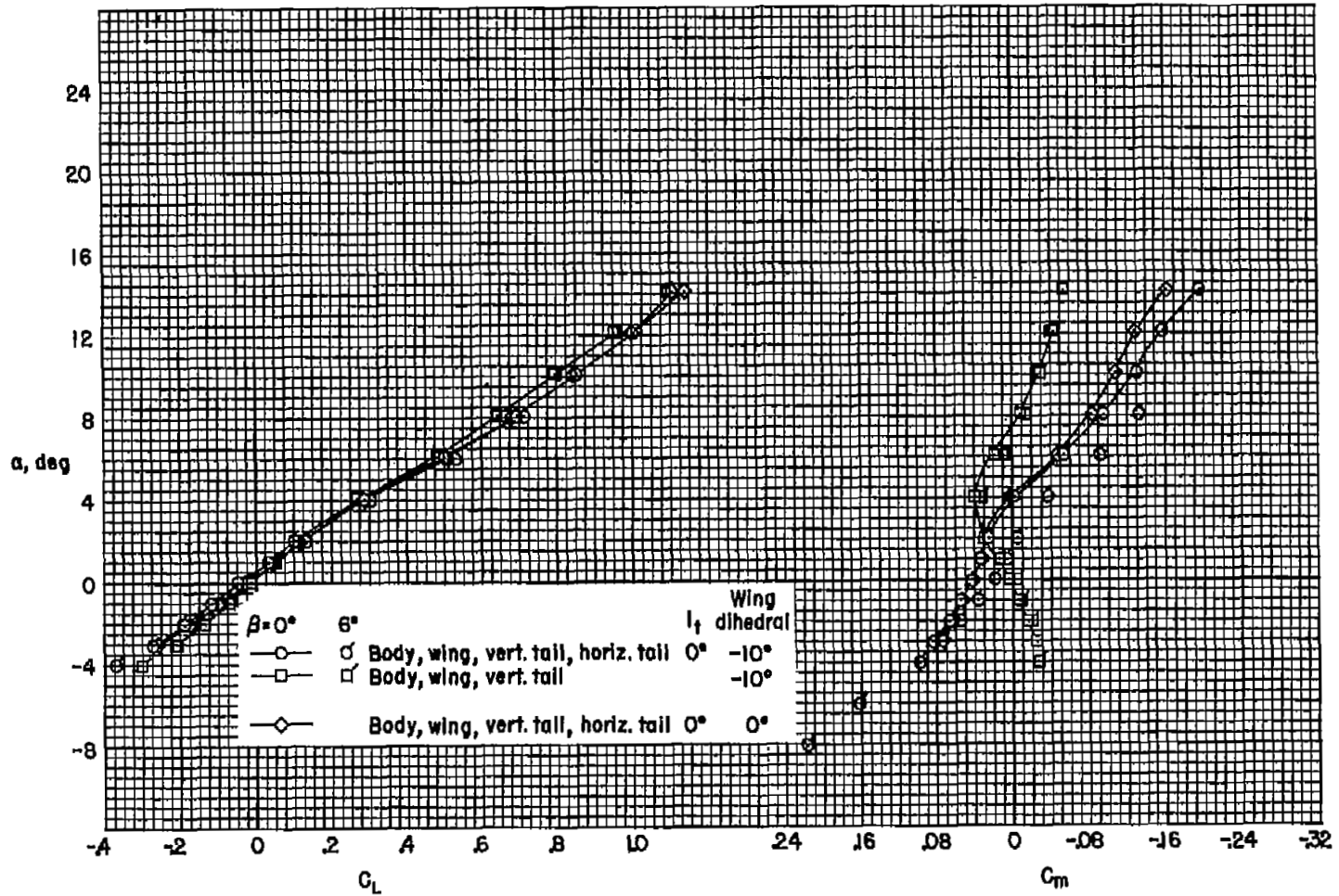
Figure 8.- Continued.

CONFIDENTIAL



(c) $M = 0.90$

Figure 8.- Continued.



(a) $M = 0.94$

Figure 8.- Concluded.

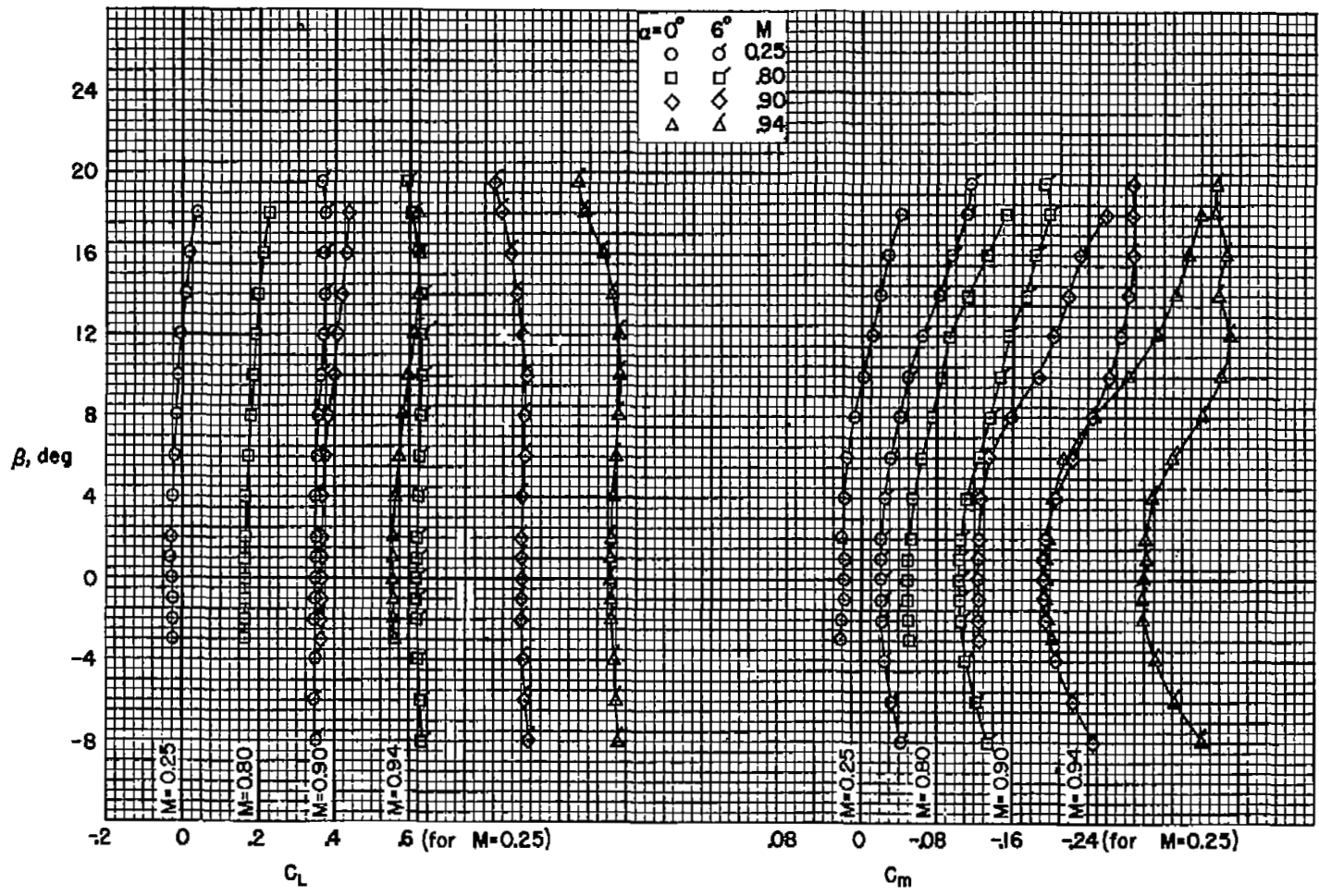


Figure 9.- The variation of lift and pitching-moment coefficients with angle of sideslip for the complete model at two angles of attack; $R = 1.50$ million, wing dihedral = -10° , $i_t = 0^\circ$.

CONFIDENTIAL

CONFIDENTIAL

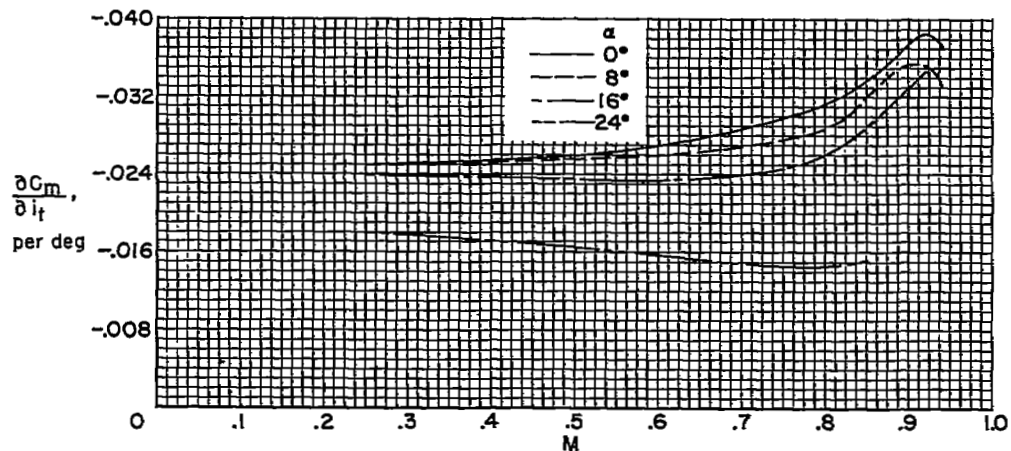
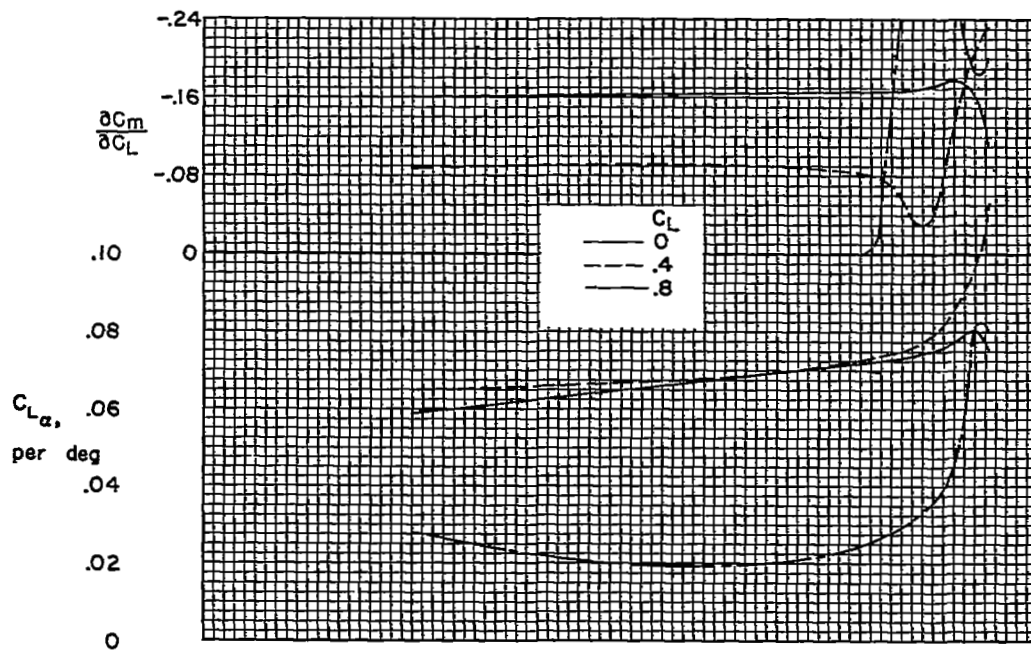


Figure 10.- The variation with Mach number of static longitudinal stability and control parameters for the complete model; $R = 1.50$ million, wing dihedral = -10° , $i_t = 0^\circ$.

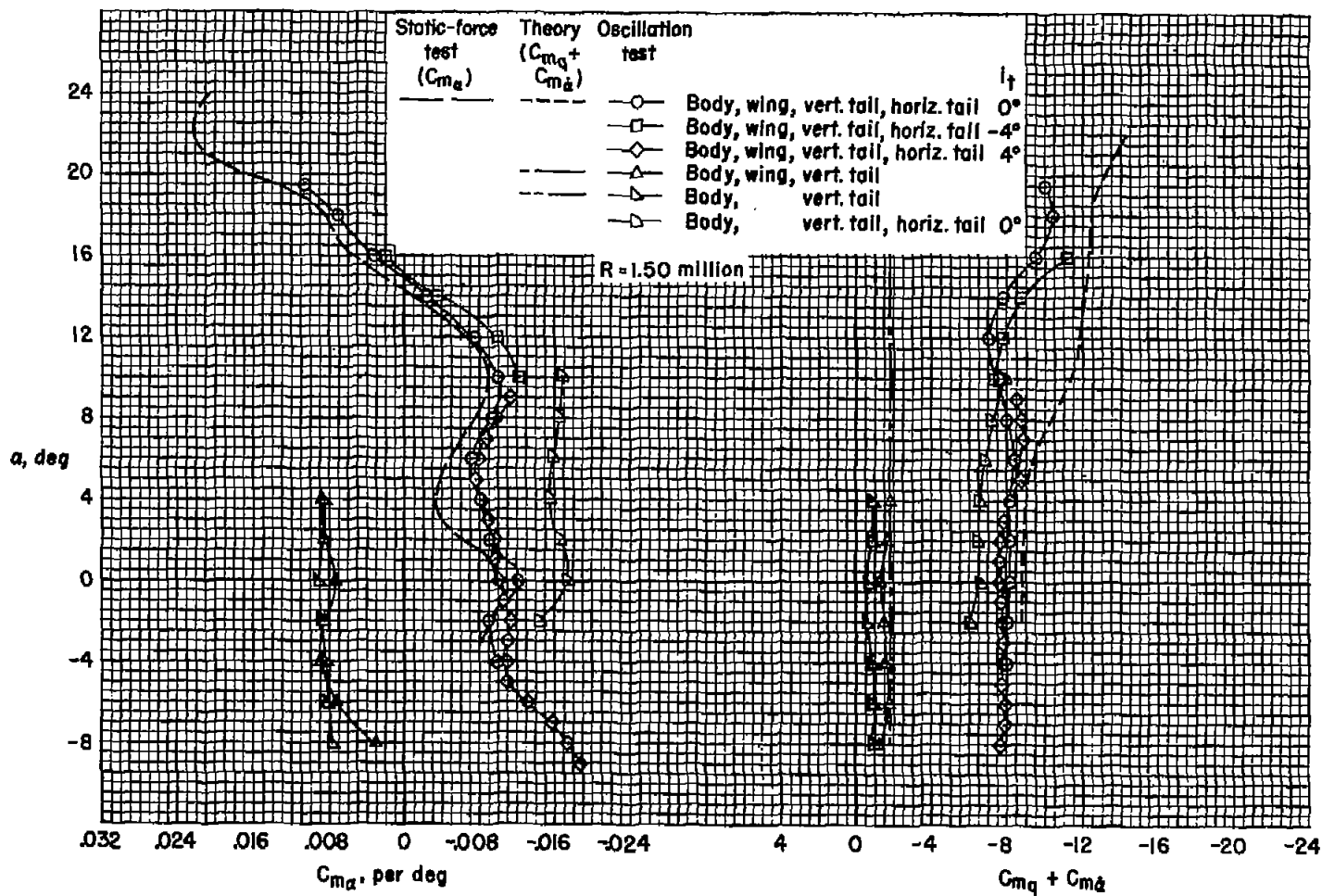
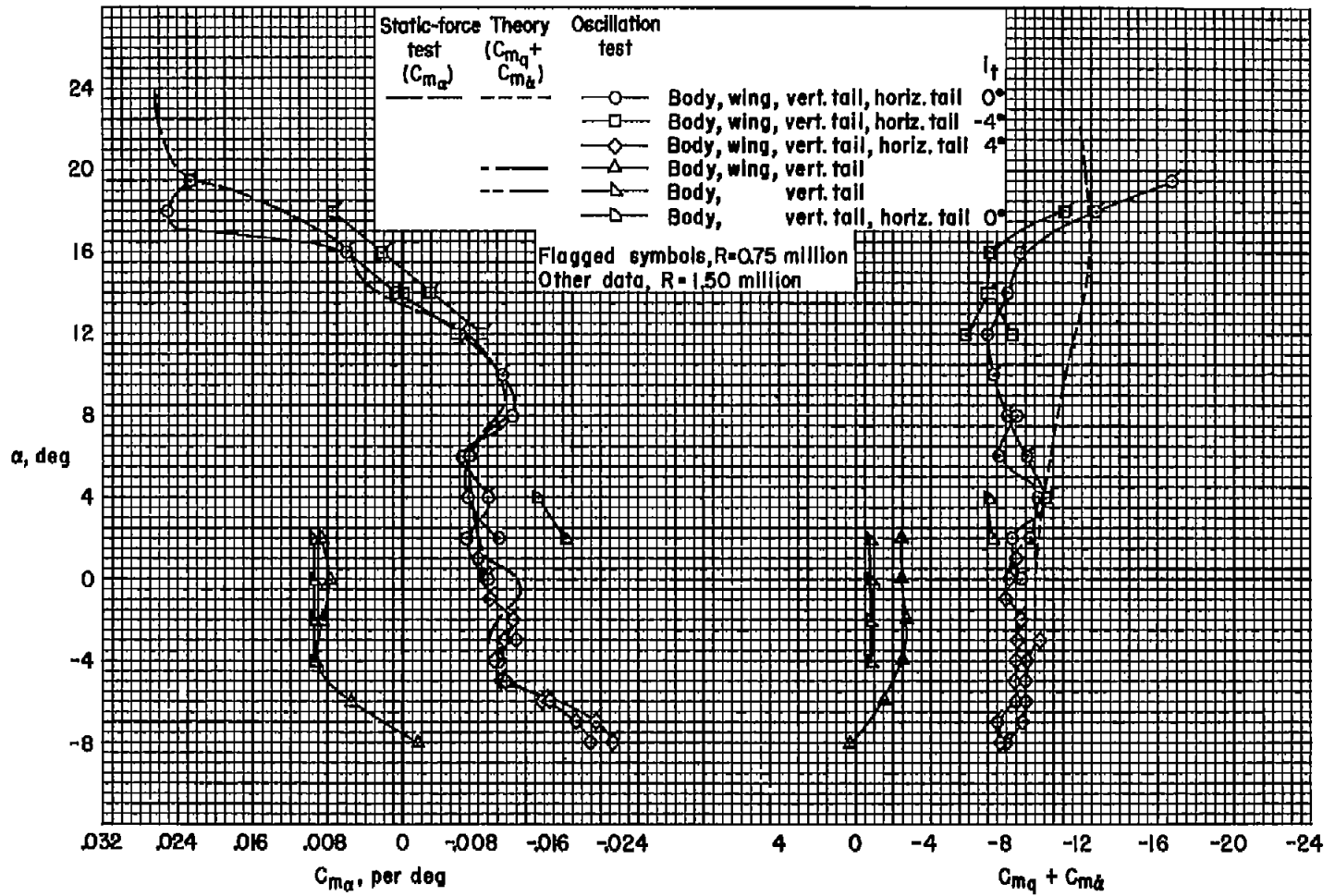
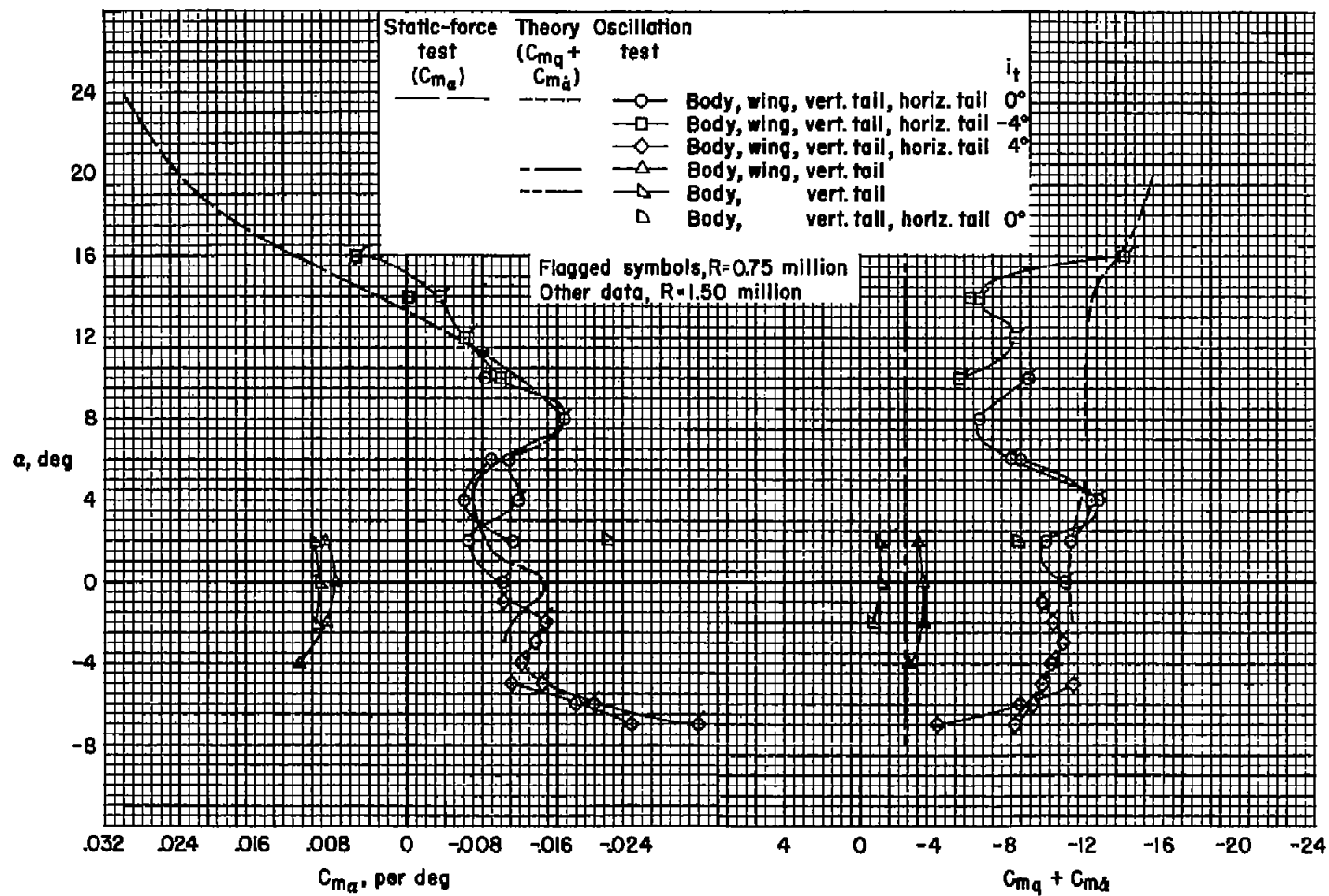
(a) $M = 0.25$

Figure 11.- The longitudinal stability derivatives from oscillation tests; wing dihedral = -10° .

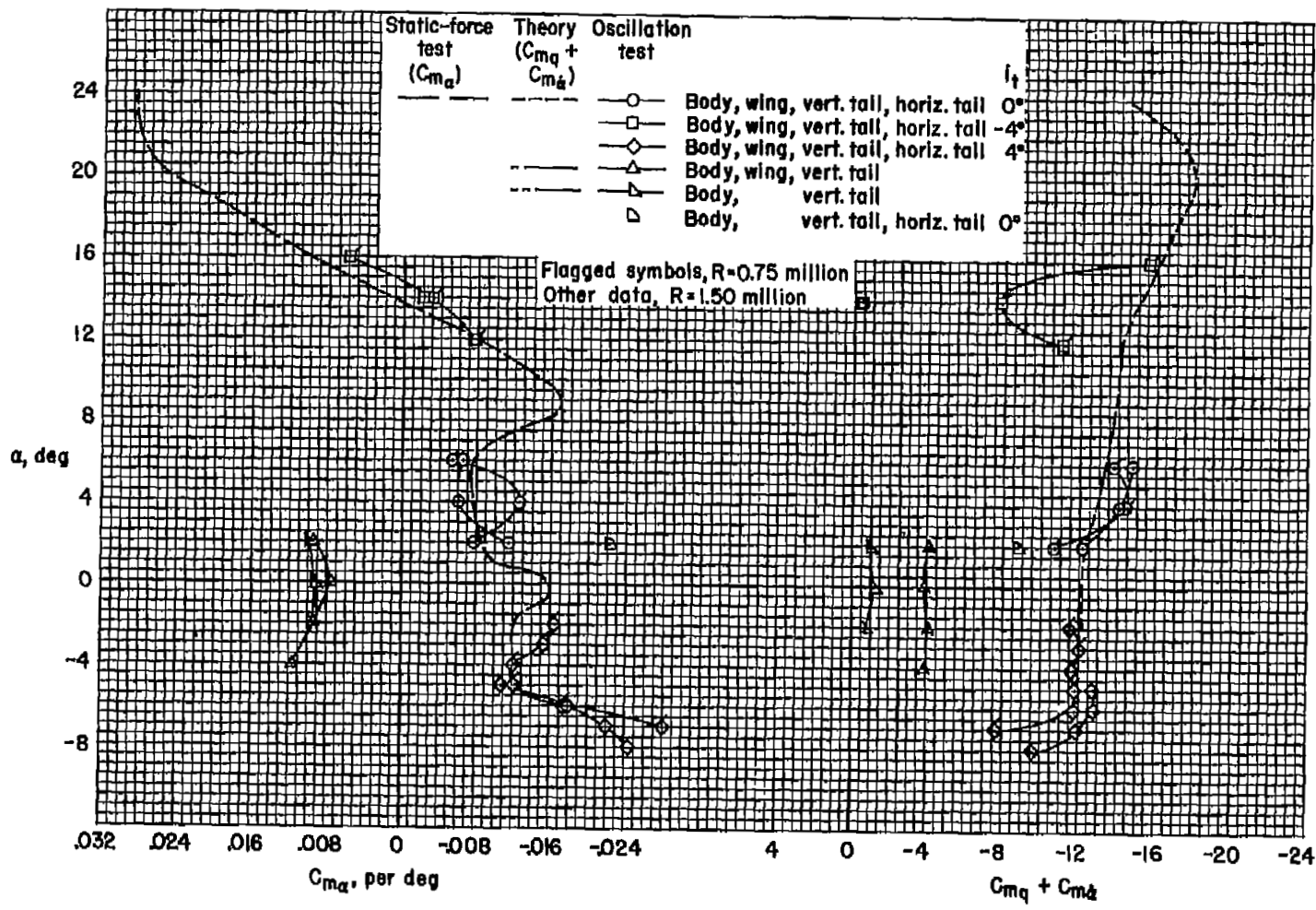


(b) $M = 0.60$

Figure 11.- Continued.



CONFIDENTIAL

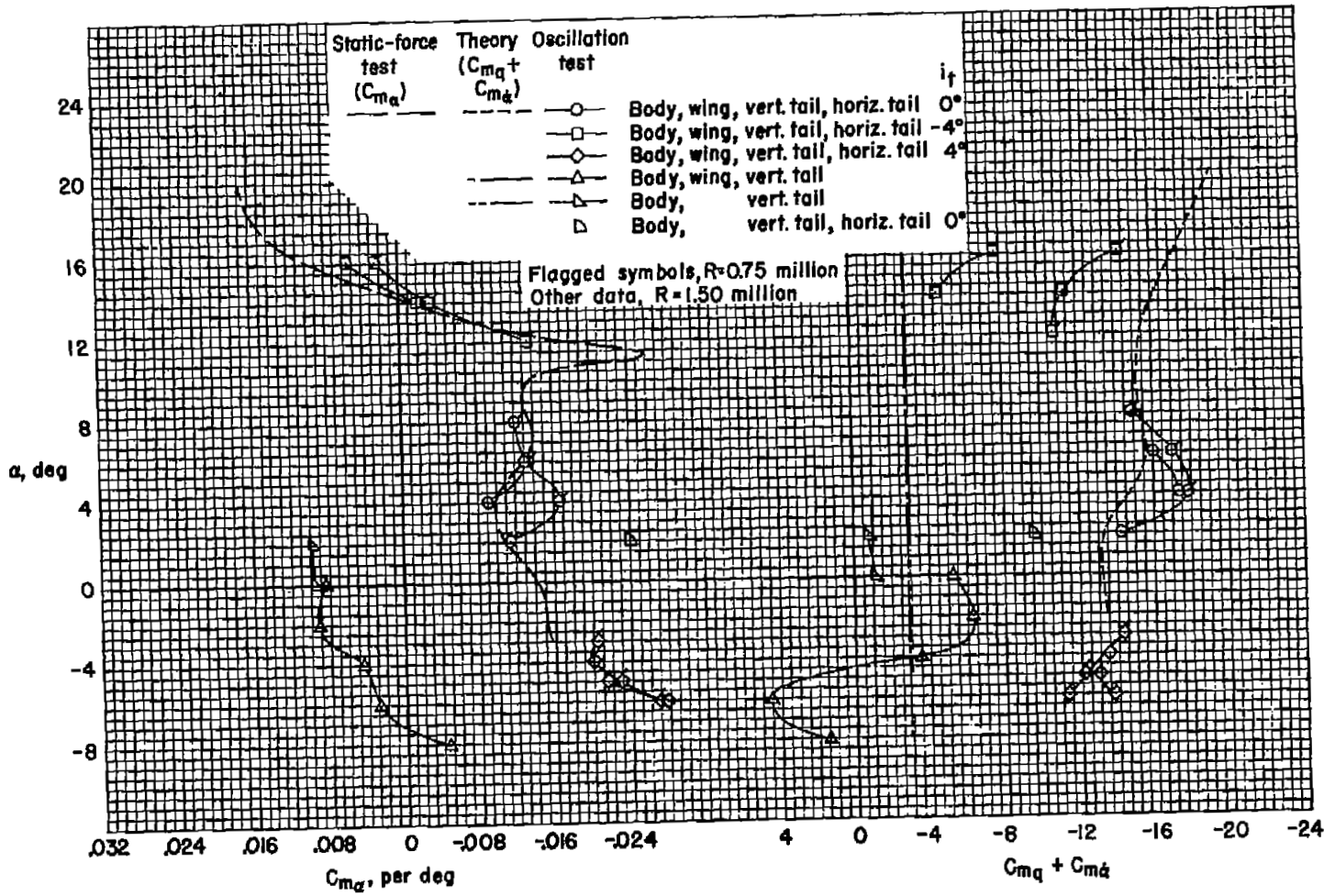


(d) $M = 0.85$

Figure 11.- Continued.

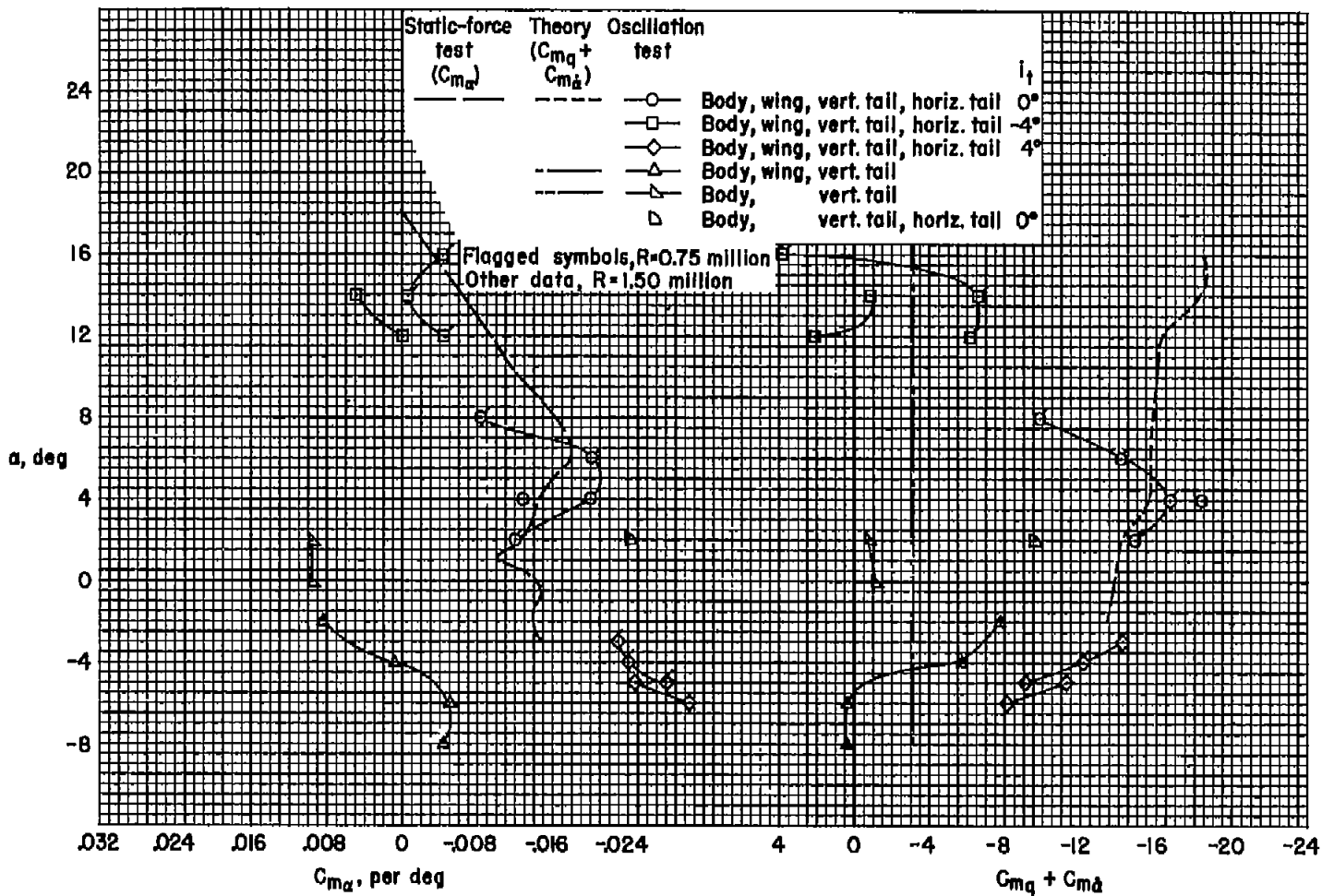
CONFIDENTIAL

CONFIDENTIAL



(e) $M = 0.90$

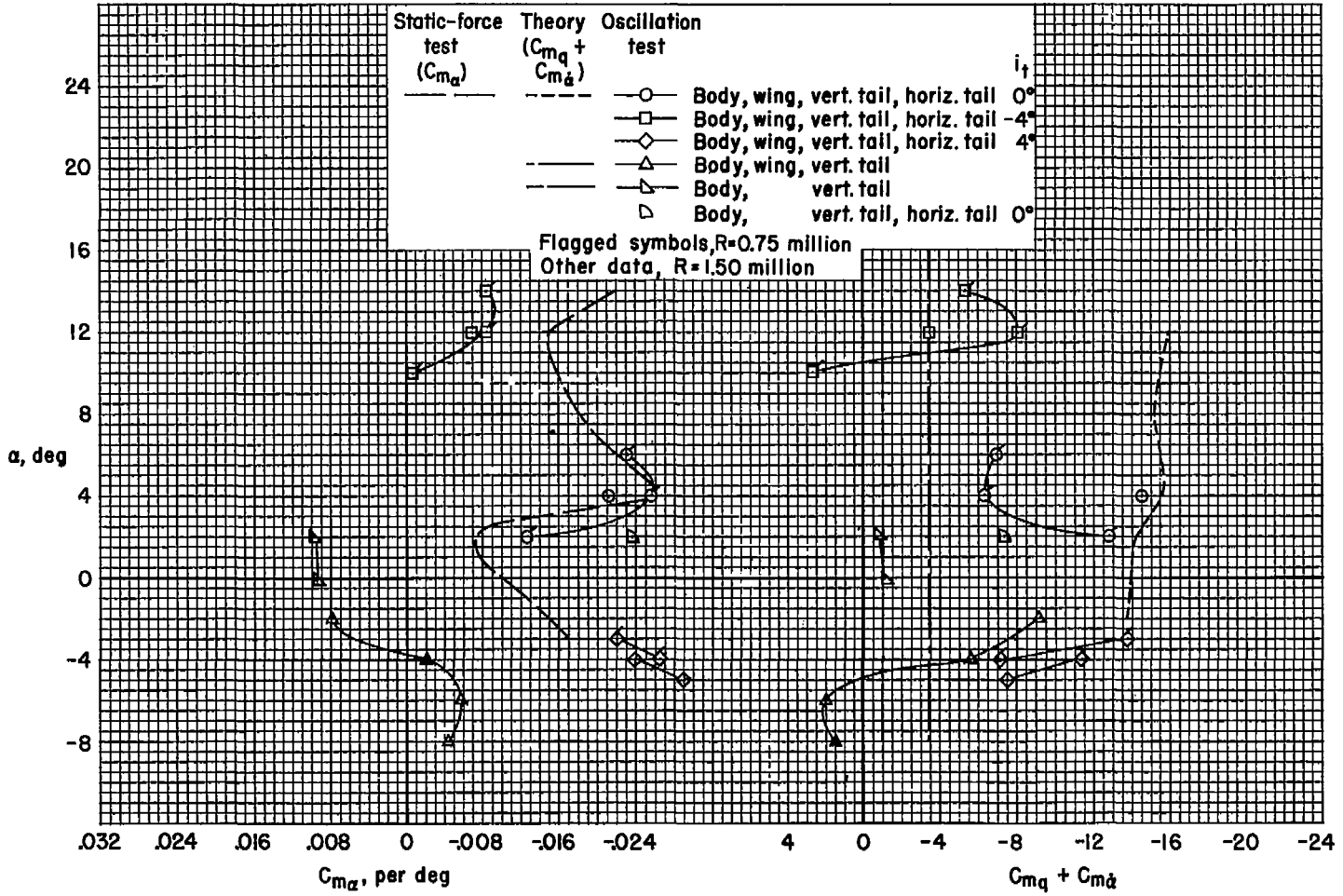
Figure 11.- Continued.



(f) $M = 0.92$

Figure 11.- Continued.

CONFIDENTIAL



(g) $M = 0.94$

Figure 11.- Concluded.

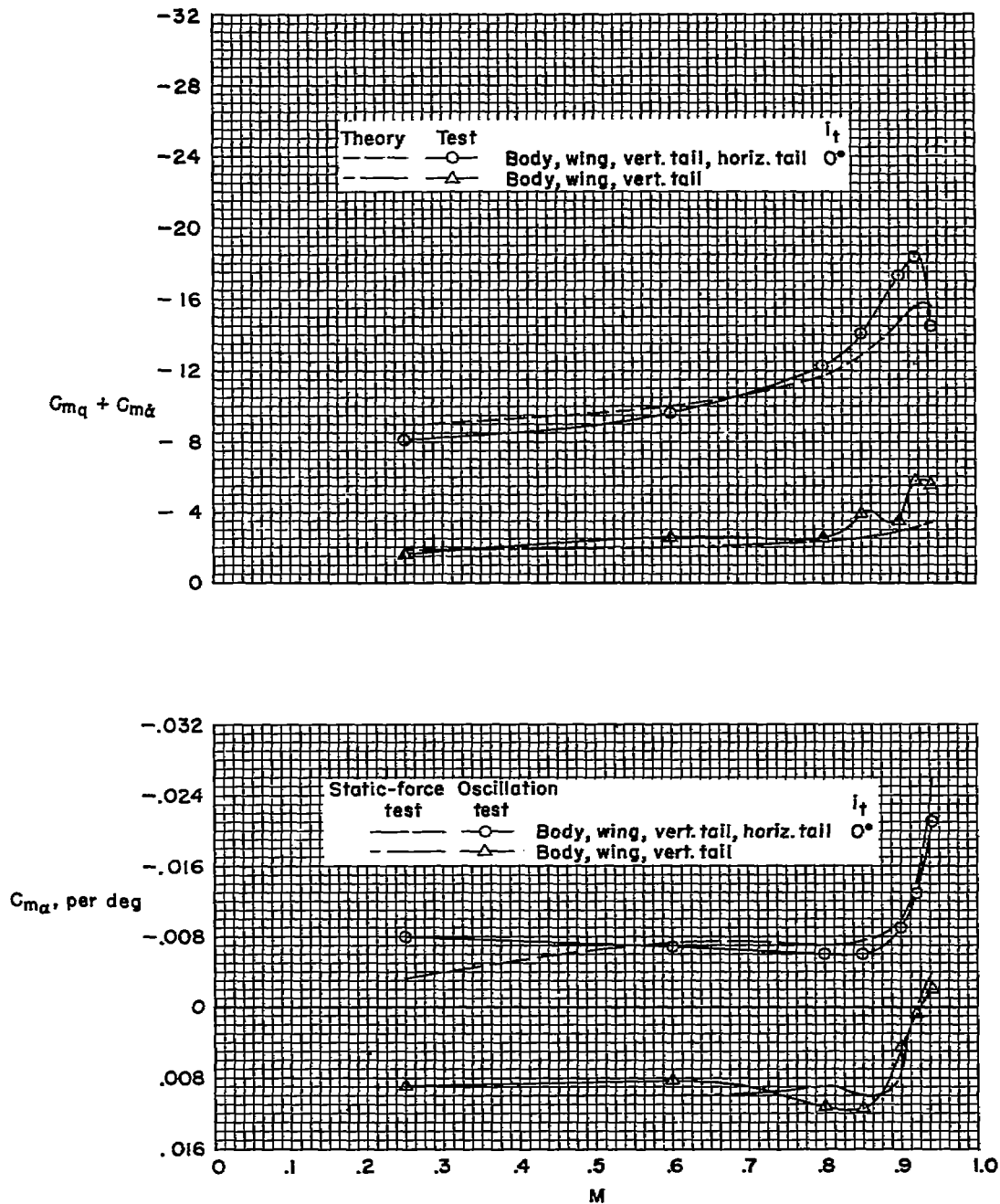


Figure 12.- The variation with Mach number of the longitudinal stability derivatives, C_{m_α} and $C_{m_q} + C_{m_{\dot{\alpha}}}$; $R = 1.50$ million, wing dihedral = -10° , $\alpha = 4^\circ$ except for oscillation tests of body, wing, and vertical tail which were performed at $\alpha = -4^\circ$.

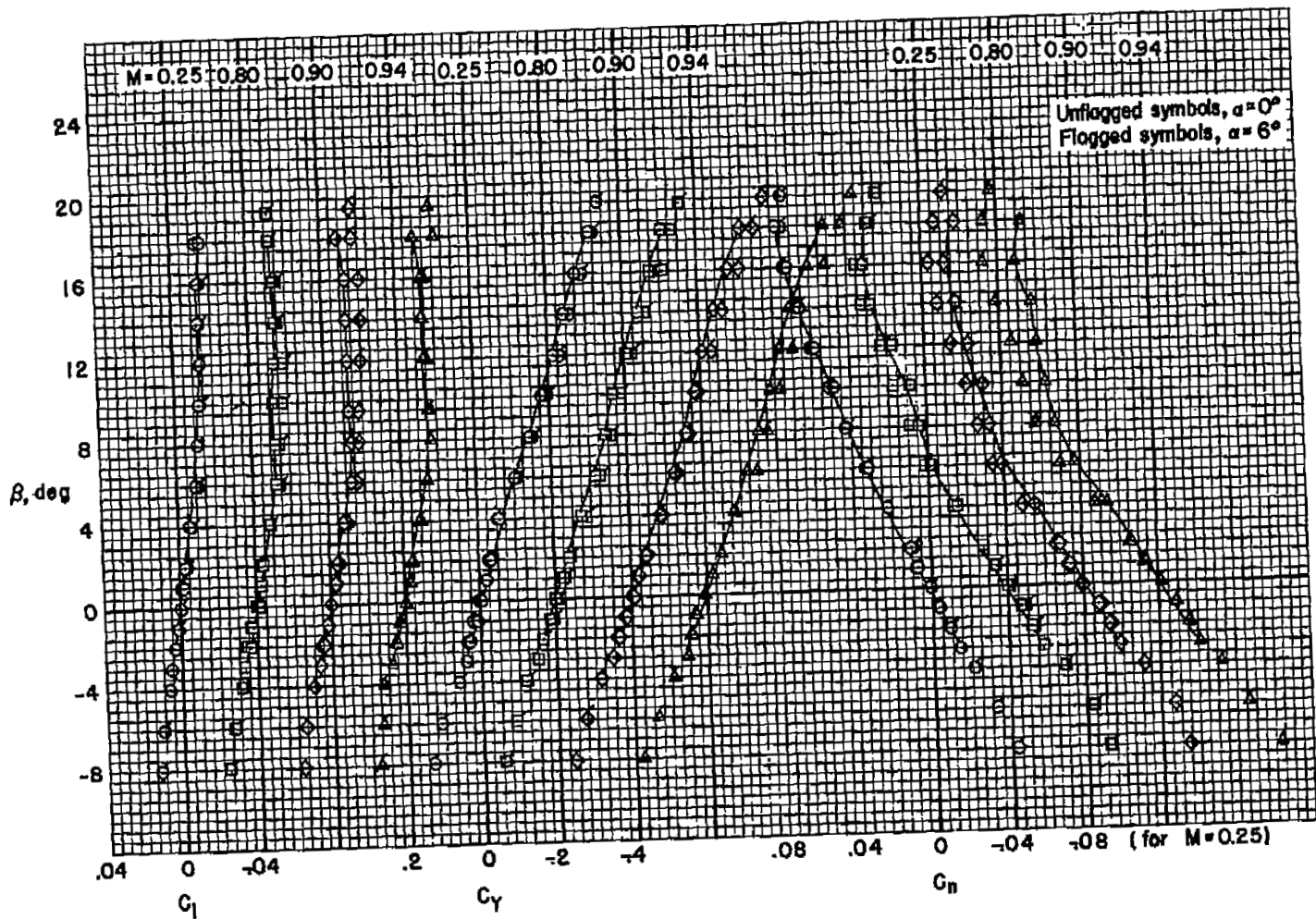
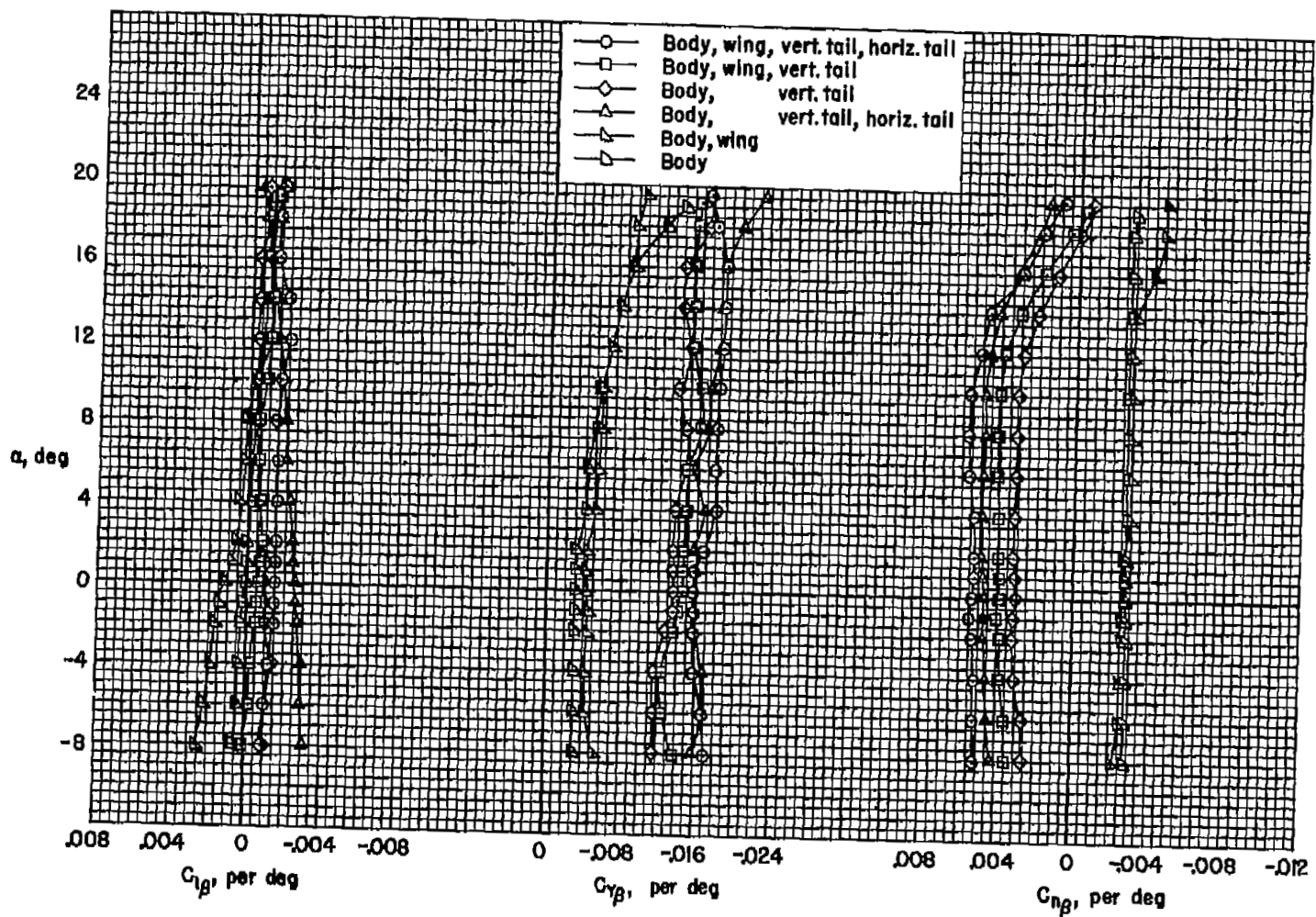


Figure 13.- The static lateral-directional characteristics of the complete model; $R = 1.50$ million, wing dihedral = -10° .

CONFIDENTIAL



(a) M = 0.25

Figure 14.- The sideslip derivatives from static-force tests; R = 1.50 million, wing dihedral = -10°.

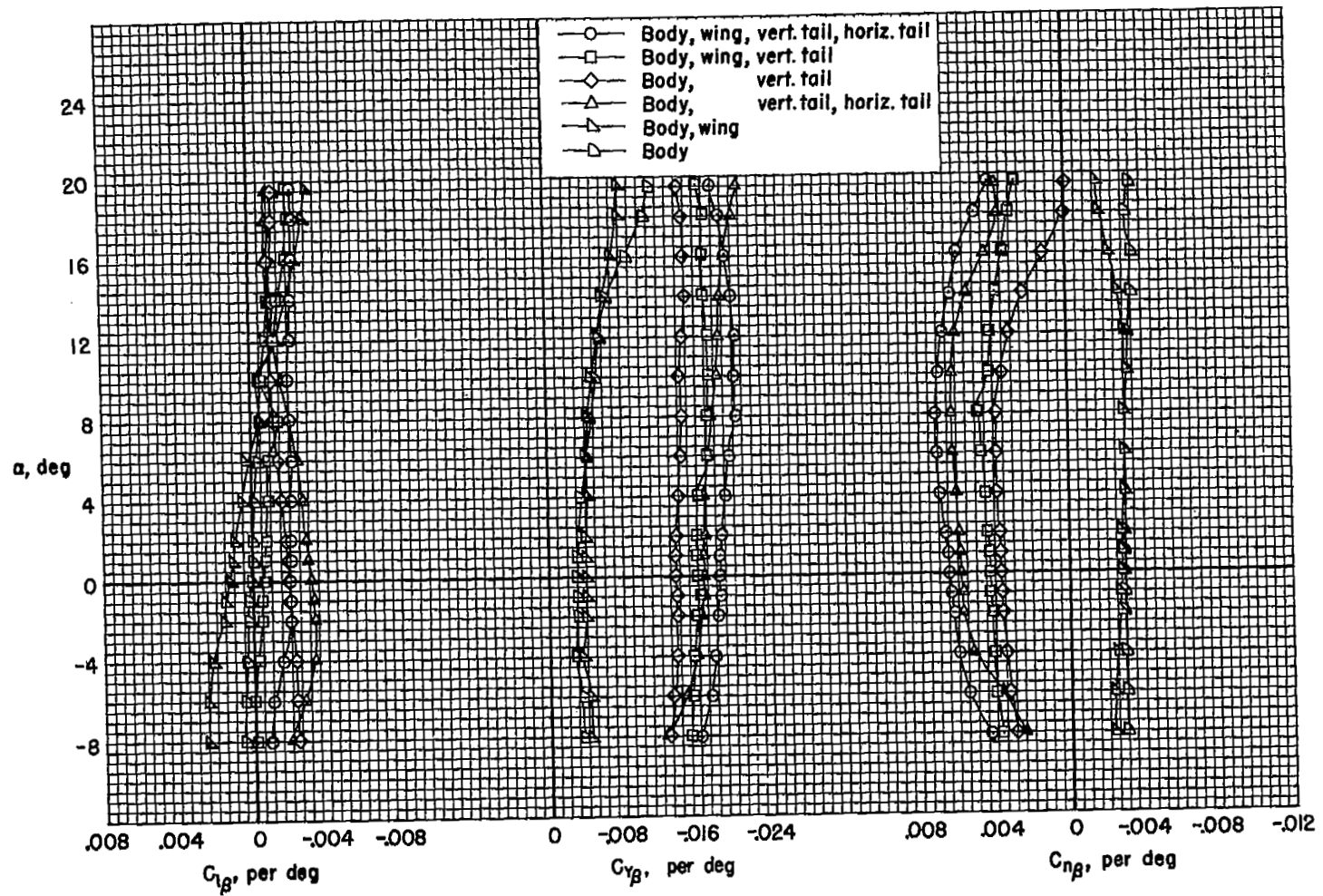
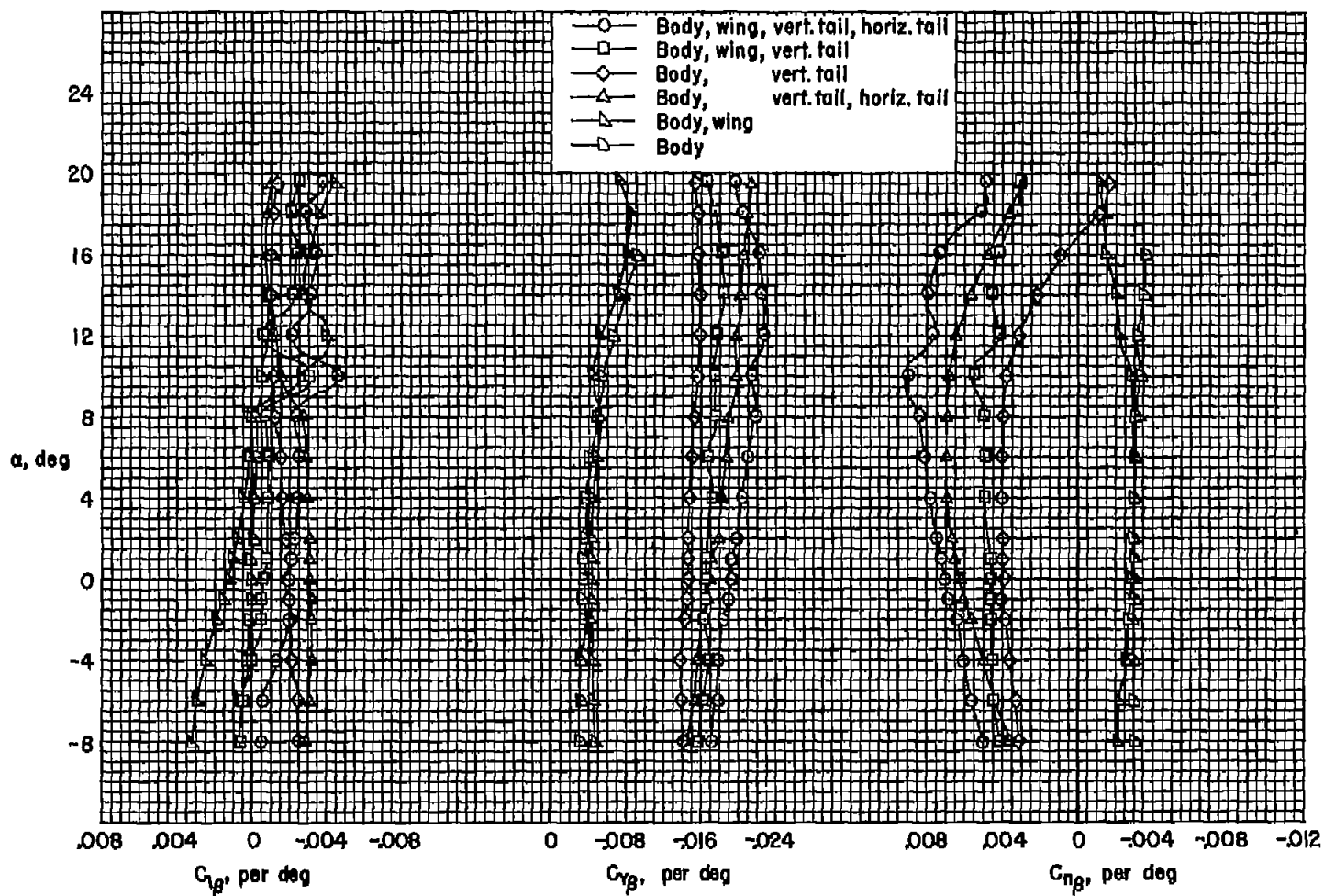
(b) $M = 0.80$

Figure 14.- Continued.



(c) $M = 0.90$

Figure 14.- Continued.

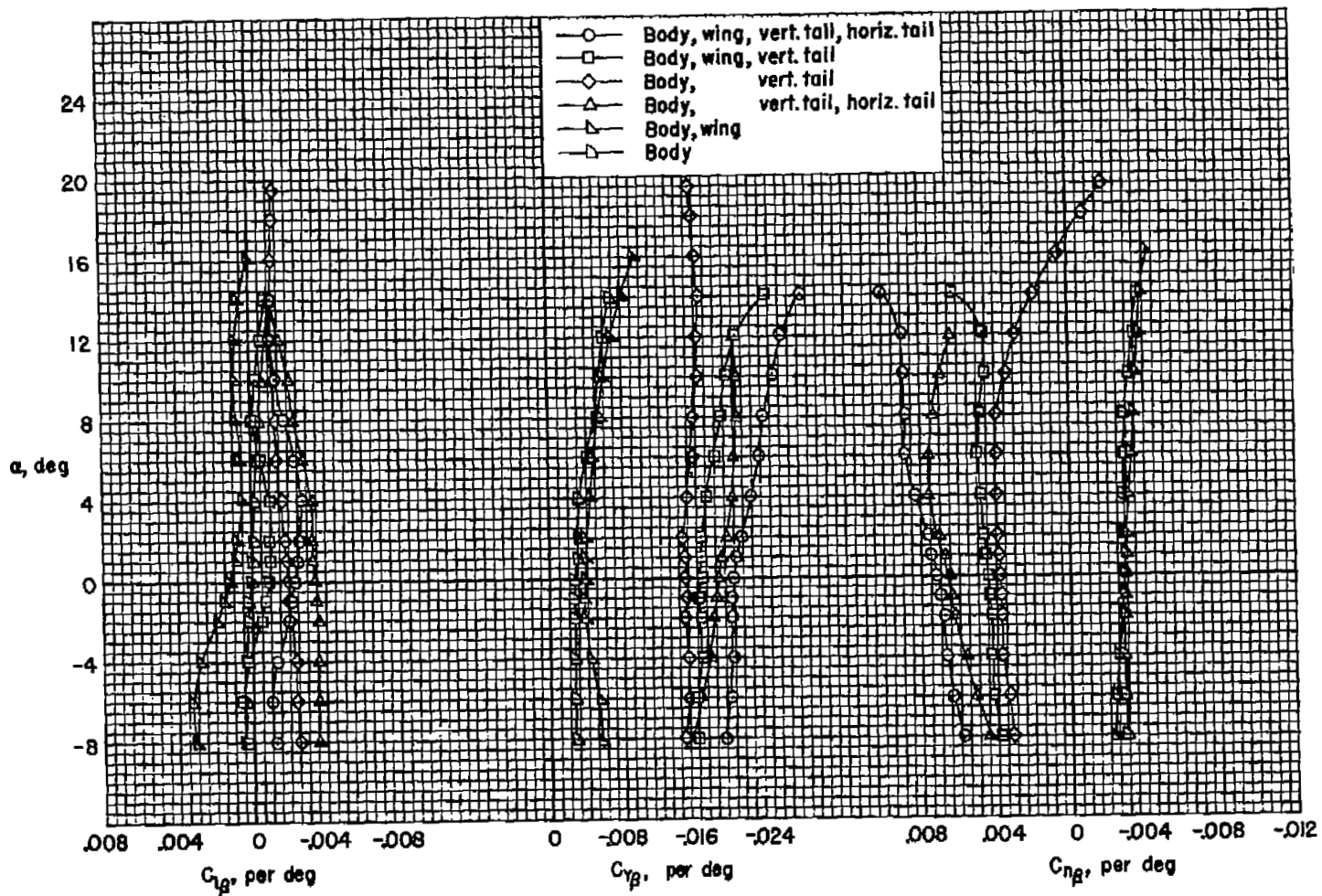
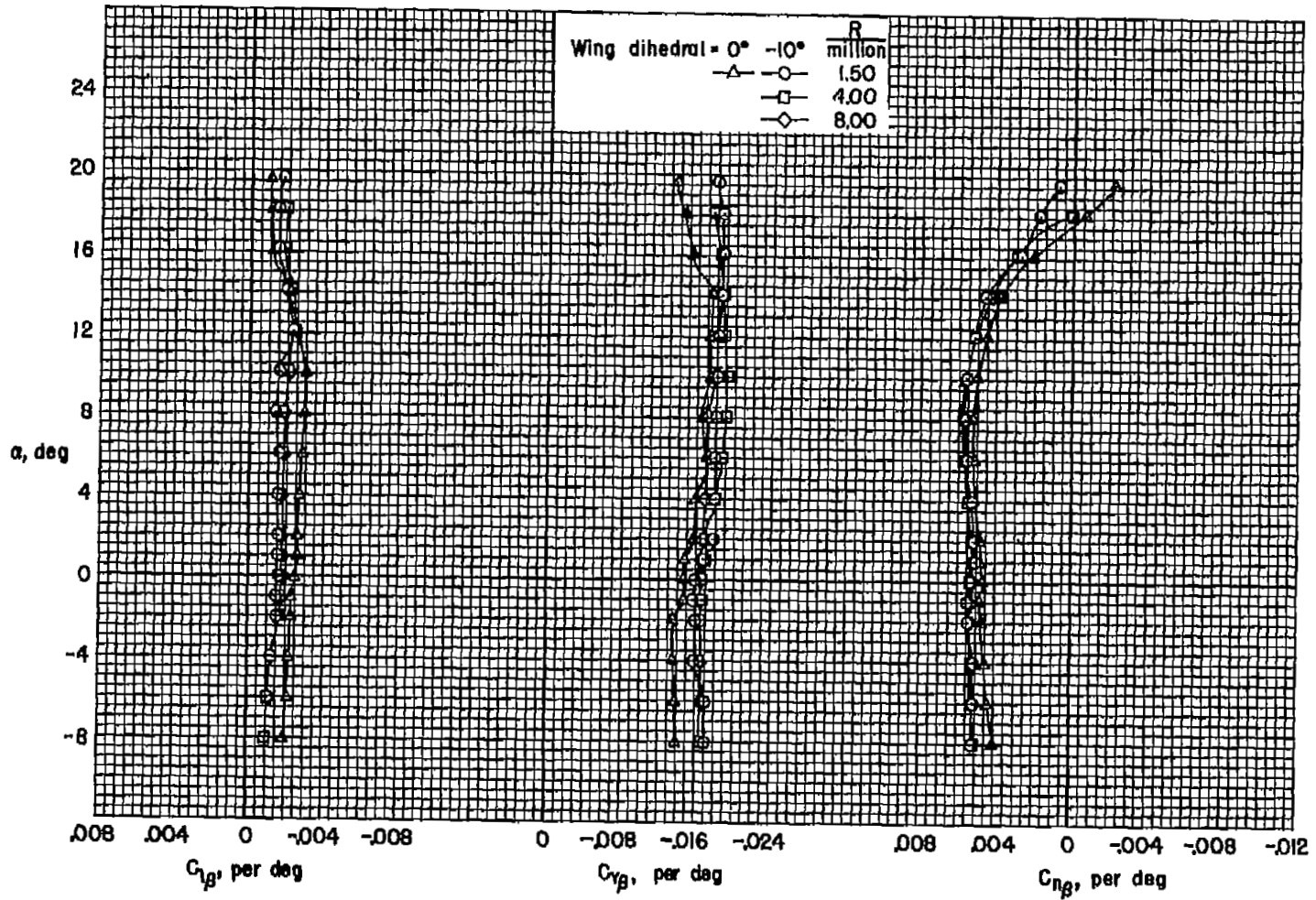


Figure 14.- Concluded.

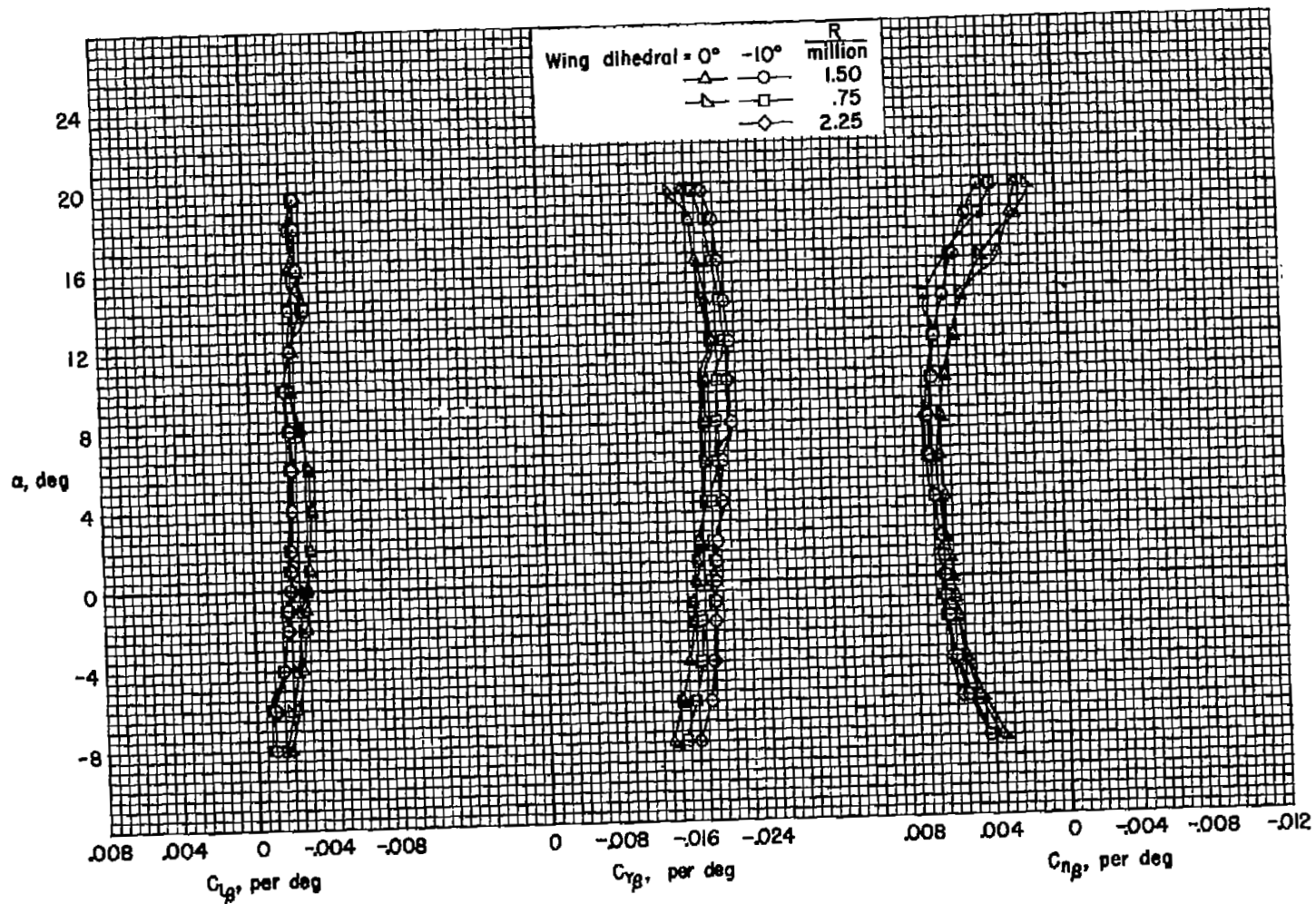
CONFIDENTIAL



(a) $M = 0.25$

Figure 15.- The effect of Reynolds number and wing dihedral on the sideslip derivatives from the static-force tests of the complete model.

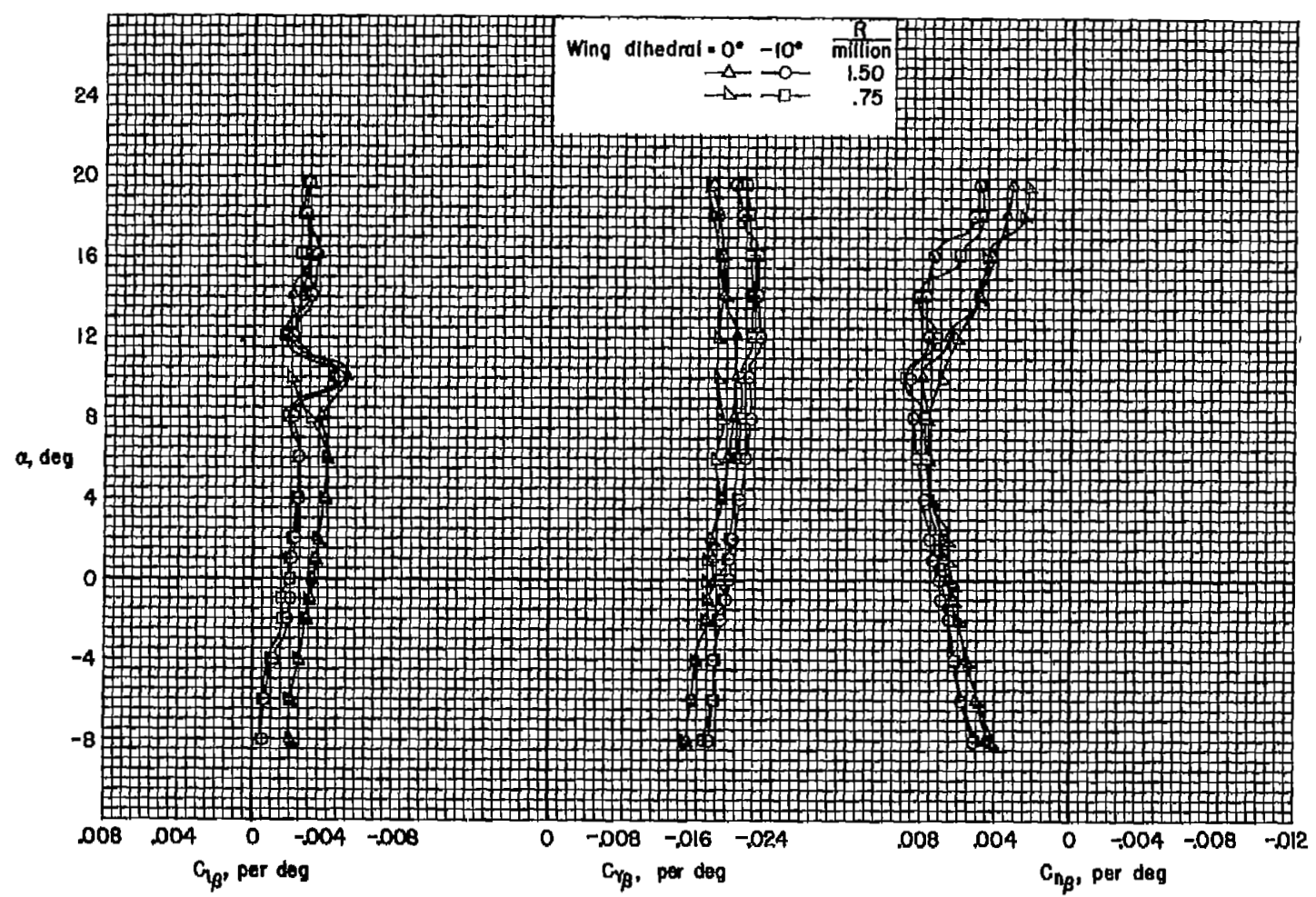
CONFIDENTIAL



(b) $M = 0.80$

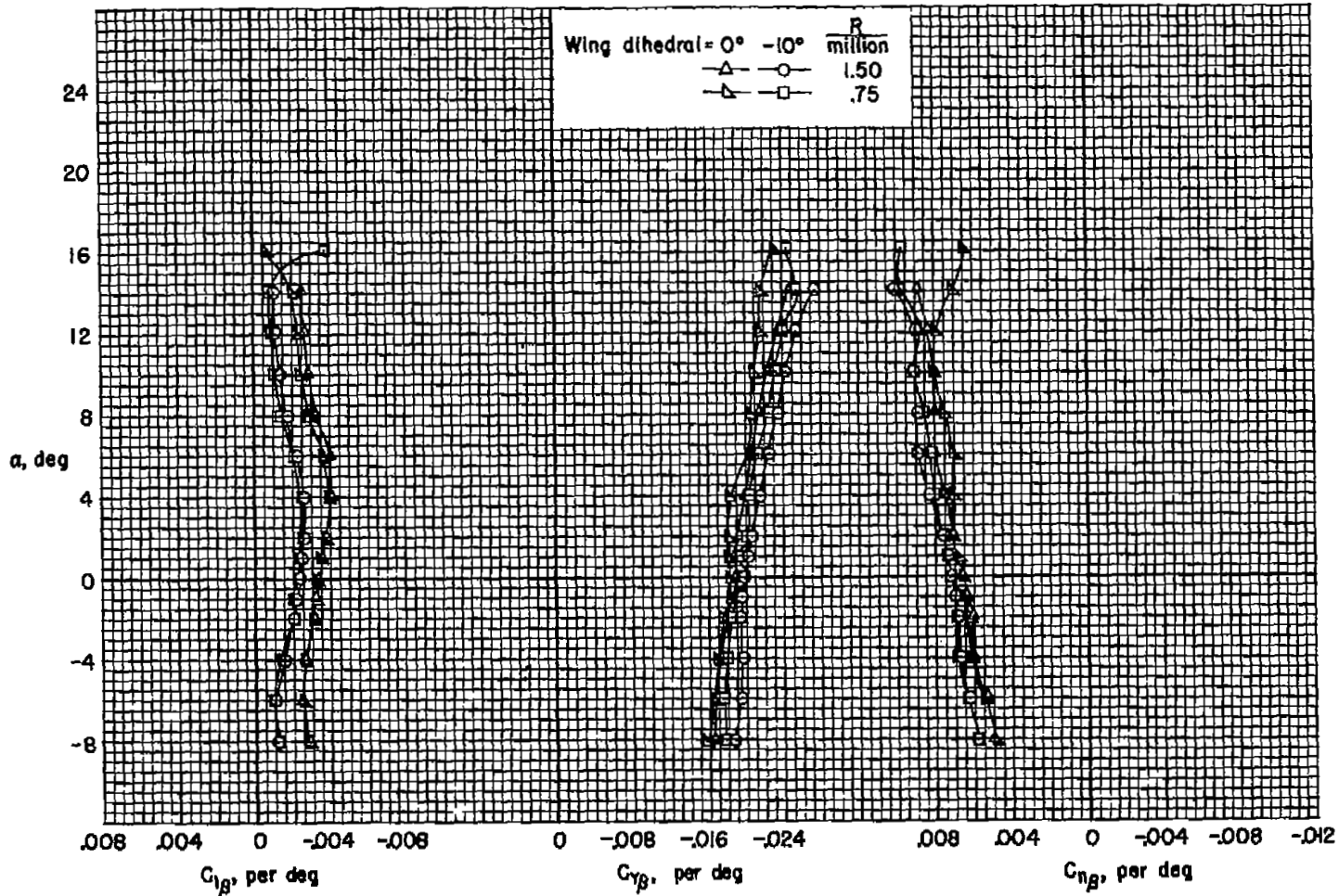
Figure 15.- Continued.

CONFIDENTIAL



(c) $M = 0.90$

Figure 15.- Continued.

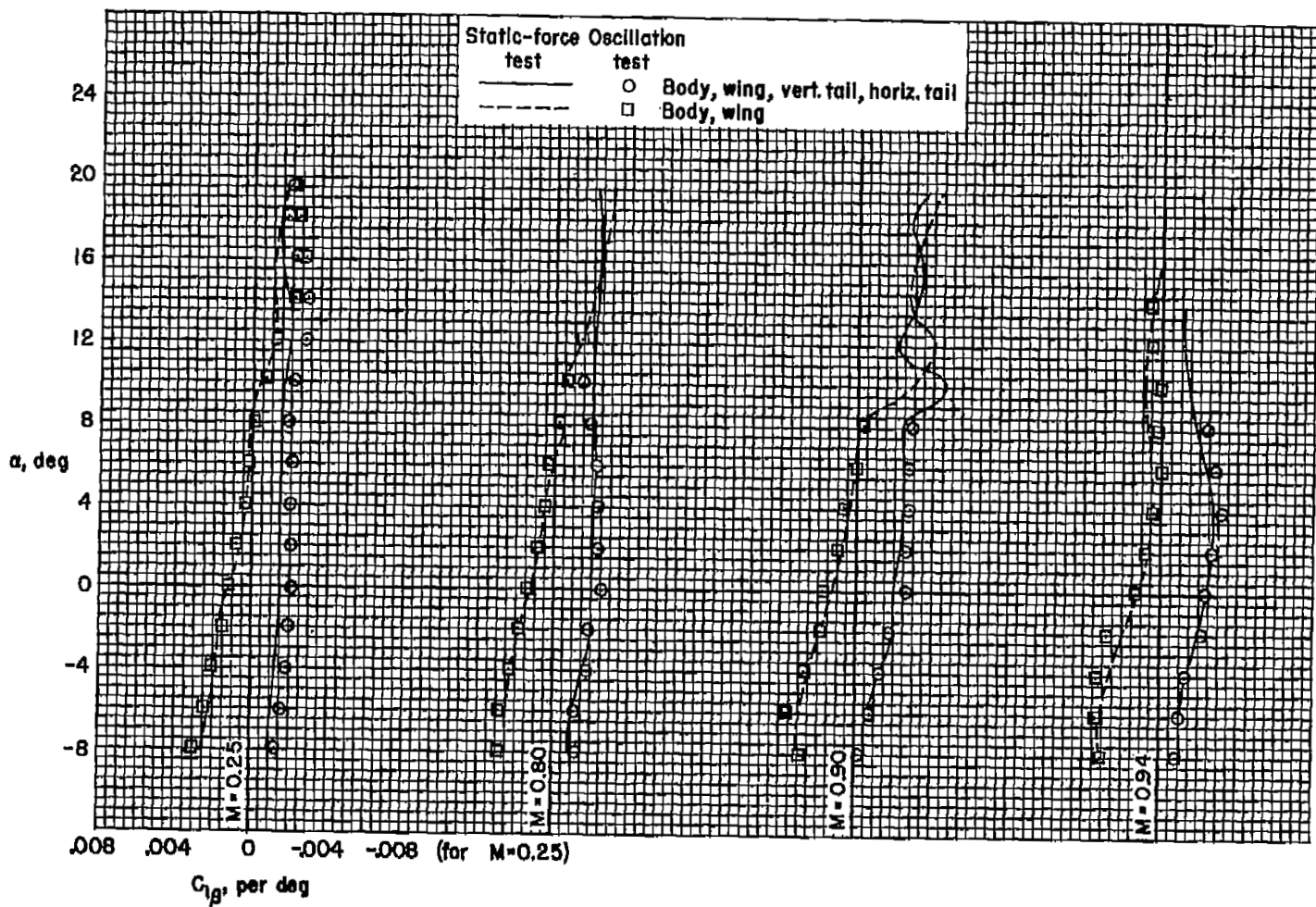


(a) $M = 0.94$

Figure 15.- Concluded.

CONFIDENTIAL

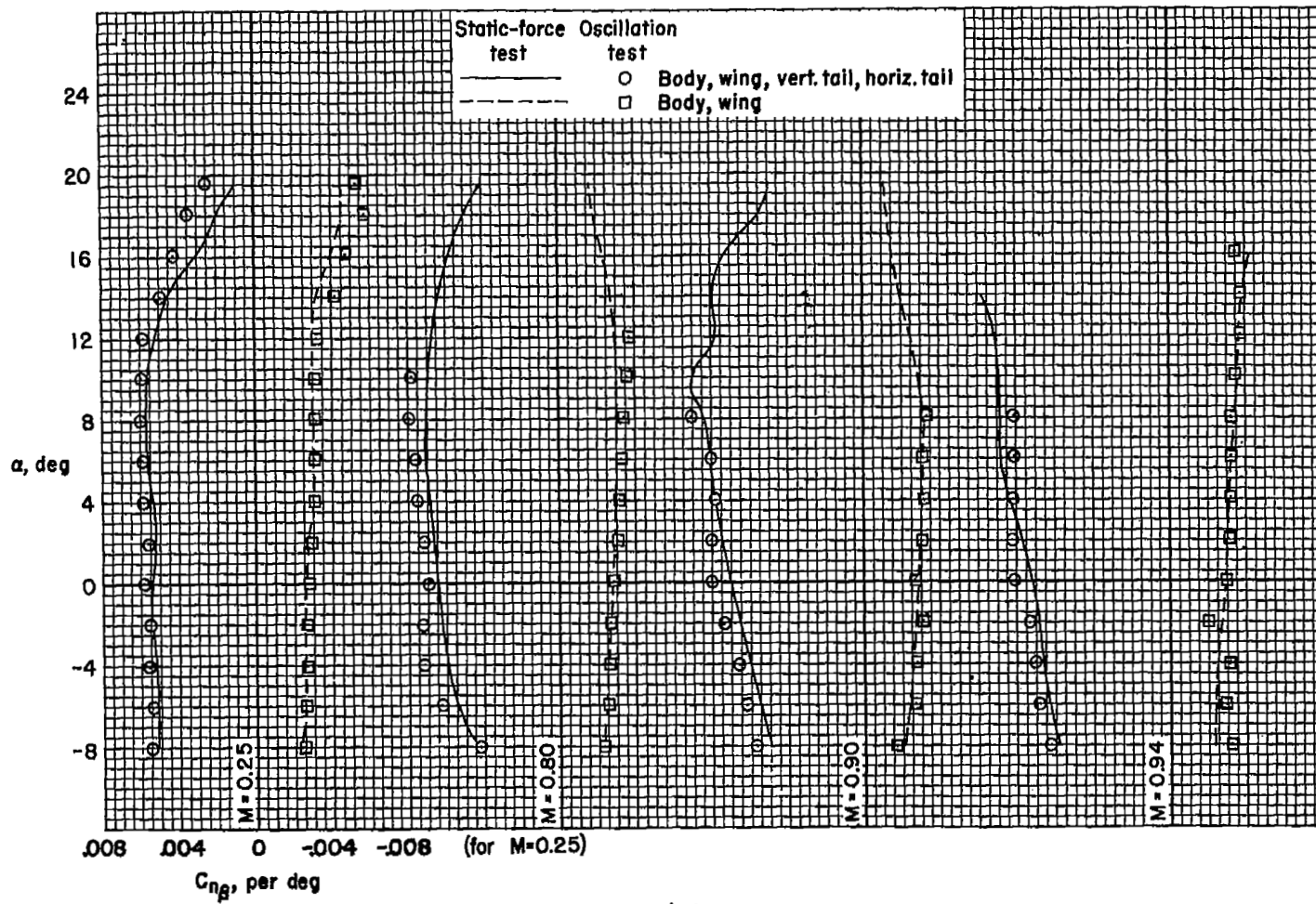
CONFIDENTIAL



(a) C_{l_β}

Figure 16.- A comparison of the sideslip derivatives from static-force tests and oscillation tests; $R = 1.50$ million, wing dihedral = -10° .

CONFIDENTIAL



(b) $C_{n\beta}$

Figure 16.- Concluded.

CONFIDENTIAL

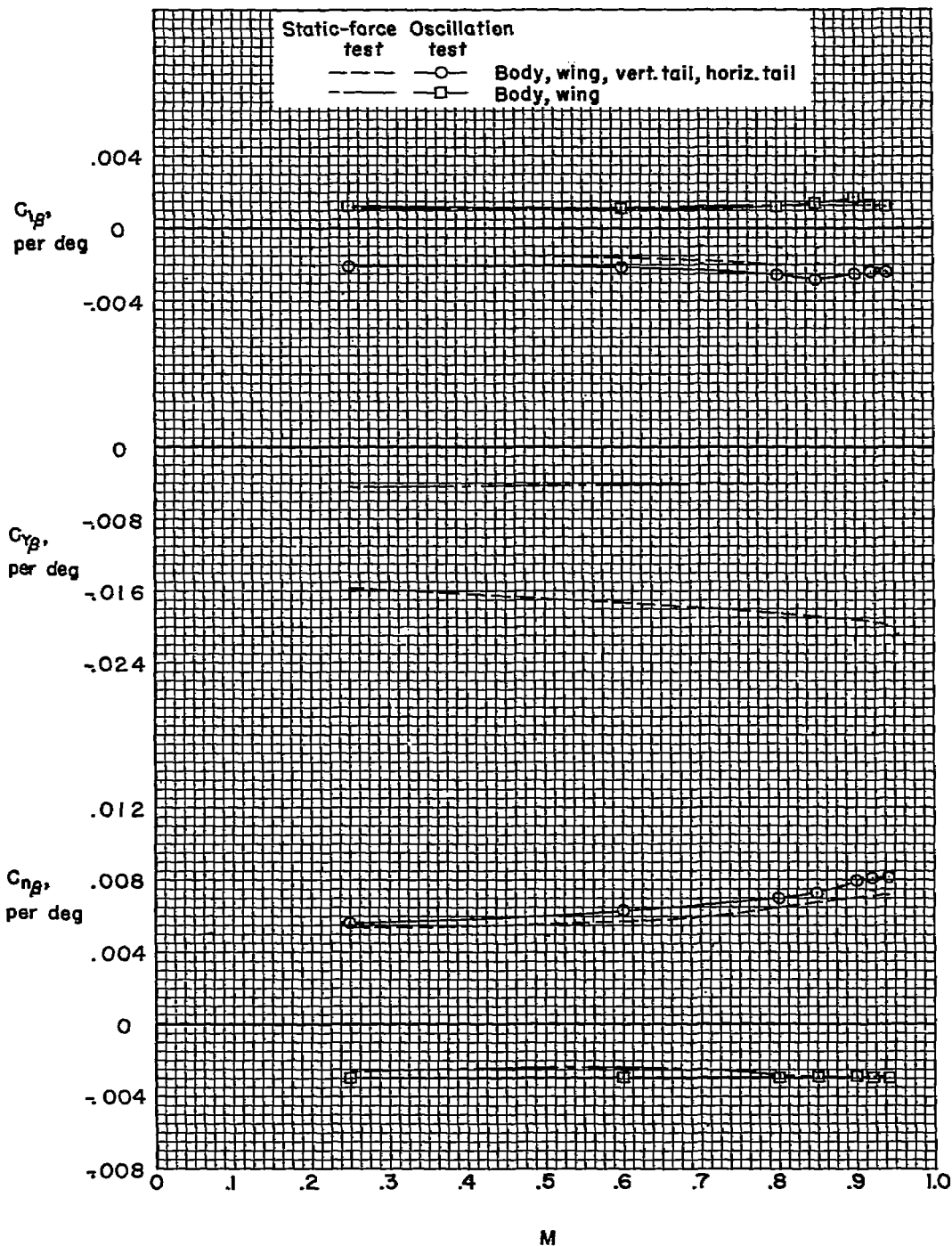
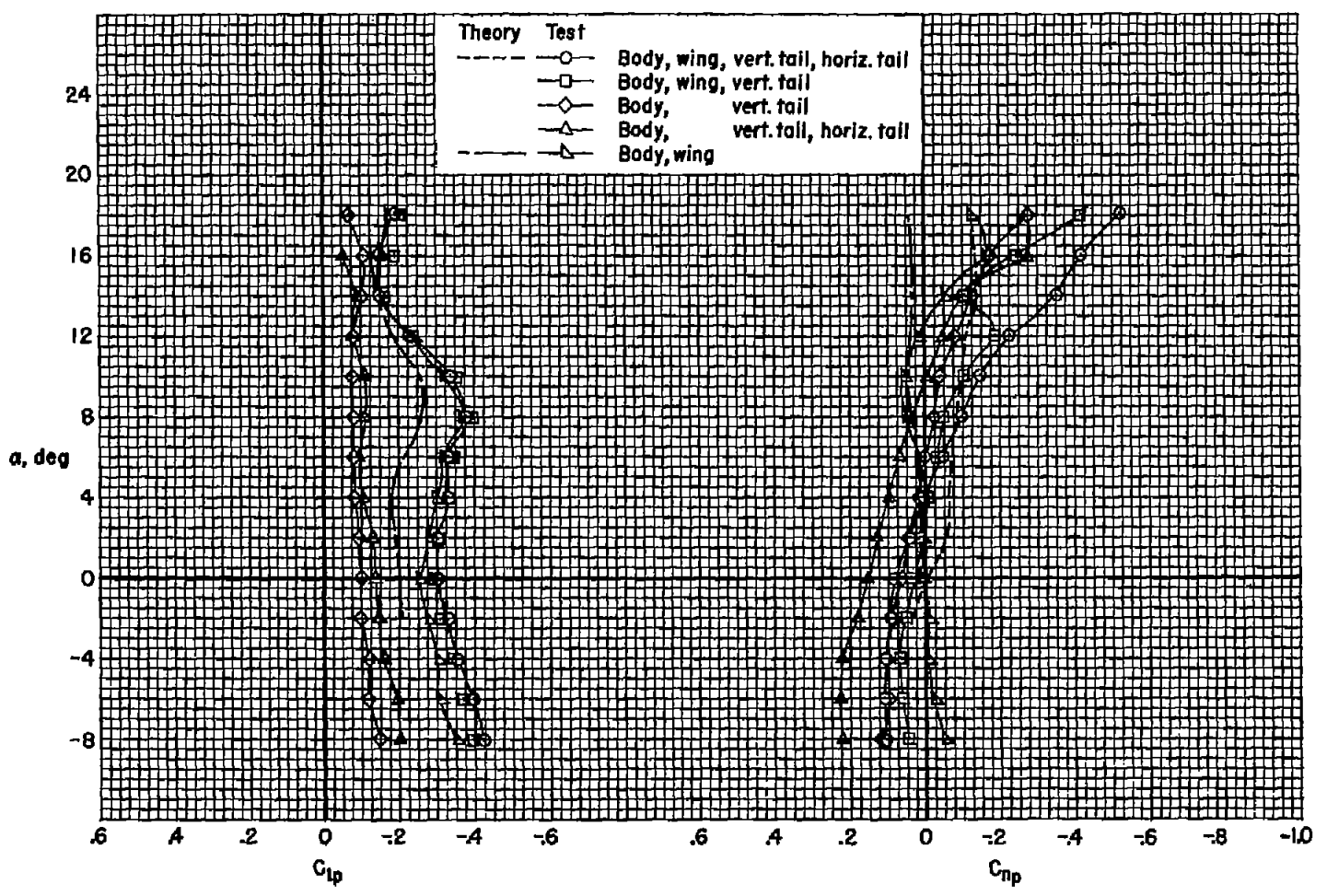


Figure 17.- The variation with Mach number of the sideslip derivatives; $R = 1.50$ million, wing dihedral = -10° , $\alpha = 0^\circ$.

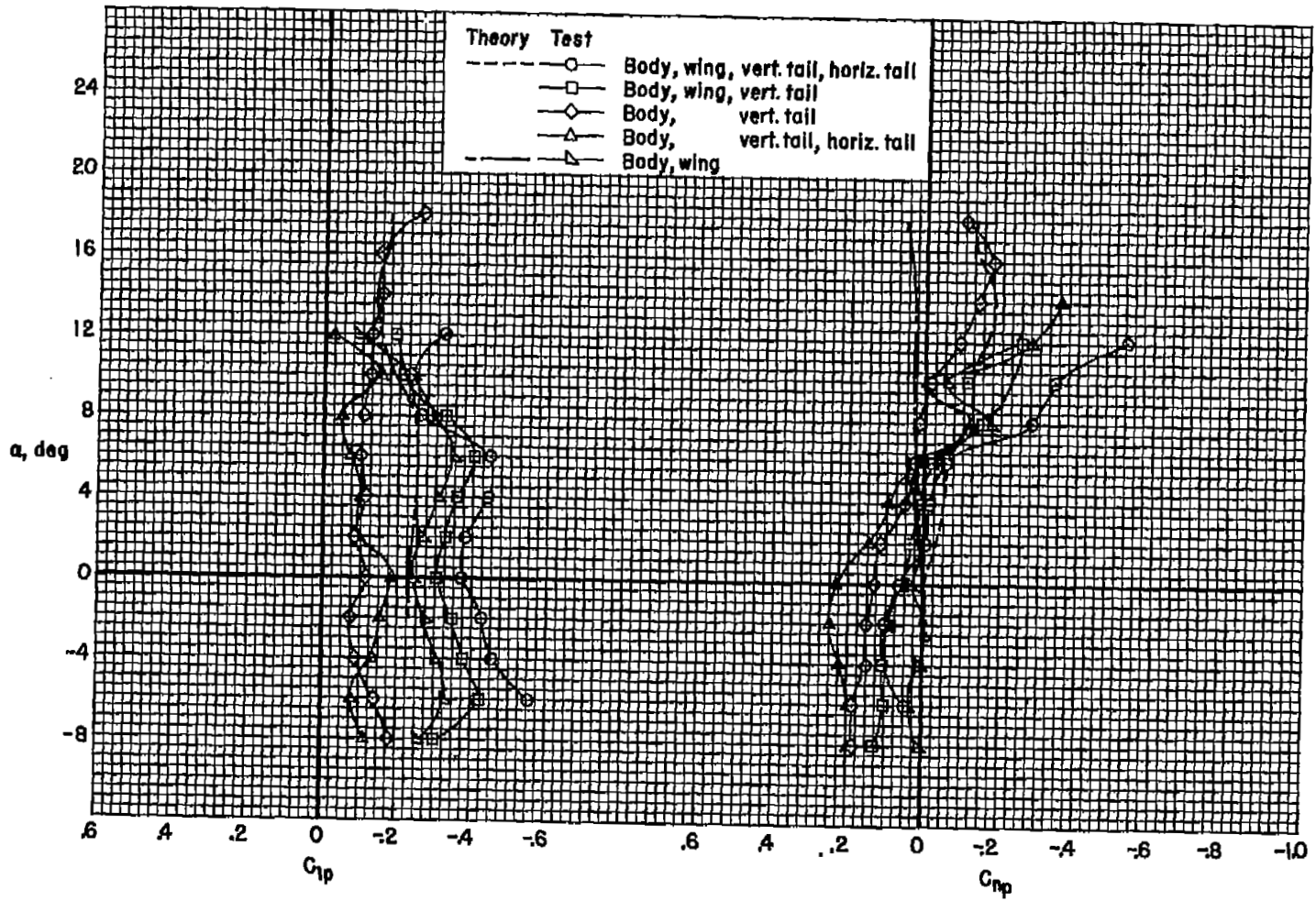


(a) $M = 0.25$

Figure 18.- The variation of damping in roll and yawing moment due to rolling velocity with angle of attack; $R = 1.50$ million, wing dihedral = -10° .

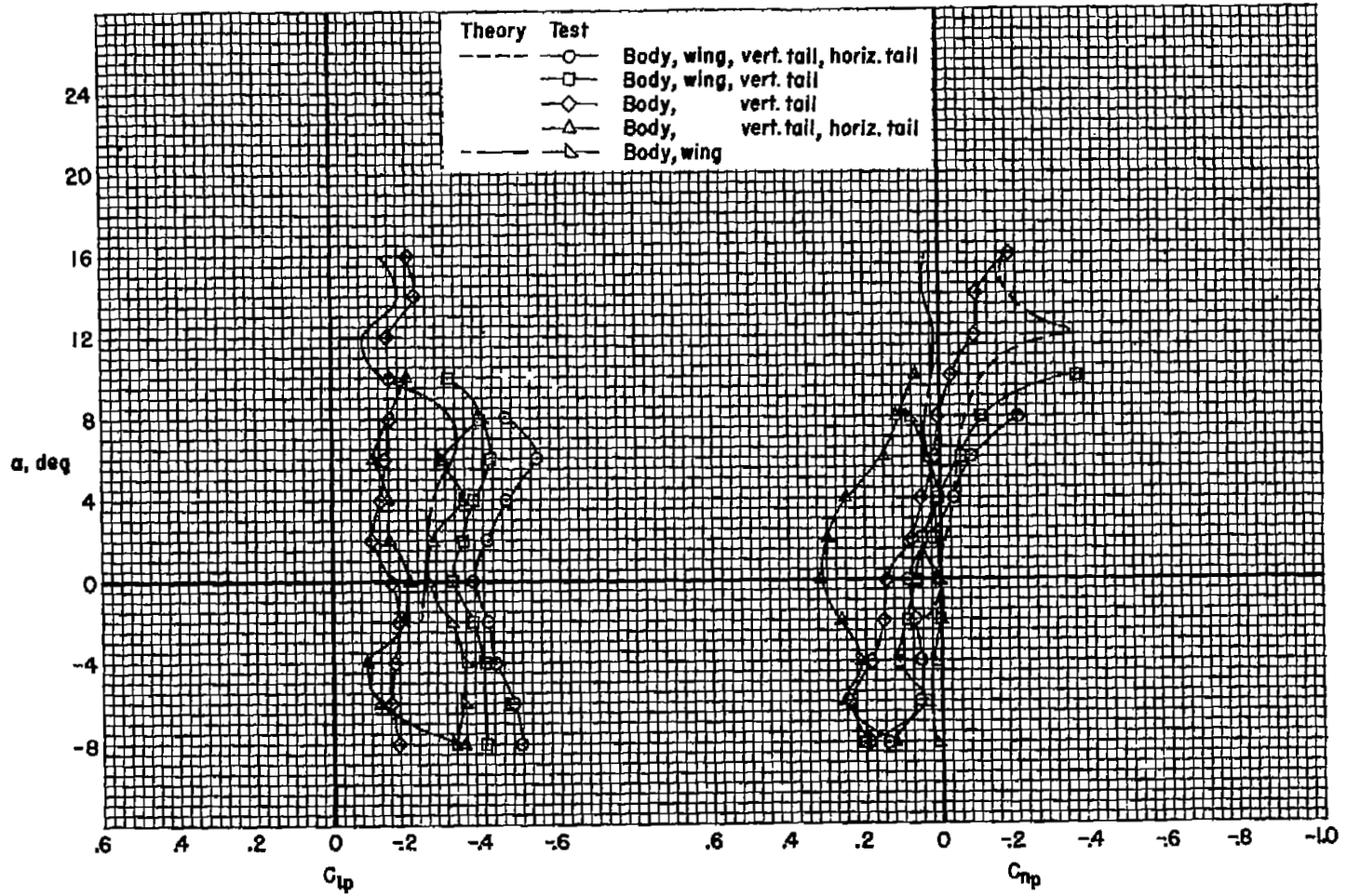
CONFIDENTIAL

CONFIDENTIAL



(b) $M = 0.80$

Figure 18.- Continued.



(c) $M = 0.90$

Figure 18.- Continued.

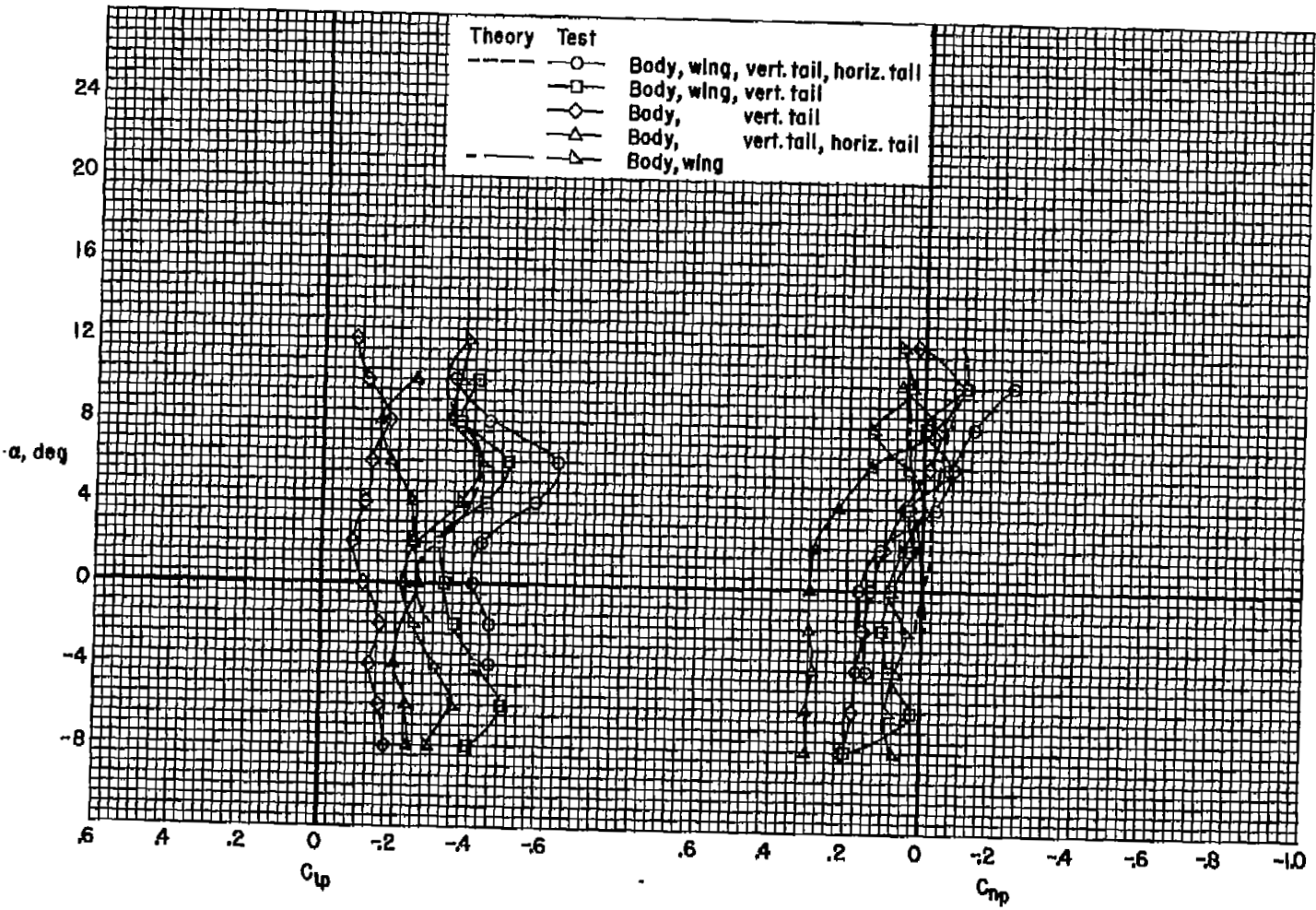
(d) $M = 0.94$

Figure 18.- Concluded.

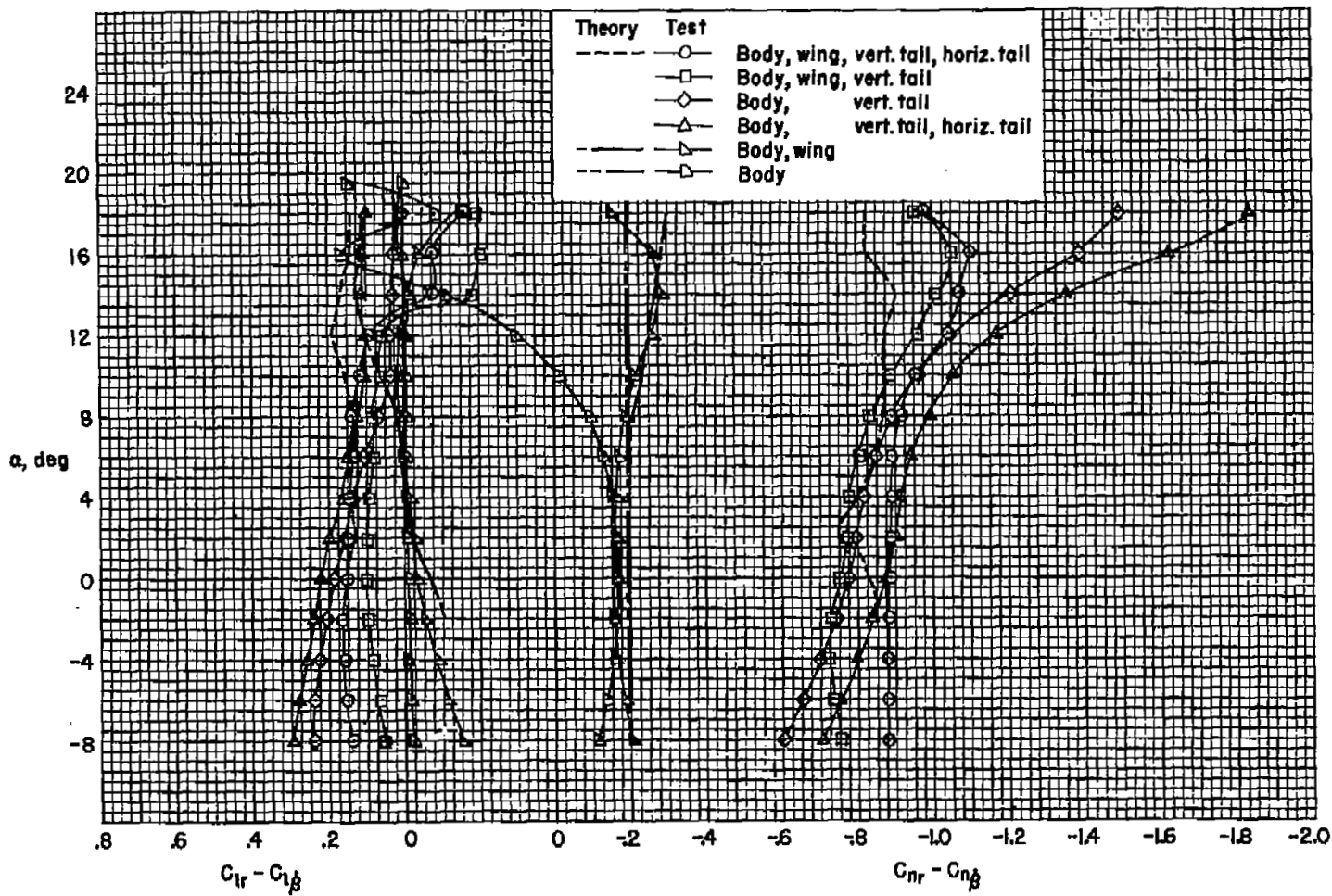
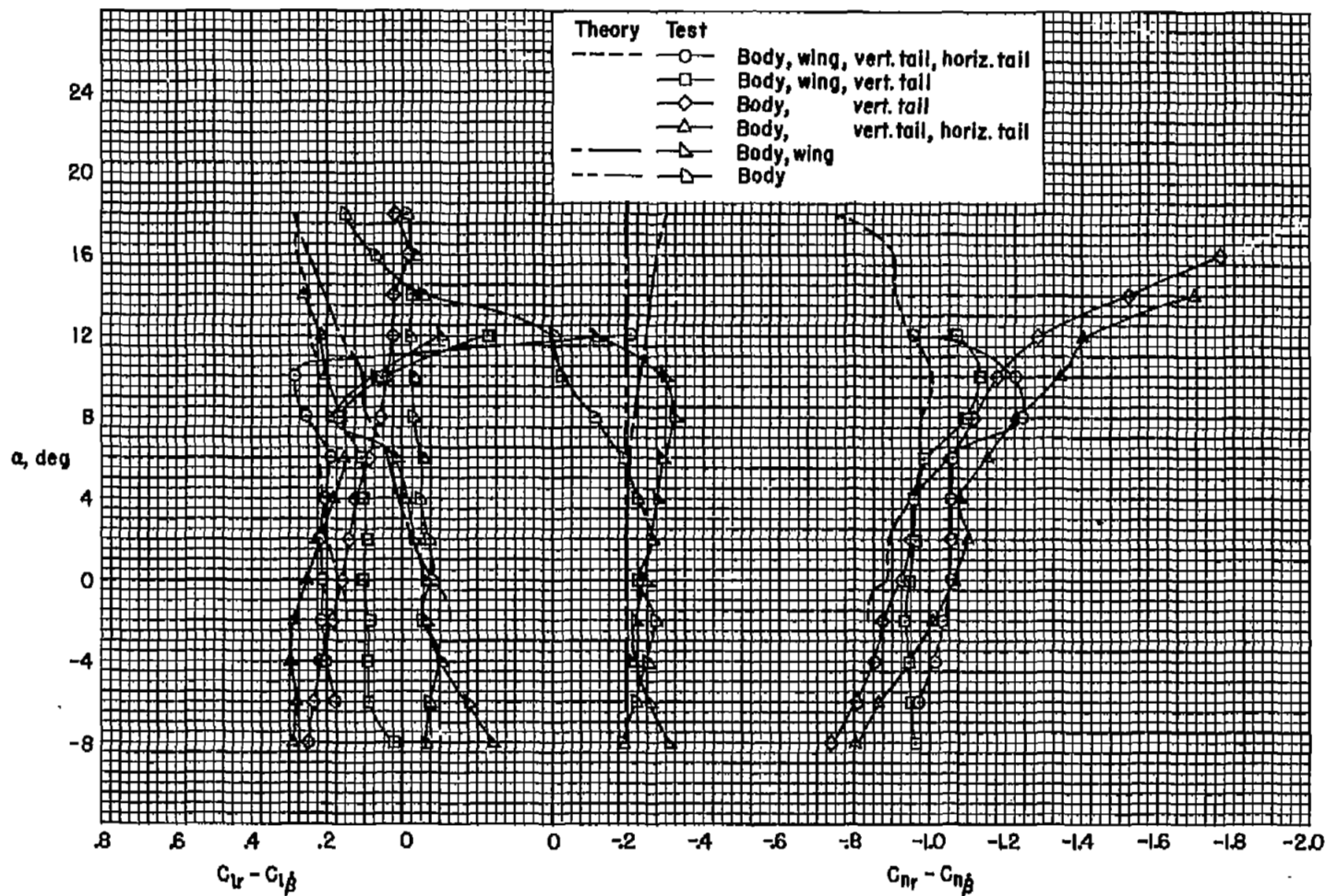
(a) $M = 0.25$

Figure 19.- The variation of rolling moment due to yawing velocity and damping in yaw with angle of attack; $R = 1.50$ million, wing dihedral = -10° .



(b) $M = 0.80$

Figure 19.- Continued.

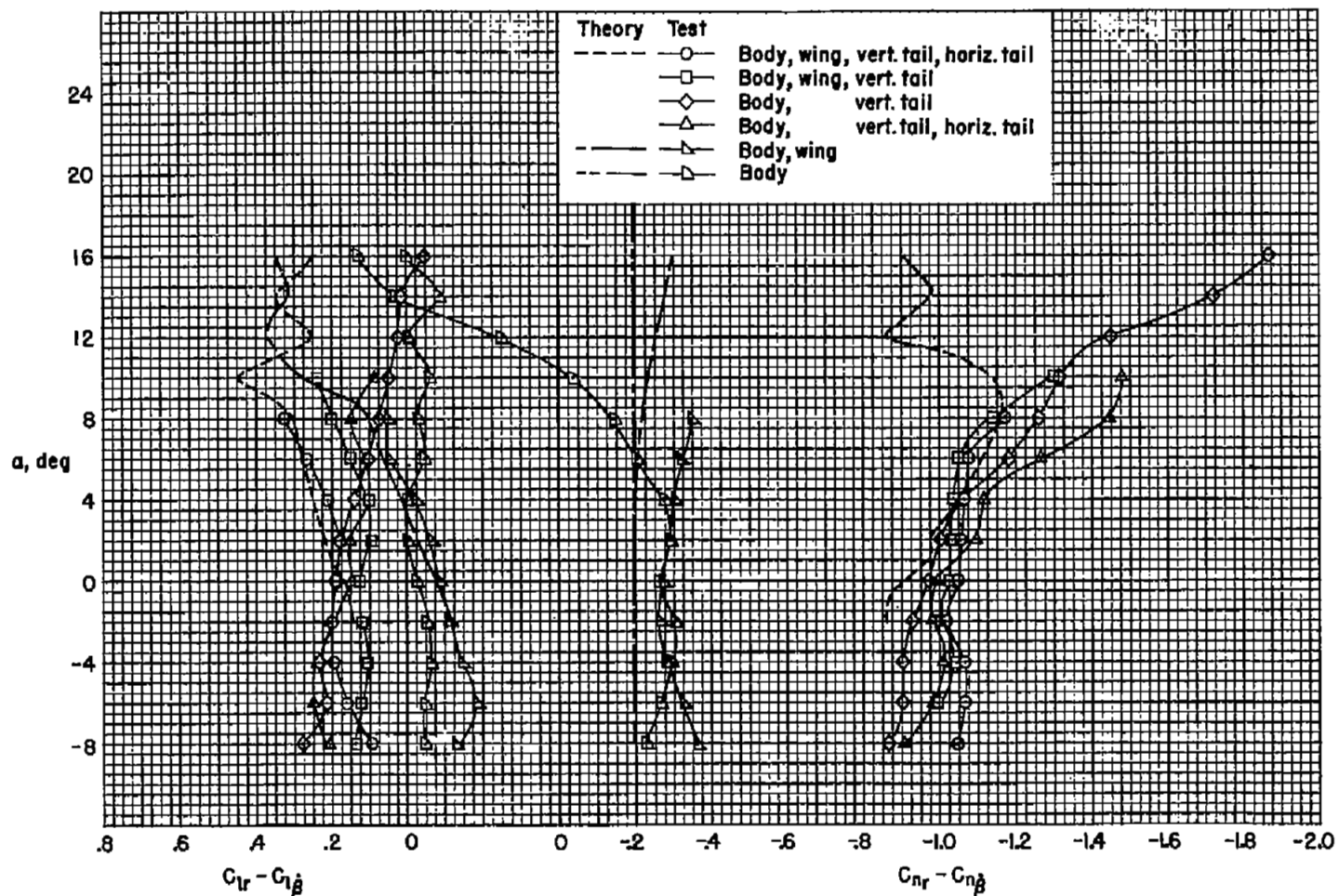
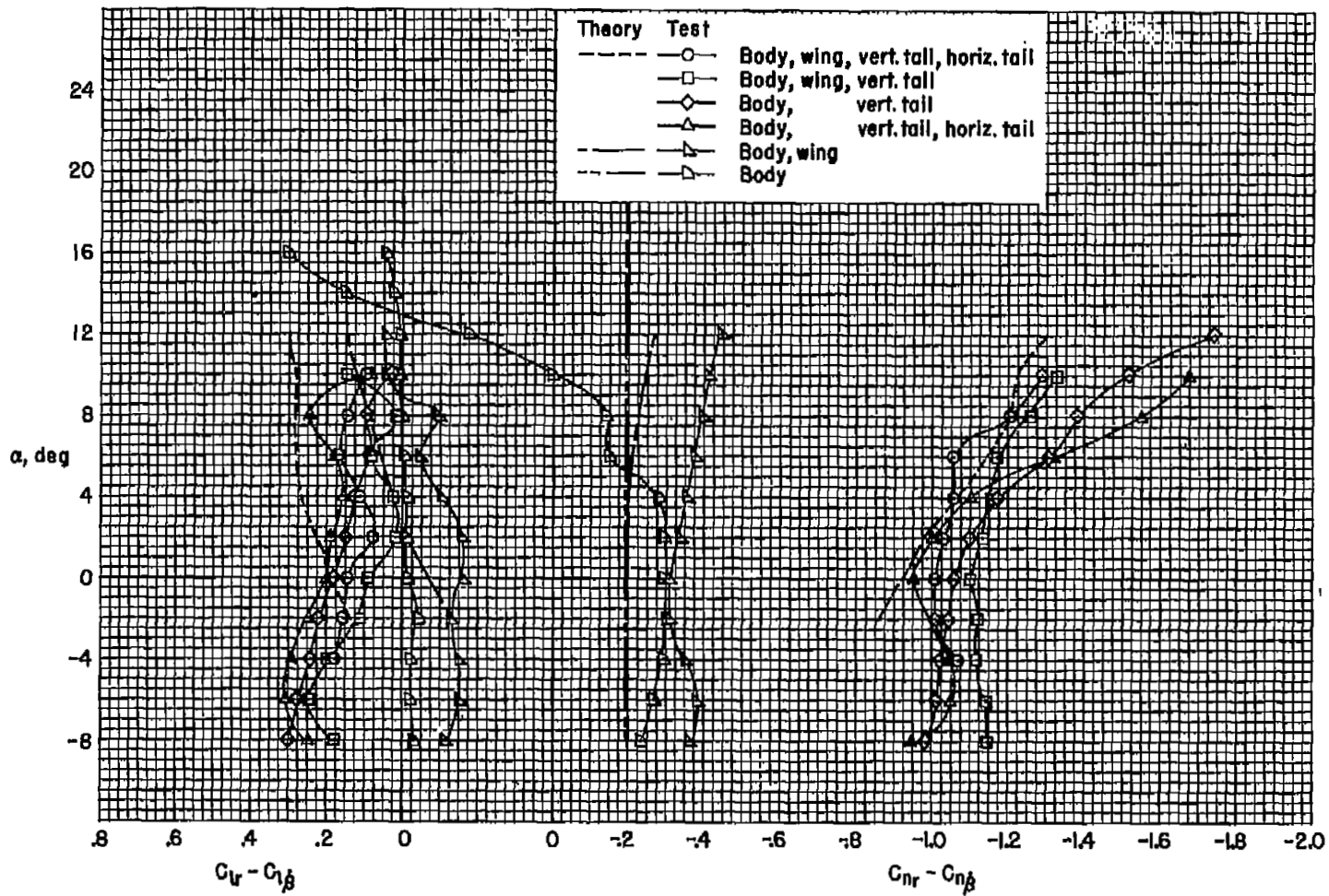
(c) $M = 0.90$

Figure 19.- Continued.



(a) $M = 0.94$

Figure 19.- Concluded.

CONFIDENTIAL

CONFIDENTIAL

CONFIDENTIAL

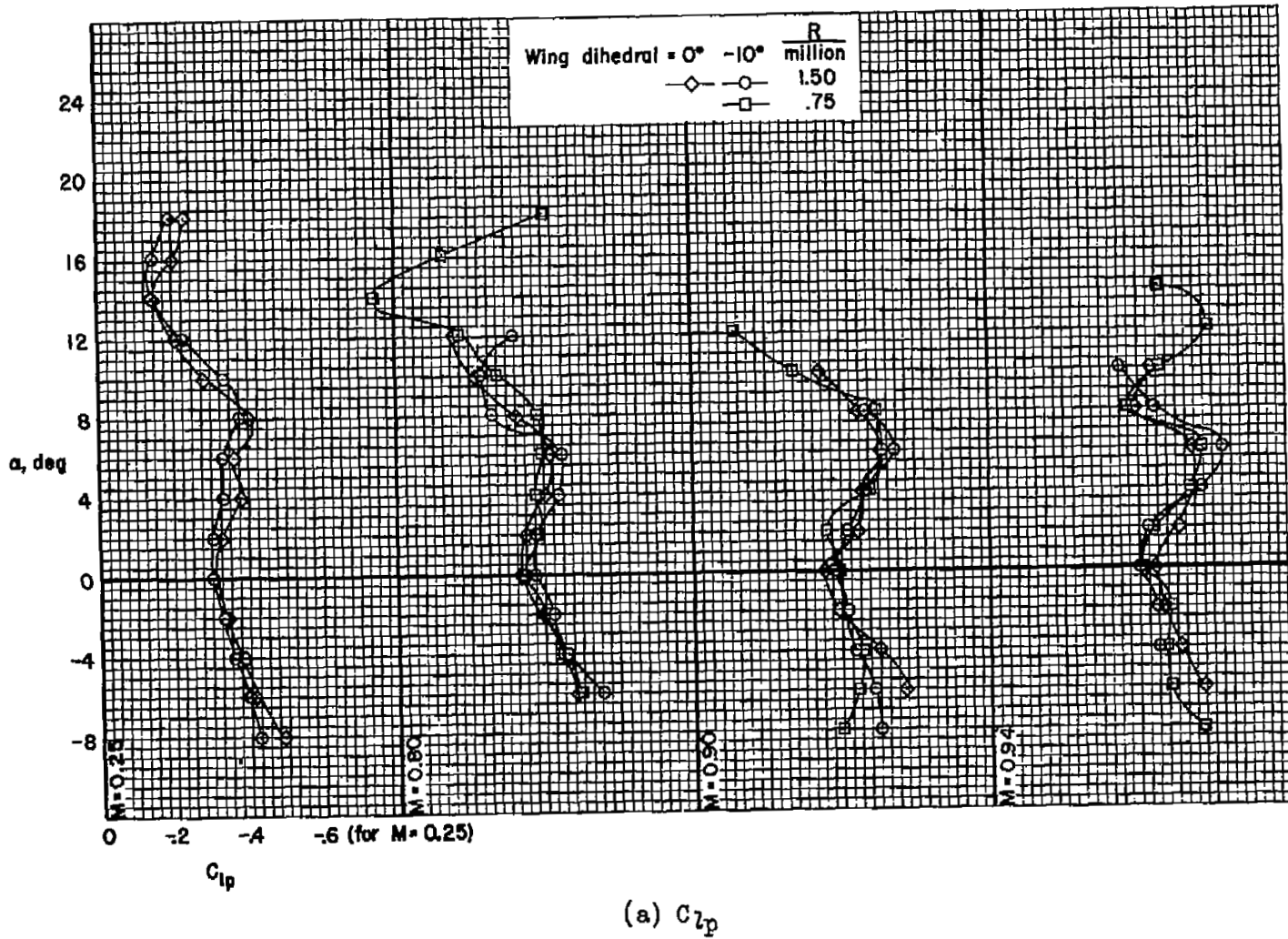
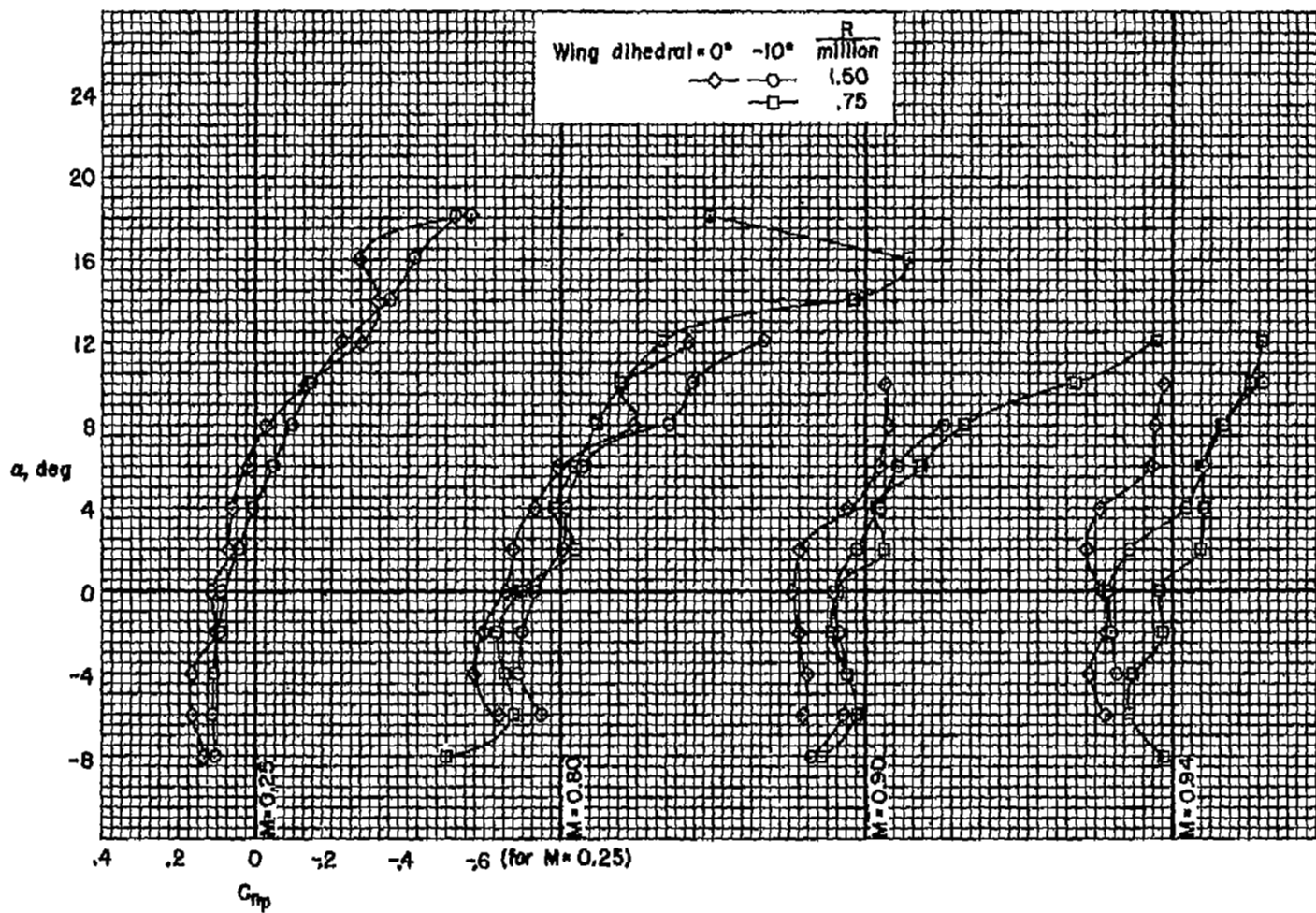
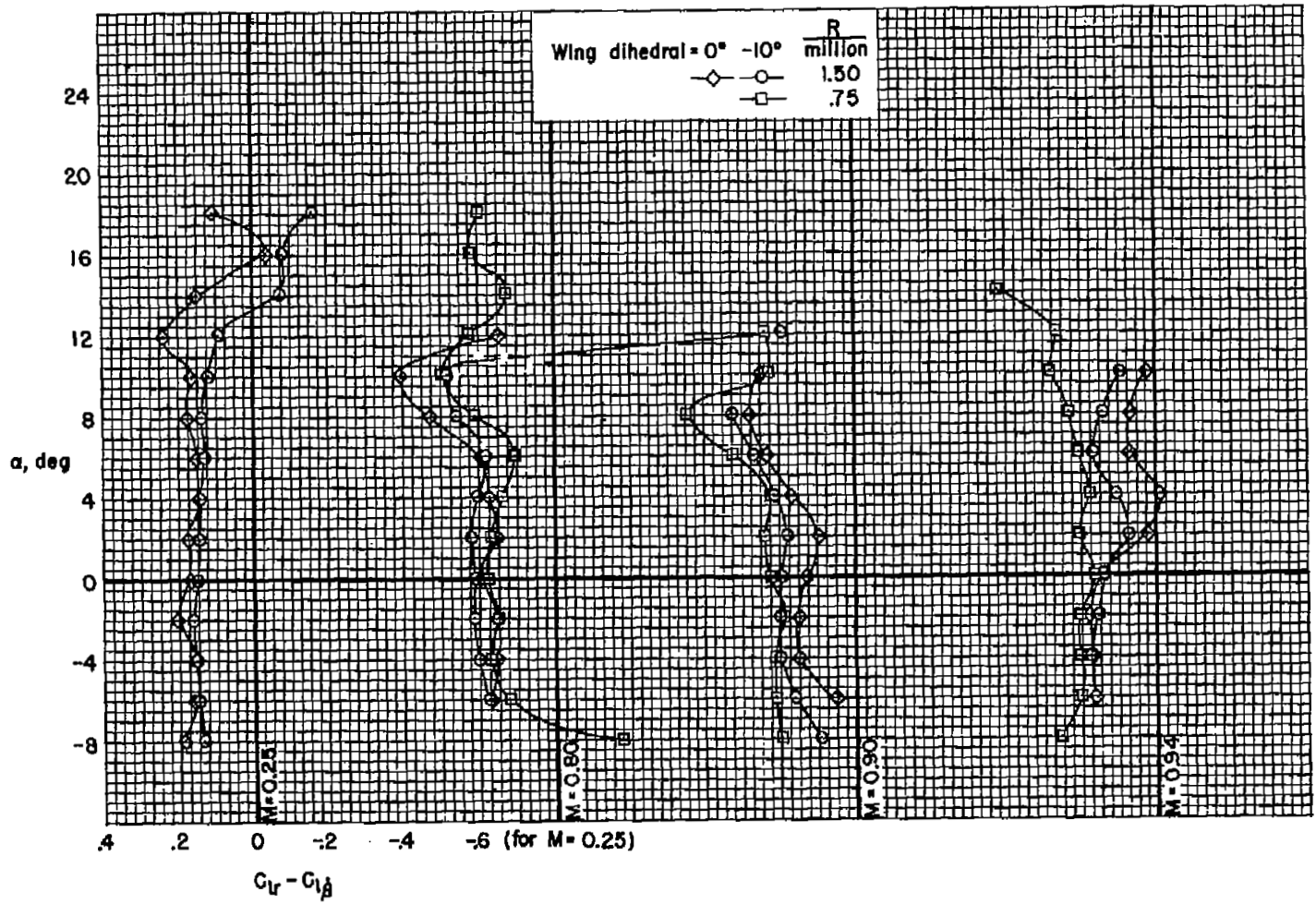


Figure 20.- The effect of Reynolds number and wing dihedral on the rotary derivatives of the complete model.



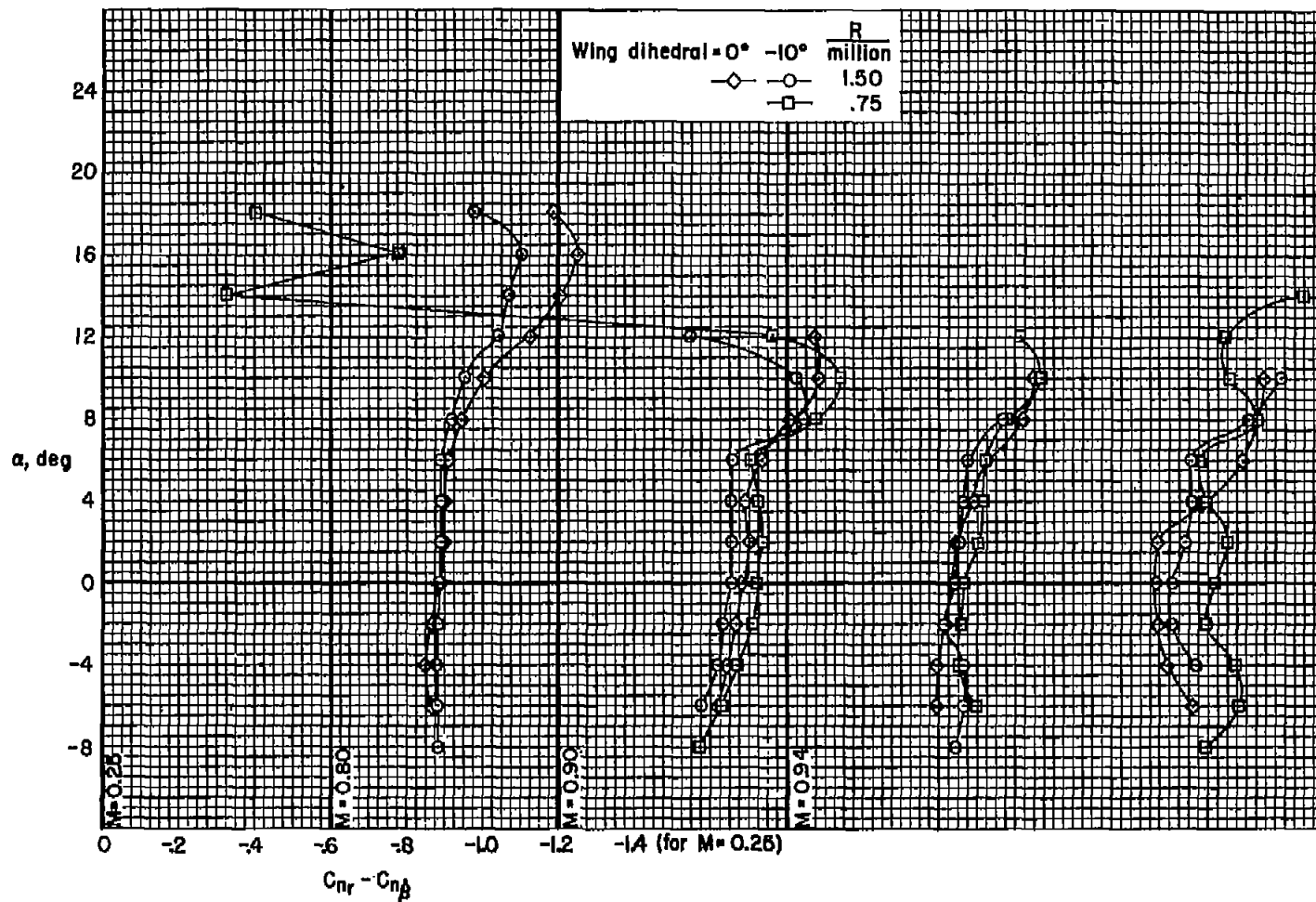
(b) C_{np}

Figure 20.- Continued.



(c) $C_{l_T} - C_{l_\beta}$

Figure 20.- Continued.



(d) $C_{nr} - C_{n\beta}$

Figure 20.- Concluded.

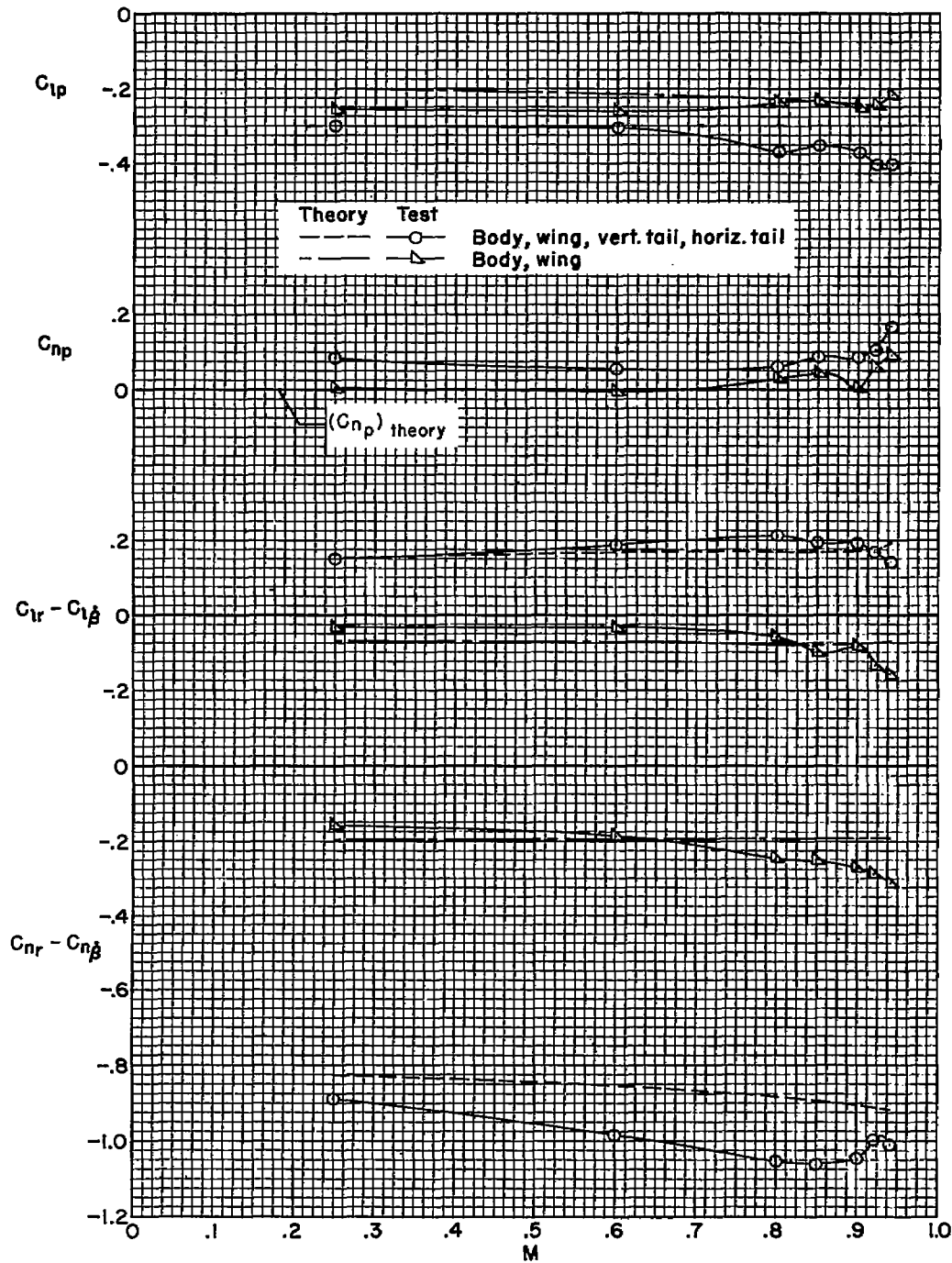


Figure 21.- The variation with Mach number of the rotary derivatives;
 $R = 1.50$ million, wing dihedral = -10° , $\alpha = 0^\circ$.

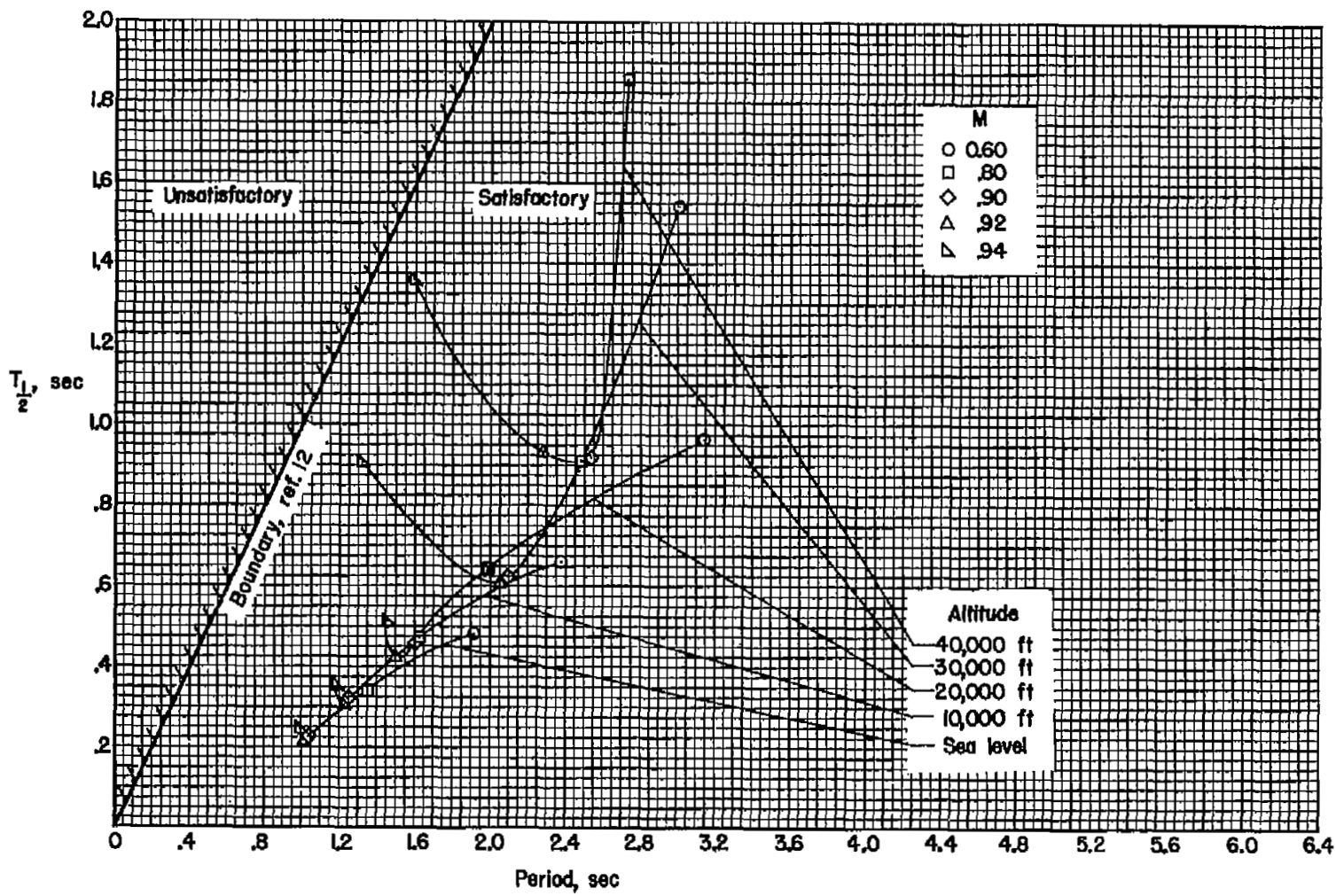


Figure 22.- Estimated period and time to damp of the controls-fixed, short-period, longitudinal oscillation for a representative airplane in level flight.

CONFIDENTIAL

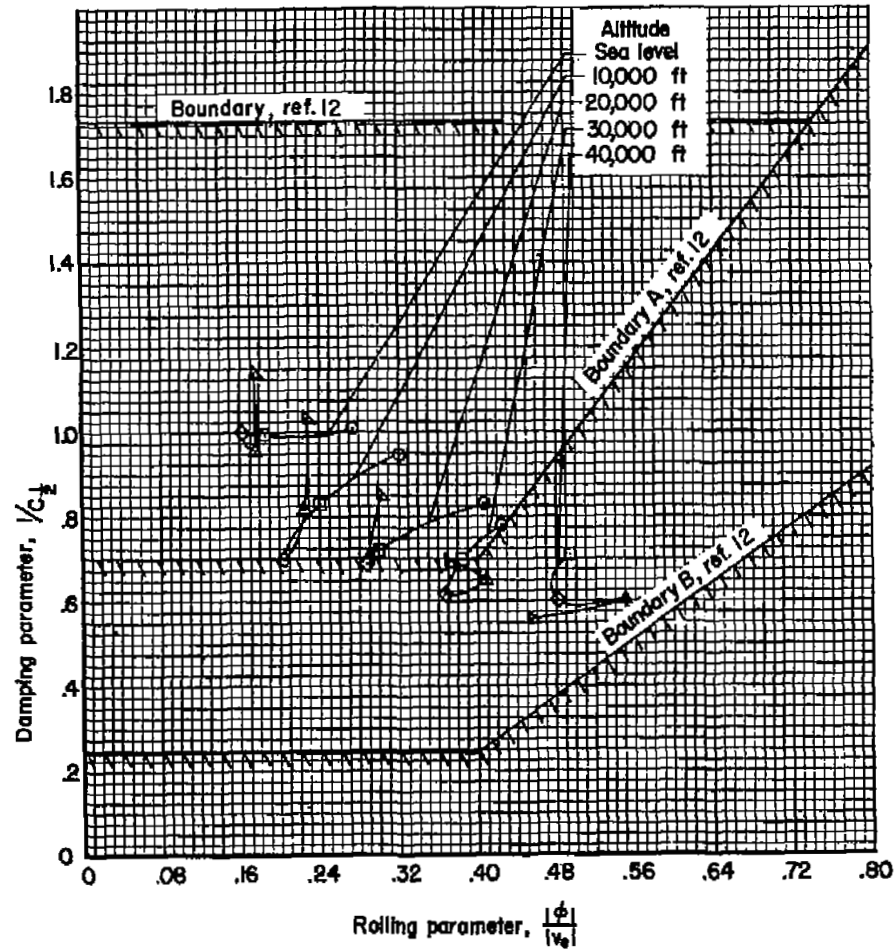
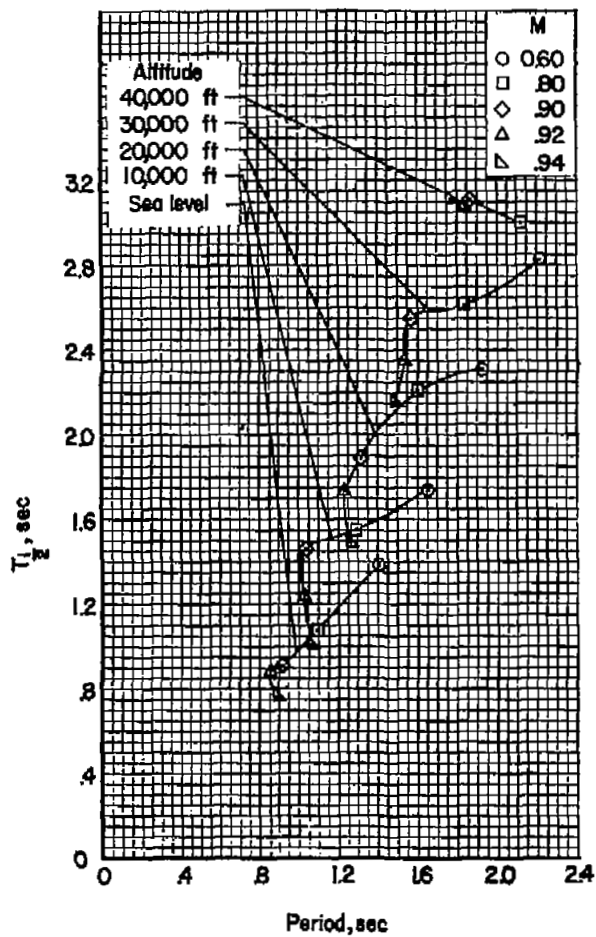


Figure 23.- Estimated characteristics of the controls-fixed lateral-directional oscillation for a representative airplane in level flight.

CONFIDENTIAL

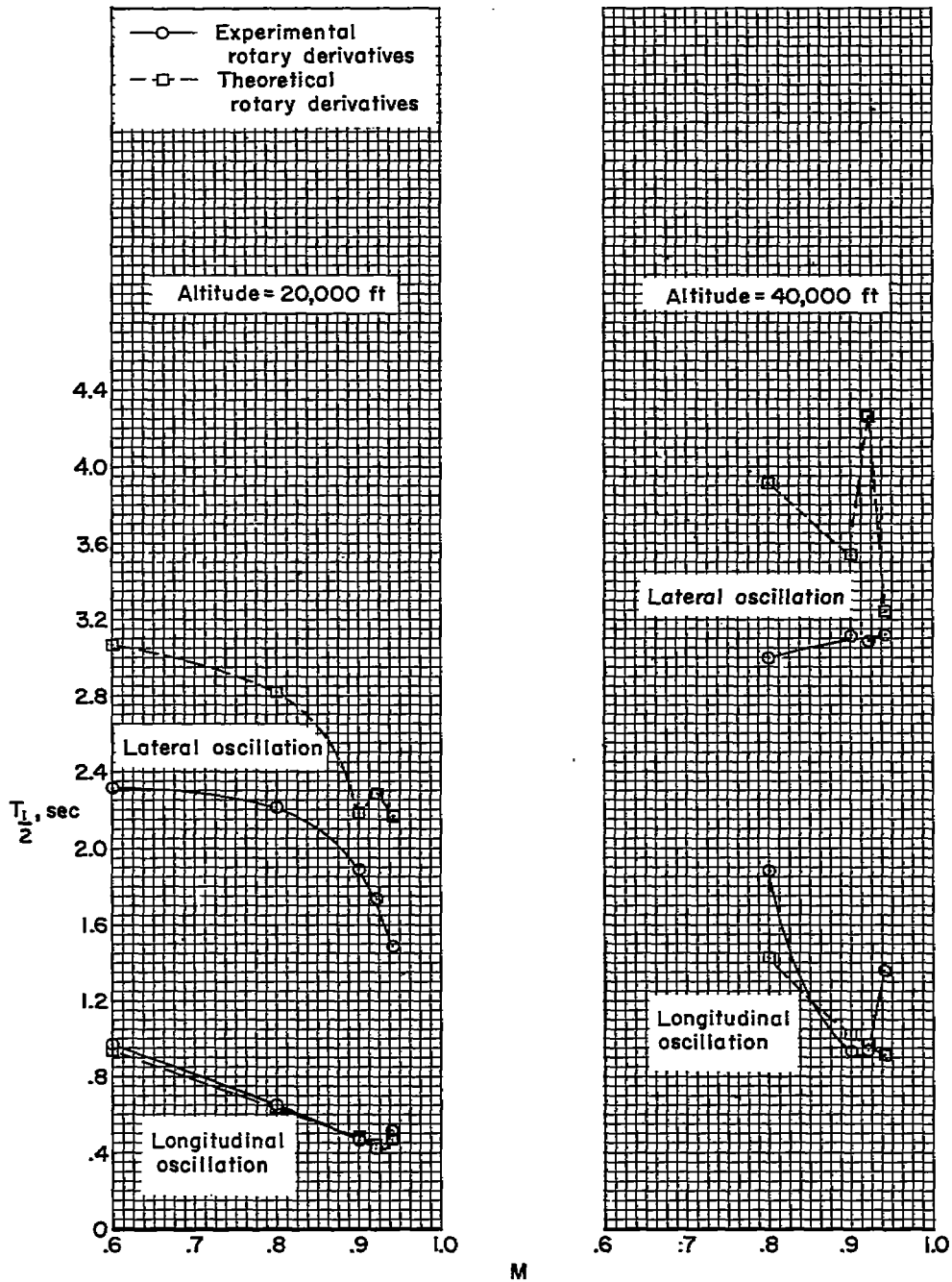


Figure 24.- The variation with Mach number of the calculated time to damp of the controls-fixed short-period oscillations for a representative airplane in level flight.

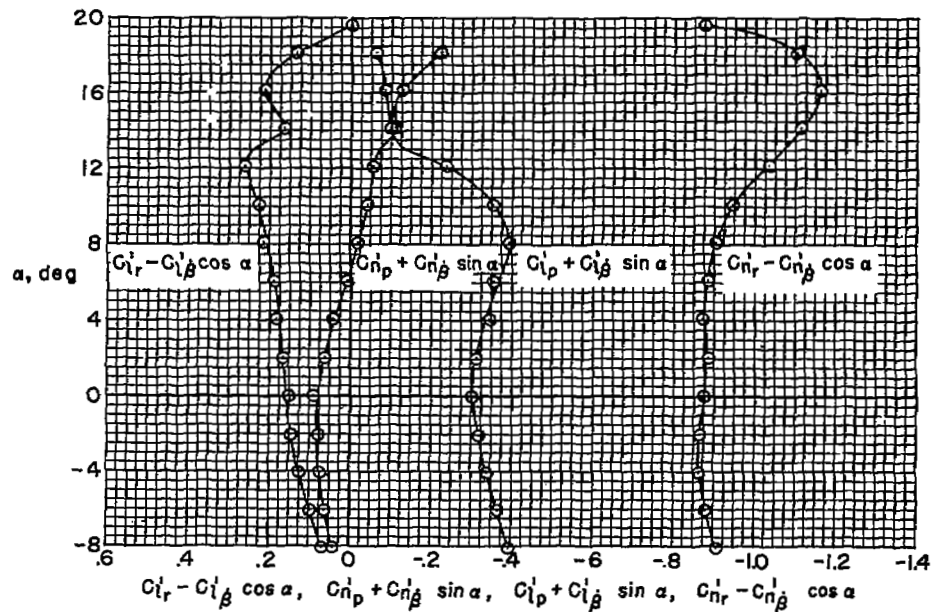
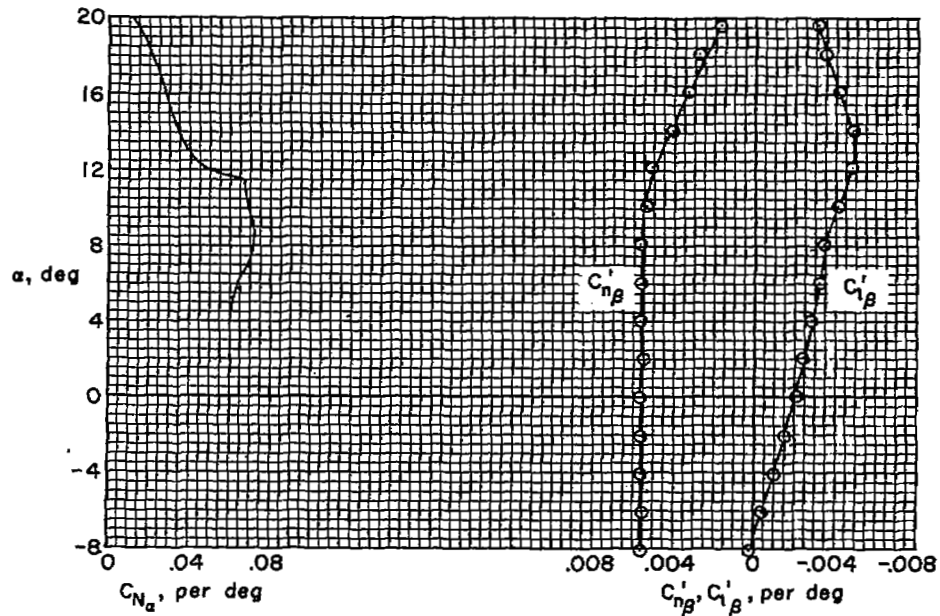
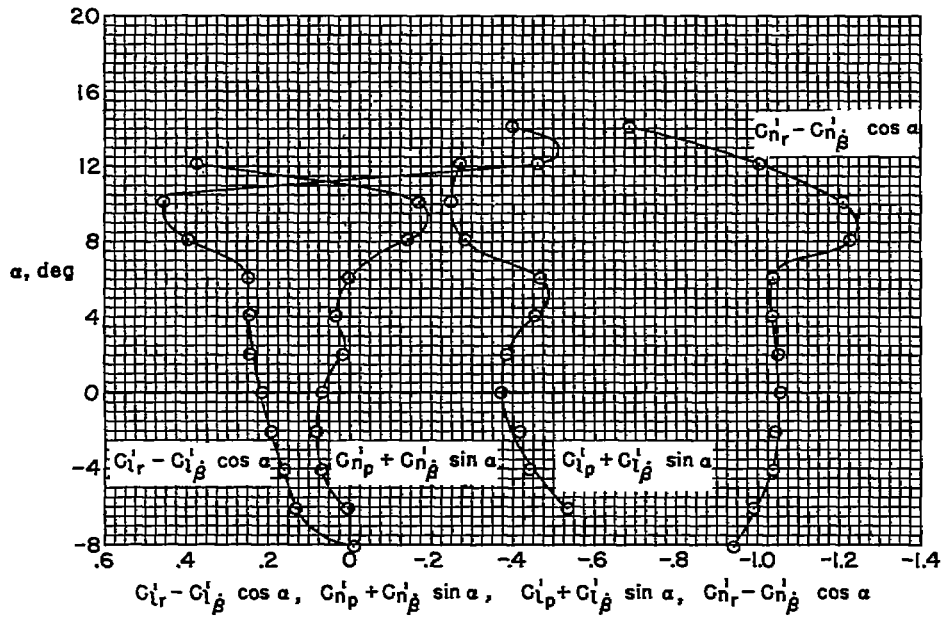
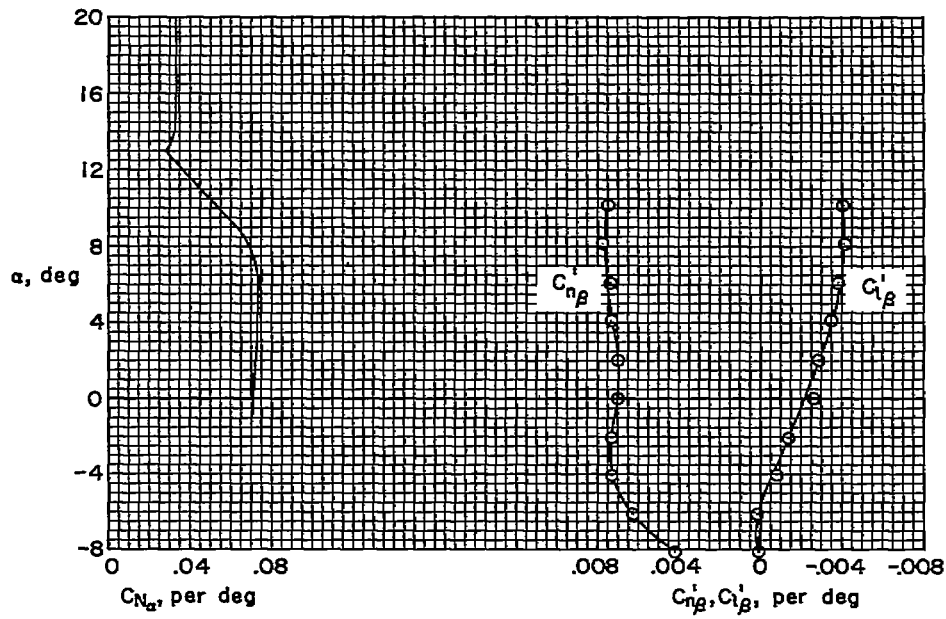
(a) $M = 0.25$

Figure 25.- The variations with angle of attack of C_{N_α} , and of the lateral-directional stability derivatives referred to body axes; $R = 1.50$ million, wing dihedral = -10° .



(b) $M = 0.80$

Figure 25.- Continued.

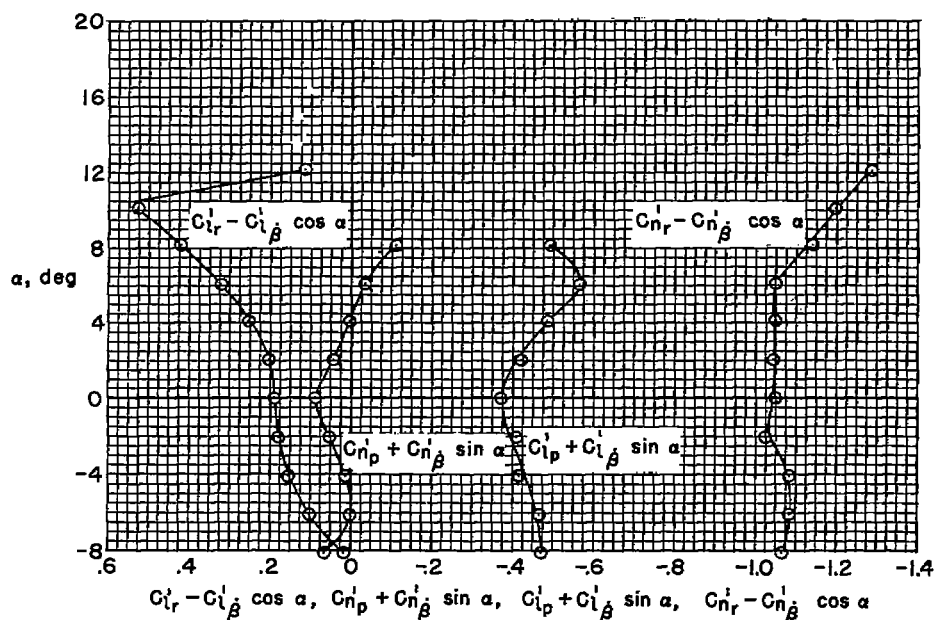
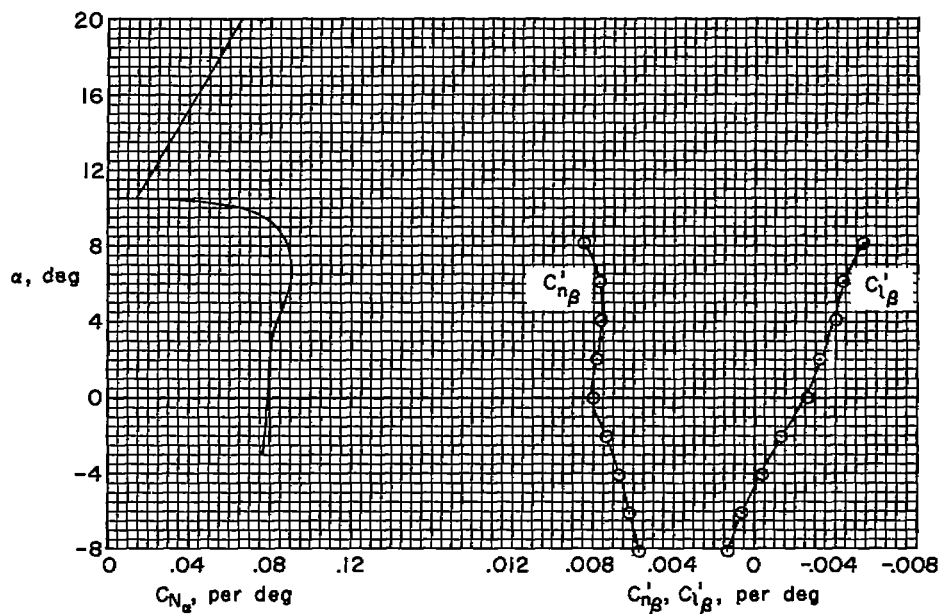
(c) $M = 0.90$

Figure 25.- Continued.

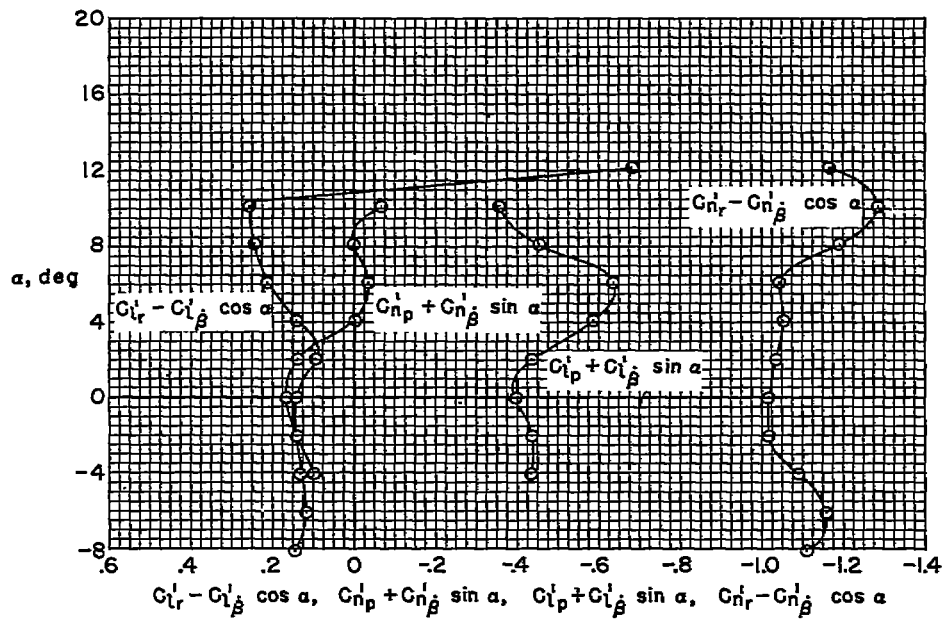
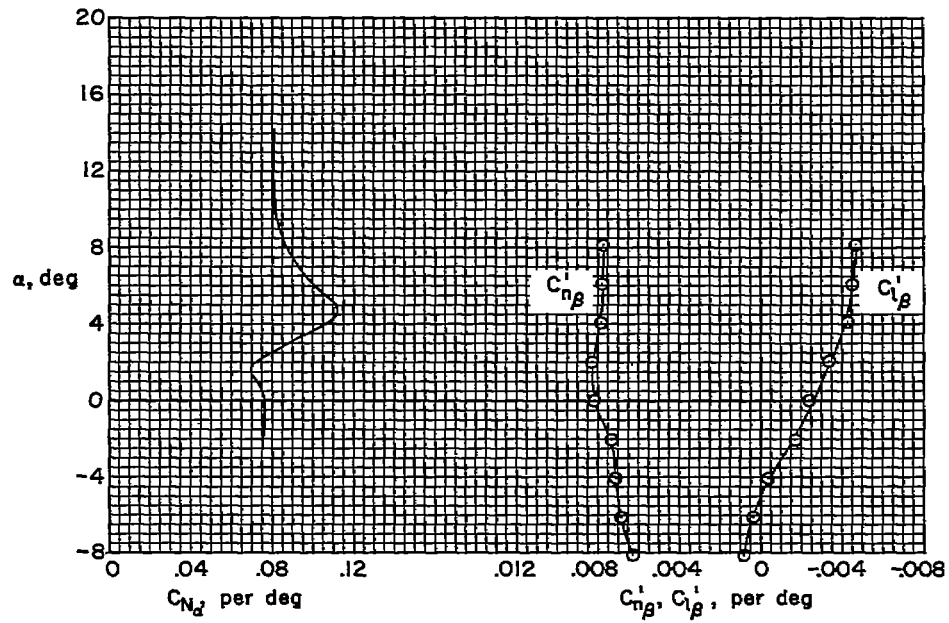
(d) $M = 0.94$

Figure 25.- Concluded.

CONFIDENTIAL